Engineering a Quantum Future: Exploiting Properties of Nanodiamond Materials

By

M. van Breugel

A thesis submitted to Macquarie University
for the degree of Doctor of Philosophy

Department of Physics & Astronomy
ARC Centre of Excellence for Engineered Quantum Systems
Quantum Materials & Applications Group
Diamond Nanoscience Laboratory

December 2020

MACQUARIE
University
SYDNEY·AUSTRALIA

Except where acknowledged in the customary manner, the material presented in this thesis is, to the best of my knowledge, original and has not been submitted in whole or part for a degree in any university.

M. van Breugel

Acknowledgements

Over the course of this degree I have been fortunate to work with many people. Thomas Volz, thank you for accepting me into the team and giving me direction across the many projects we have worked on. Carlo Bradac, I thank you for being my mentor. Your guidance and friendship have steered me well over the past decade and I am a better person for it. Lachlan Rogers, the knowledge and passion that drives you is remarkable. The imprint this has made on me will last well into the future. Mattias Johnsson, your office door has always been open to me and you have endured countless questions. Your kindness has not gone unappreciated. James Rabeau, thank you for your wise words over the years.

To my friends who have shared part of this journey with me I could not have come this far alone. To name each of you here would be a chapter of itself, but there are some who should be highlighted. Christina Baldwin, Reece Roberts, Glen Douglass, Shane Vickers, Tom Guff, Andrew Wood, Rochelle Martin, Sarath Raman Nair, Jemy Geordy, Matt Joliffe, Oliver Conquest, Cyril Laplane, James Wood, Mathieu Juan, Xavier Vidal, Gabriel Molina-Terriza, James Downes, Guillermo Munoz-Matutano, Ben Norton, Mike Steel, and Lisa Pesavento. Sarah Lau, your loving support has impacted me greatly, and I look forward to sharing many more experiences together.

A warm thank you to my family. To my mother, for supporting me with unwavering love. My father, for your advice and encouragement. My grandmother, for always welcoming me with open arms. And to my brother, the person I can always turn to with unquestioned trust.

There are many others who I have laughed with, travelled with, and stood side-by-side with — thank you for keeping me grounded in the world.

List of Publications

C. Bradac, M. Johnsson, M. van Breugel, B. Baragiola, R. Martin, M. L. Juan, G. Brennen, T. Volz, *Observation of room-temperature spontaneous superradiance from single diamond nanocrystals*, Nature Communications, 2017.

M. van Breugel, L. J. Rogers, O. Conquest, T. Feger, C. Schwab, D. Coutts, T. Volz, *Micro-Raman spectroscopy of diamond nanoparticles using an échelle spectrometer*, in preparation.

L. J. Rogers, M. van Breugel, T. Volz, *Multi-phonon decay from Raman scattering in Group-IV semiconductors*, in preparation.

Conference Proceedings

M. van Breugel, C. Bradac, M. Johnsson, B. Barigola, R. Martin, S. Kaiser, G. Brennen, T. Volz, *Room-Temperature Spontaneous Superradiance from Single Diamond Nanocrystals*, Hasselt Diamond Workshop, 2017.

M. van Breugel, C. Bradac, M. L. Juan, G. Molina-Terriza, T. Volz, *Silicon-vacancy Centres in Nanodiamond for Near-resonant Optical Trapping*, IONS KOALA, 2015.

Posters

M. van Breugel, O. Conquest, R. Roberts, L. Rogers, T. Volz, *Nano-scale Thermometry with Diamond*, Australian Institute of Physics (AIP) Congress, 2018.

M. van Breugel, C. Bradac, M. Johnsson, B. Besga, B. Barigola, R. Martin, M. Juan, G. Molina-Terriza, G. Brennen, T. Volz, *Room-Temperature Spontaneous Superradiance from Single Diamond Nanocrystals*, Okinawa Institute of Science & Technology (OIST) Coherent Quantum Dynamicd (CQD) Workshop, 2016.

M. van Breugel, J.-M. Le Floch, C. Bradac, S. Raman Nair, N. Carvalho, N. Nand, M. Tobar, T. Volz, *Towards Coherent Manipulation of Single Nitrogen-Vacancy Spins with a Macroscopic Microwave Cavity*, Australian Institute of Physics (AIP) Congress, 2016.

Abstract

Nanodiamond is a unique material that combines the extreme properties of diamond with the alluring properties of nanomaterials. Moreover, diamond can host colour centres — optically active defects that act like artificial atoms — some of which are renowned for their spin-optical properties. This makes nanodiamond material a prime candidate for implementing a range of future solid state quantum technologies. The practical implementation of diamond nanotechnologies in general relies on our capability to understand both diamond as a material and the properties of its colour centres. One particular defect, the nitrogen-vacancy (NV) colour centre, can be credited for launching diamond as a platform for quantum information processing, ultra-high resolution sensing, and biomedical applications. This thesis explores a set of different aspects of nanodiamond material containing NV centres, from spin to optical to vibrations degrees of freedom, with a particular eye to potential applications.

Firstly, a macroscopic dielectric loaded resonator microwave cavity was investigated as a new technology for driving the NV spin. The cavity is suspended ~ 1 cm above the surface of a sample, delivering a highly uniform driving field and negating sample heating effects. Implementing a Hahn spin-echo pulse sequence to measure the spin dephasing rates was ultimately unsuccessful due to the microwave cavity being unable to produce properly formed pulse shapes at short time scales.

Secondly, optical properties of densely-packed NV centres in nanodiamonds are investigated and the observation of room-temperature superradiance from single diamond nanocrystals is presented. These results represent the scientific apogee of this thesis. It is shown that nanodiamonds packed with a sufficiently high density of NV centres can exhibit cooperative effects, which are interrogated through the observation of superradiance. NV lifetimes as short as 1.1 ns are observed, which is a significant ($10\times$) speed-up in the photon emission rate compared to isolated NV centres. This is consistent with a model of cooperative effects, which is further confirmed by observing super-Poissonian photon statistics as predicted by our model.

The superradiance investigation uncovers the need to accurately measure the temperature of individual nanodiamond crystals. Raman spectroscopy methods for thermometry are developed, enabled by a novel ultra-high resolution échelle spectrograph. The analysis reveals that NDs on glass in air can be heated up to ~ 900 K with ~ 160 mW of focussed off-resonant laser illumination. This remarkable optical heating is concluded to occur for nanodiamonds in poor thermal contact with the substrate. Discrepancies are found when fitting the established 4-phonon decay model with the experimental data, however, individual nanodiamond data could be matched to a reference measurement in bulk diamond by altering the optical density of states. This is attributed to Mie resonances on the nanoparticles.

Finally, substantial efforts in development, modernisation, and automation of lab systems are reported. This work demonstrates how these efforts have already enabled semi-autonomous measurements to be conducted and have catalysed a change in our method of lab operation.

Contents

1

Introduction and Background

"If I have seen further it is by standing on the shoulders of giants."

Isaac Newton

Nanodiamond (diamond material with size of the order $\sim 100\,\text{nm}$ or smaller) is a unique material that combines the extreme properties of diamond with the alluring properties of nanomaterials. The material has attracted increasing attention over the last few decades due to its vast potential for applications in nanotechnology. Key to this attraction is not only the extreme material properties of diamond, but diamond's ability to host a large variety of colour centres — defects that give diamond colour. Over 500 colour centres are known to exist in diamond [1]. Those that absorb light create the colour perceived by the human eye, and some colour centres can also re-emit absorbed light. Many colour centres posses unique optical and spin properties, including the well-known nitrogen-vacancy (NV) centre (§ 1.3.2). The applications of nanodiamond-based technologies are far-ranging, from single-photon generation and solid-state spin qubit registers for quantum information, to ultra high-resolution sensing, and as non-toxic biomarkers for the life sciences.

The practical implementation of these applications relies on our capability to understand both diamond material and the properties of its colour centres. For quantum technologies the diamond must be of ultra-high purity as not to shorten spin coherence times. For sensing and biomedical applications the nanoscale size of the material and the optical stability of colour centres is crucial. Complex surface physics means that these demands are often in conflict, and a lot of research effort has been put into developing diamond-based nanotechnologies. This has driven a fast pace for the diamond nanoscience field, including improvements in diamond material science [2] and in colour centre creation [3]. Indeed, the growth of research publications in this field has been rapid, as illustrated in Figure 1.1.

1.1 Motivation and Scope

Quantum-enhanced and quantum-enabled sensing and metrology have emerged recently as particularly active fields of research. Many of the initial demonstrations in this field have
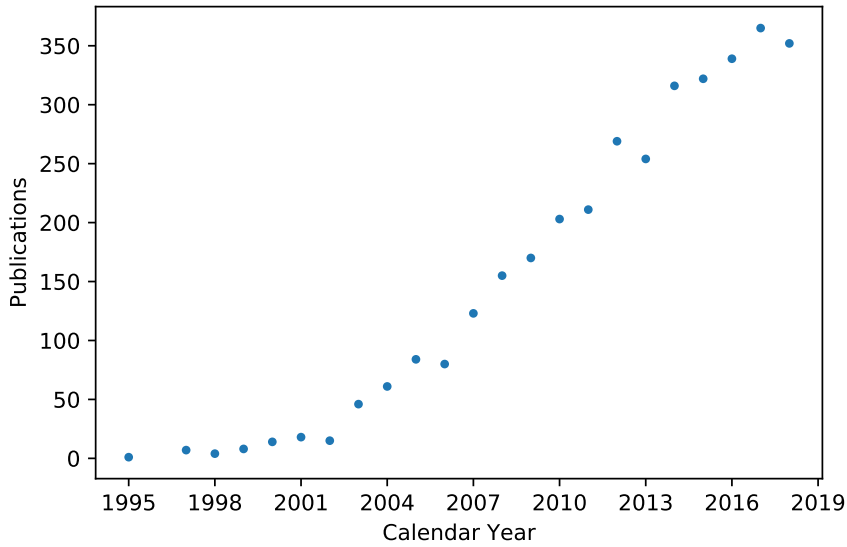
Figure 1.1: Publications referencing nanodiamond. Publications containing nanodiamond in their search metadata from 1995 – 2018. Source: Google Scholar.

been applied to fundamental problems in biology, such as nanoparticle tracking, measurements in trapped nanoparticles, MRI enhancement, and drug delivery [4–11]. However, the significance of nanodiamond-based sensing and metrology applications spans further than the life sciences, reaching fields such as magnetic field sensing, semiconductor electronics, microelectronics, temperature sensing, pressure sensing, and other future applications [12–18]. We note that the use of nanodiamond materials for sensing and metrology is still a young area of study, seeded by the first realised magnetometry applications in 2008 [12, 13].

This PhD project has been performed as part of a team and lab with a traditional focus on the applications of nanodiamond and other quantum materials. The thesis reports a variety of physics investigations that have stemmed from questions arising in the context of sensing and metrology applications, with the ultimate goal of using this knowledge for engineering quantum systems. In particular, this work focuses on aspects of diamond nanoscience that exhibit quantum properties — with emphasis on the underlying physics as opposed to specific sensing protocols. This chapter presents an overview of diamond as a material and the optically active atomic-scale defects it hosts. These defects are known as colour centres, some of which possess favourable spin and optical properties. In particular we discuss the nitrogen-vacancy (NV) centre, proven as a unique tool for many applications that have expanded the horizons for diamond nanoscience over the past half century. These topics and concepts are an important basis for understanding the work in subsequent chapters.

The all-optical initialisation and readout of the NV spin is well-established [19, 20]. The NV centre has the longest room-temperature spin-coherence time of any optically active solid state system [2][1], and on-going work to couple NV spin systems [21–24] all contribute to the NV centre in diamond generating disruptive quantum technologies. In **Chapter 2** we present our efforts to use a dielectric loaded resonator cavity to conduct spin measurements on the NV centre. In parallel with the cavity we use a stripline antenna with an identical

---

[1]Phosphorus donors in silicon are not optically active, however, are capable of achieving coherence times of up to 60ms [25] and have well demonstrated capabilities for quantum technologies.

sample such that we can draw comparisons between these microwave delivery methods. We generate Rabi oscillations in single NV spins, however, find that the cavity design prevents us from successfully conducting decoherence measurements via the Hahn spin-echo sequence.

Superradiance in room-temperature, solid-state systems may lead to technological innovations and applications in efficient photon detection, energy harvesting and quantum sensing. Of direct relevance to the research efforts of our team was to explore the underlying physics of superradiance in nanodiamonds containing many NV centres to further understand previous results from conducting optical trapping experiments [26]. Therefore, in **Chapter 3** we investigate properties of diamond nanoparticles containing a high density of NV centres. Specifically, we report the observation of room-temperature superradiance for single nanodiamonds. A significant speed-up in the photon emission rate is observed, in addition to non-trivial correlations between the emitted photons.

In addition to these important scientific findings, part of my PhD project was devoted to the significant development, modernisation, and automation of experimental lab systems. Our experiments into the investigation of superradiance phenomena required the gathering of a large data set comprised of measurements repeated across many individual NDs. Its construction was labour intensive, with no methods for conducting autonomous or semi-autonomous measurements. This became the major driving force in developing a system whereby automated measurement processes could be conducted, in addition to the need to replace our workhorse piezoelectric scanning stage in our confocal microscopy apparatus, which itself required extensive efforts. Furthermore, to enable wide-range, single-shot spectroscopic measurements we collaborated with a team of astronomers within the Physics Department. We made use of a novel échelle spectrograph which they had built, requiring the development of data extraction methods. This work enabled wide-range spectroscopy exceeding the resolution of instruments currently on the market. These developments are detailed in **Chapter 4**.

In the highly-dynamic environment of a research lab, new ideas emerge and manifest into previously unforeseen experimental projects. **Chapter 5** follows from questions raised in the superradiance study concerning the local temperature of the analysed nanodiamonds. We present a Raman spectroscopy method to scrutinise temperatures of individual nanodiamonds. As part of this endeavour we produce evidence of laser-induced heating of individual nanodiamonds that are in poor thermal contact with the substrate. Additionally, this chapter illustrates the effectiveness of the automation and procedural upgrades that are described in Chapter 4.

Finally, **Chapter 6** contains conclusions and future prospects generated by this research. Strong potentials exist for much of the key research presented in this thesis, in particular for the continued investigation of superradiant behaviour in single-crystal nanodiamonds, and for the application of nanodiamond material for highly spatially localised temperature measurements.

1.2   Diamond and Colour Centres

In addition to the macroscopic qualities of diamond that have contributed to its impressive brand, it is diamonds mesoscopic properties that makes it appealing for the development of nanotechnologies. Defects in the diamond lattice, either irregularities and/or the inclusion of foreign atoms, can give rise to unique physical characteristics. For instance, diamond can be host to defects that are optically active, so called colour centres, some of which are

renowned for their spin-optical properties. Here we review in particular the nitrogen-vacancy (NV) colour centre which has arguably launched diamond as a promising candidate for many solid-state quantum technologies. In fact, over the last few years diamond colour centres have become the foundation, or even the archetype systems, for several quantum information technologies and ultra-high resolution sensing applications, as well as bio-imaging and bio-marking schemes for diagnostics and therapeutics. It is our control over the fabrication and characteristics of diamond, in combination with our understanding of the underlying physics of colour centres, that have made it the material of choice for leading-edge technologies.

1.2.1   Lattice Structure

The crystalline structure of diamond originates from carbon atoms arranged in a characteristic tetrahedral lattice [27]. Each carbon atom bonds covalently to its four neighbours via sp^3 hybrid orbitals. The resulting crystal lattice is strong and resistant to deformation, and is a key contributor to diamonds extreme properties.

1.2.2   Physical Properties

Diamond exhibits extreme physical properties compared to other materials. The following is a small review of a subset of these properties. In the case of diamond's mechanical properties we draw comparisons between diamond, silicon, and germanium, as all three share the same lattice structure.

Hardness   As a result of diamond's rigid tetrahedral crystal structure and the strong covalent bonds of the carbon atoms, diamond is the hardest known natural material. On the Mohs scale, which is a measure of scratch hardness, diamond ranks a value of 10 at the top of the scale [28]. The Mohs scale is non-linear; diamond is four times harder than compounds with a rank of 9 on the scale. Silicon ranks 6 and germanium 7 on this scale, approximately ten times lower than diamond.

Strength   The stress required to deform a material determines its strength. For diamond containing no defects, this value can be greater than 90 GPa for tensile, compression, and shear stresses [29–35]. For silicon and germanium, their ideal strength is merely 25 GPa.

Elastic Properties   This section can be subdivided into four constituents; Young's modulus, shear modulus, Poisson's ratio, and bulk modulus. Young's modulus is related to the tensile strength of a material, and is the ratio between the uniaxial stress and the uniaxial strain in the linear-elastic regime. For diamond the value of this ratio is approximately 1100 GPa, in contrast to 160 GPa for silicon and 130 GPa for germanium [33] — which are both an order of magnitude smaller. The shear modulus is related to the deformation of a solid as it experiences forces parallel to its sides, in opposite directions on opposing sides. It is the ratio of shear stress and shear strain, and for diamond its value is 550 GPa compared to 60 GPa for silicon and 50 GPa for germanium [33] — again around 10 times smaller. The Poisson's ratio of a material is also related to its deformation, though is the ratio between transverse strain and axial strain, or between stretching in one direction and compression in perpendicular directions. The value for diamond is 0.07, meaning that it has a high resistance to deformation. For silicon and germanium the value is 0.2 — about 3 time larger. Finally,

Table 1.1: Values of refractive index of diamond for different wavelengths [38].

Wavelength (nm)	Refractive Index
226.5	2.715
480.0	2.437
535.8	2.424
578.0	2.419
656.0	2.410
2500	2.379
25 000	2.375

the bulk modulus is a measure of a material's resistance to uniform compression. The bulk modulus value for diamond is 440 GPa, whereas in silicon is 100 GPa and in germanium is 80 GPa [33] — a quarter of the value.

Thermal Conductivity   Diamond has an extremely high thermal conductivity, making it an exceptional material for applications in high-frequency, high-power, high-temperature, and high-voltage applications. Monocrystalline diamond has a thermal conductivity of 2200 W/ (m · K) at room temperature [36], which is extreme when compared to that of copper at 400 W/ (m · K).

Specific Heat   The specific heat is a measure of the amount of heat per unit mass required to raise the temperature of a material by one degree Celsius at 300 K and with constant pressure and volume. For diamond this has been measured to be 6.195 J/ (mol · K).

1.2.3   Optical Properties

The optical properties of diamond vary depending on the presence of defects within the lattice. Here we consider diamond containing few to no lattice defects.

Refractive Index and Dispersion   Diamond has a high refractive index compared to most other transparent materials. A selection of reference values are shown in Table 1.1. In the optical region, the refractive index of diamond varies with wavelength much more than most (but not all) other materials. The difference in refractive index of a material between the blue / violet region and the red region is known as the coefficient of dispersion. For diamond this value is 0.044, greater than that of some crystals e.g. quartz (0.013) but less than that of other crystals e.g. cassiterite (0.071) [37].

Optical Transparency and Effects of Colour Centres   For wavelengths of 225 nm $< \lambda <$ 2000 nm and $\lambda > 6000$ nm the measured transmissivity of diamond is 0.7. In the range 2000 nm $< \lambda <$ 6000 nm the transmissivity falls below 0.7 as a result of infrared absorption of carbon-carbon systems [39]. In the optical regime diamond can often appear coloured [37]. This colouration is attributed to defects in the diamond lattice, stemming typically from the inclusion of foreign atoms [1]. If the defects fluoresce they are said to be optically active, and can possess interesting spin and optical properties once isolated.

1.3   Defects in Diamond

All defects can be classified as intrinsic, extrinsic, or as a combination, regardless of their optical activity. Over the optical range from 170 nm to 20 μm diamond has more than 500 optically active defects [1], including the well known nitrogen-vacancy (NV) centre (§1.3.2).

1.3.1   Intrinsic and Extrinsic Defects

Irregularities within the diamond lattice are referred to as intrinsic defects. Such defects can occur naturally or can be induced by methods such as irradiation [40]. There exist multiple specific types of intrinsic defects, including sites shared by an extra carbon atom [41, 42], sites missing a carbon atom (vacancies) [43, 44], and lattice sites with broken bonds [45].

Conversely, the incorporation of foreign atoms into the diamond lattice form extrinsic defects. Again, these can be either naturally occurring or induced by artificial means such as ion implantation, see § 1.4.2. Two types of extrinsic defects exist; substitutional and interstitial defects [27]. As its name suggests, a substitutional defect consists of a foreign atom substituting a carbon atom at a lattice site. In the case of an interstitial defect a foreign atom is lodged in the lattice between lattice sites. It is these extrinsic defects that give rise to the colour of diamond material [1, 46, 47].

1.3.2   The Nitrogen-Vacancy Centre

The nitrogen-vacancy (NV) centre has attracted considerable attention over the past two decades and is one of the most studied defects in diamond. The NV defect is the arrangement of a nitrogen atom and an adjacent empty lattice site substituting carbon atoms in the diamond lattice, orientated along the $\langle 111 \rangle$ direction [48, 49], illustrated in Figure 1.3.

Electronic and Optical Properties

The NV can be found in either its neutral charge state NV^0, or its negatively charged state NV^-. The NV^- exhibits the unique spin and optical properties that have generated considerable interest. Therefore, hereafter the abbreviation 'NV' will refer directly to the negatively charged state unless otherwise specified.

A single NV centre isolated in the diamond lattice behaves as an artificial atom — an emitter with a discrete anharmonic energy level structure. The unique properties of the diamond matrix allow this structure to retain its atom-like quantum behaviour at room-temperature. Its defined energy levels have optically active transitions, giving the NV centre its own unique spectral fingerprint, as shown by the photoluminescence spectrum in Figure 1.4a. Of significant interest in the NV spectrum is its zero-phonon line (ZPL), located at 637 nm, corresponding to the energy difference between the zero-vibrational state of the ground and excited levels [50]. The spectrum also features a large phononic sideband red-shifted from the ZPL. In-fact, merely 4% of the NV fluorescence falls into the ZPL [3]. However, even a single NV centre (either isolated in a nanodiamond or spatially distinct in bulk diamond) produces a strong photoluminescence signal detectable via standard confocal microscopy. This is the result of a large optical absorption cross-section in comparison to other Group-IV colour centres, a relatively short excited state lifetime, high quantum efficiency, and the absence of a long-lived dark state that shelves the fluorescence [51].
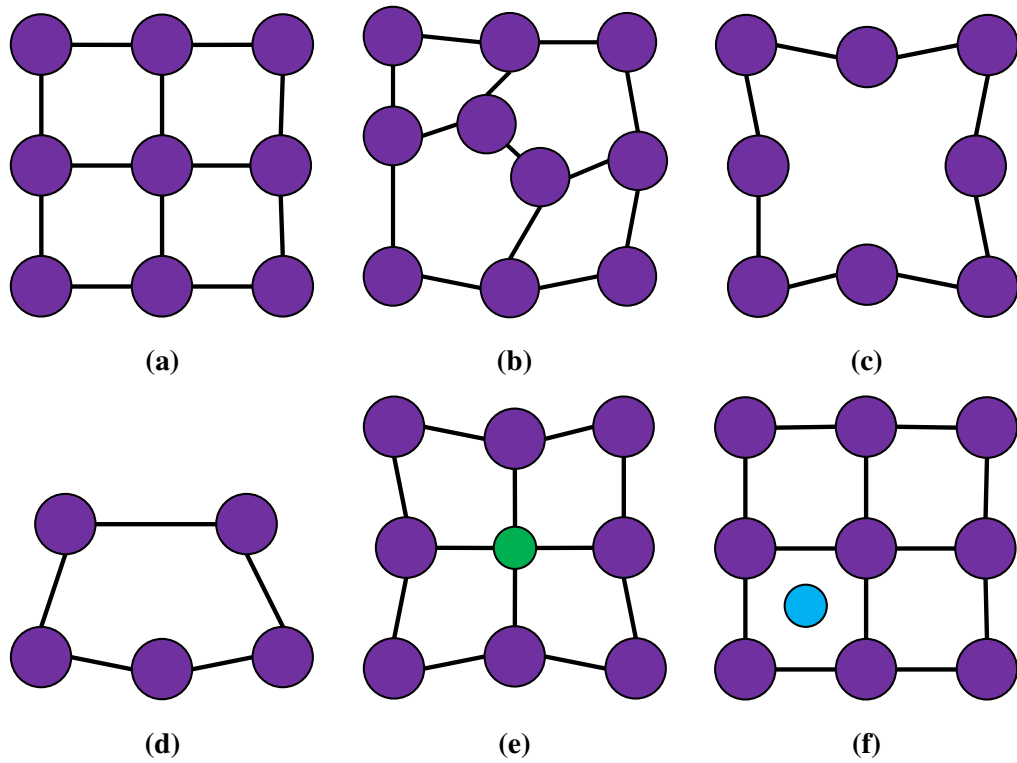
Figure 1.2: Lattice defects. A schematic representation of intrinsic and extrinsic defects in a lattice (not specifically diamond). Atoms belonging to the material are shown as purple, and foreign atoms are shows as both green and blue. **(a)** A lattice example with no irregularities. **(b)** An intrinsic defect where a lattice site is shared by an extra carbon atom. **(c)** A lattice site missing a carbon atom, said to be a vacancy, also an intrinsic defect. **(d)** A lattice site with broken bonds is also an intrinsic defect. **(e)** An extrinsic, substitutional defect from a foreign atom substituting a carbon atom at a lattice site. **(f)** An extrinsic, interstitial defect where a foreign atom is lodged in the lattice between lattice sites.

The energy level structure of the NV is at the core of both its spin and optical properties. Six electrons are associated with the NV centre: three "dangling bonds" from the carbon atoms surrounding the vacancy, two "dangling bonds" from the nitrogen atom (the nitrogen atom uses three of its five valence electrons to bond to its neighbouring carbon atoms), and one provided from elsewhere in the lattice (typically from a nearby substitutional nitrogen impurity) [53]. The majority of the charge density ($\sim 72\%$) is located about the three carbon atoms surrounding the vacancy, a small fraction located about the nitrogen atom ($\sim 0.2\%$), and the remainder spread over the surrounding lattice ($\sim 28\%$) [54].

The structure of the energy levels (Figure 1.4b) feature ground and excited triplet states separated by the aforementioned ZPL transition at 637 nm. The ground triplet has a zero-field magnetic resonance in the microwave regime at ~ 2.88 GHz [55, 56]. In the absence of a magnetic field the ground state $m_s = \pm 1$ sub-levels are degenerate, however, the presence of a magnetic field lifts this degeneracy due to the Zeeman effect. The $m_s = \pm 1$ sub-levels then become resonant slightly above and below the zero-field ~ 2.88 GHz value. The high-sensitivity of this splitting, as well as the ability to detect it optically (§ 1.3.2), make the NV an excellent tool for magnetic sensing [12, 13, 57–59].
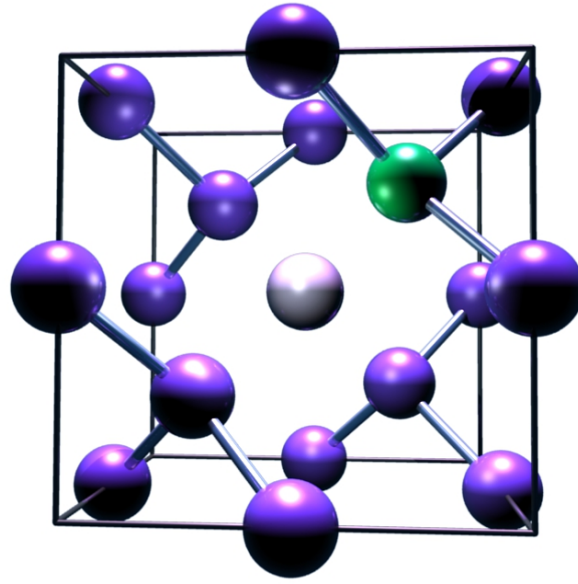
Figure 1.3: The nitrogen-vacancy centre in diamond. A representation of the diamond lattice containing an NV centre. A nitrogen atom (green) and a neighbouring vacancy (white) replace carbon atoms (purple) in the diamond lattice (two interpenetrating face-centred cubic (fcc) Bravais lattices [27]).

Spin Manipulation

The ground state of the NV centre can be approximated as a two-level quantum system due to its spin-conserving optical transitions, which can be pumped to the first allowed energy level (excited state) by 532 nm laser excitation. The NV triplet ground energy levels with magnetic quantum numbers $m_S = 0$ and $m_S = \pm1$ are split by spin-spin interaction by ~ 2.88 GHz. The cyclic luminescence of the $m_S = \pm1$ excited state is 30% less efficient than that of the $m_S = 0$ excited state, which when the system is optically pumped results in population of the $m_S = 0$ ground state — thereby spin-polarising (or initialising) the NV centre, illustrated in Figure 1.5a. Microwave radiation at ~ 2.88 GHz is able to mix (manipulate) the two ground states ($m_S = 0$ and $m_S = \pm1$), Figure 1.5b, which therefore causes a decrease in the luminescence signal. This is due to the fact that the $m_S = \pm1$ state scatters less photons than the $m_S = 0$ state. It follows that interrogating the degree of fluorescence of the NV when the system is again excited (observing if the system is 'bright' or has 30% less counts) tells us which state ($m_S = 0$ or $m_S = \pm1$) the system was in (readout), illustrated in Figure 1.5c and Figure 1.5d respectively.

1.4   Diamond Growth & Colour Centre Creation

Diamond material naturally forms between the range of 150 km and 200 km below the surface of the Earth [61], where extreme temperatures and pressures provide the energy required for stable diamond crystallisation. The process of honing synthetic diamond growth commenced circa 1950. Since, the ongoing desire to refine and advance the process has driven a significant volume of research, initially with large gaps between new discoveries.

(a)

(b)
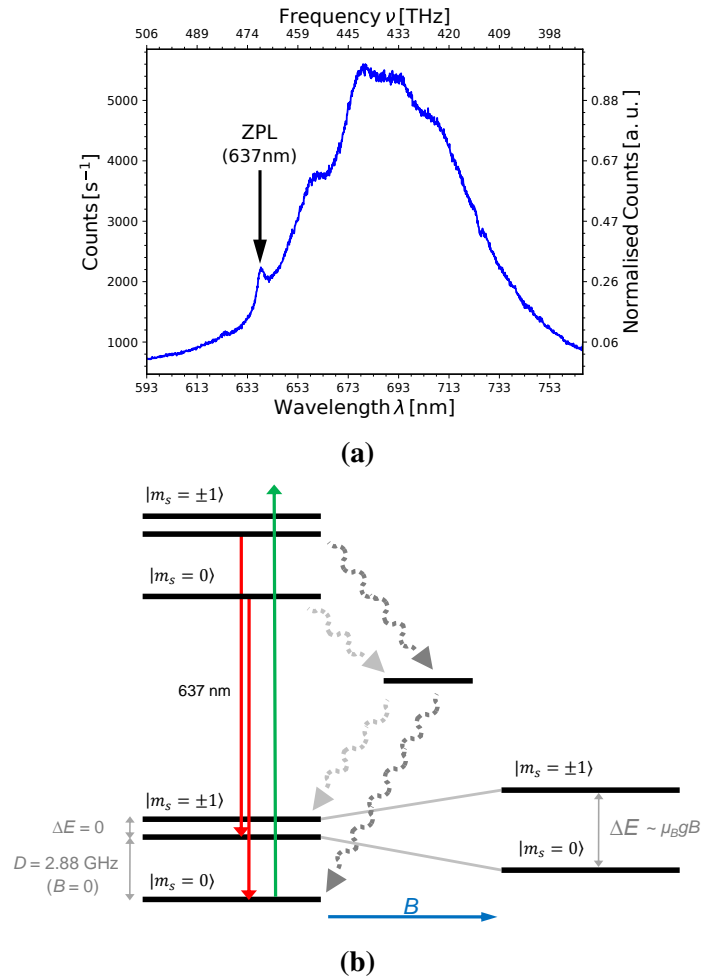
Figure 1.4: NV electronic structure and photoluminescence spectrum. (a) Spectrum of a single NV centre recorded at room-temperature under 532 nm laser excitation. The ZPL is annotated, and the large phononic sideband can be observed. (b) The electronic energy level structure of the NV centre in diamond. Radiative transitions are denoted with solid arrows, and non-radiative 'dark' decay channels with dashed arrows. The transition between the ground and excited state corresponds to 637 nm, and that between the ground triplet to ~ 2.88 GHz (with zero magnetic field). Note that weak relaxations occur from the excited $|m_s = 0\rangle$ state and the shelving state [52].

1.4.1 Growth Methods

High-Pressure High-Temperature

The first synthetic growth method employed to create diamond in a laboratory environment mimicked the conditions of high-pressure and high-temperature found beneath Earth's crust. This method, aptly named 'high-pressure high-temperature' (HPHT), was first achieved in 1953 [62], a few years after the phase diagram for carbon was initially mapped in 1938 [63] (later expanded in 1955 [64]). The method uses large anvils to exert pressure (above 5 GPa) on a heated (above 1500 °C) reaction cell [65, 66]. The cell is filled with high-purity carbon-containing materials such as graphite, in addition to a solvent metal — typically iron or nickel. The solvent metal transports the dissolved carbon to seed diamonds, while it also reduces the minimum external pressure required to reach the target growth conditions. The HPHT method continues to be used today due to its low cost and high throughput. It does
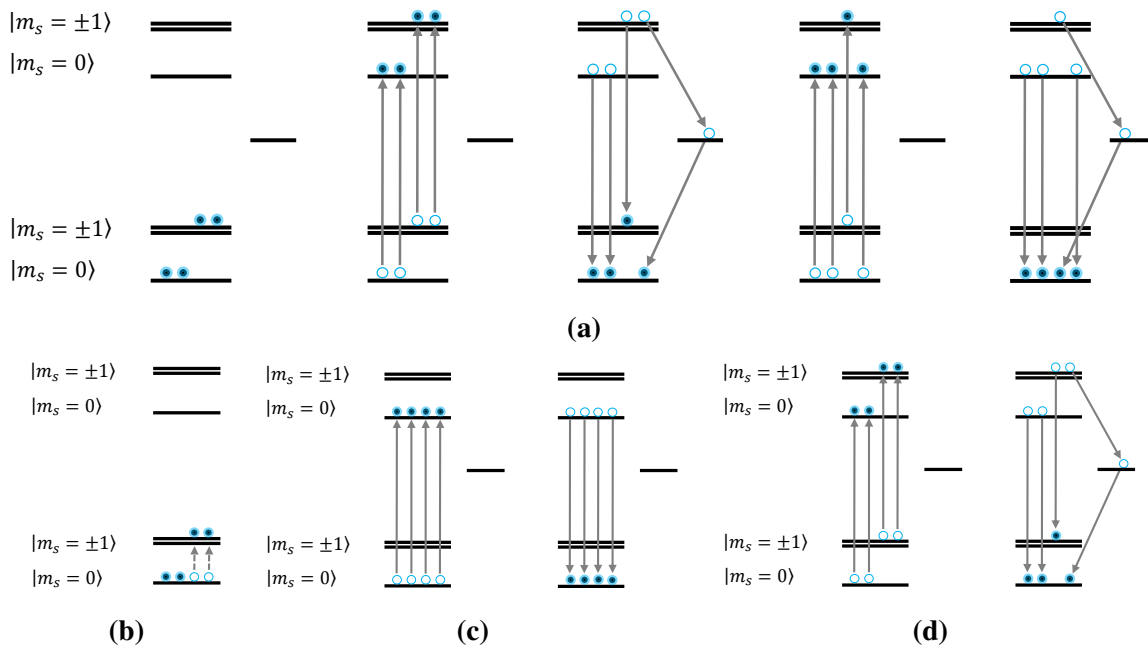
Figure 1.5: Illustration of the control mechanisms implemented to initialise, manipulate and readout the state of the NV. The ground state of the NV can be approximated as a two-level quantum system due to its spin-conserving optical transitions, which can be pumped to the first allowed energy level (excited state) by 532 nm laser excitation. The NV triplet ground energy levels with magnetic quantum numbers $m_S = 0$ and $m_S = \pm 1$ are split by spin-spin interaction by ~ 2.88 GHz. Of course, the NV defect has only a single electron to manipulate. In this figure the defect is depicted with four electrons only to provide a more intuitive representation for the reader, i.e. the schematic should be interpreted as the evolution over time of the photodynamics of a single NV centre. **(a)** The cyclic luminescence of the $m_S = \pm 1$ excited state is 30% less efficient than that of the $m_S = 0$ excited state, which when the system is optically pumped results in population of the $m_S = 0$ ground state — thereby spin-polarising (or initialising) the NV centre. **(b)** Microwave radiation at ~ 2.88 GHz is able to mix (manipulate) the two ground states ($m_S = 0$ and $m_S = \pm 1$). **(c)** Interrogating the degree of fluorescence of the NV when the system is again excited tells us which state ($m_S = 0$ or $m_S = \pm 1$) the system was in (readout). If the system was in the $m_S = 0$ state upon re-illumination then we observed photon count is 'bright', and **(d)** if the system was in the $m_S = \pm 1$ state then we observe a photon count rate 30% reduced. Figure adapted from [60].

not, however, allow for a wide range of customisation and control of the synthesis process.

Chemical Vapour Deposition

More recently the technique of chemical vapour deposition (CVD) has proved successful for diamond synthesis [67]. In contrast to the HPHT method, the CVD method takes place at much lower pressures and somewhat lower temperatures — occurring in a different region of the carbon phase diagram, Figure 1.6. A carbon-rich gas, typically methane (CH_4), is pumped into a reaction chamber (accompanied by hydrogen (H_2) and oxygen (O_2) to enhance growth conditions) where either a hot filament or a microwave source heats the gases to the extent that they are ionised and a plasma is formed. In this region of the phase diagram graphitic bonds are favoured, but these are also etched more rapidly by the plasma. The balance of these dynamic processes favours the gradual accumulation of diamond bonds.
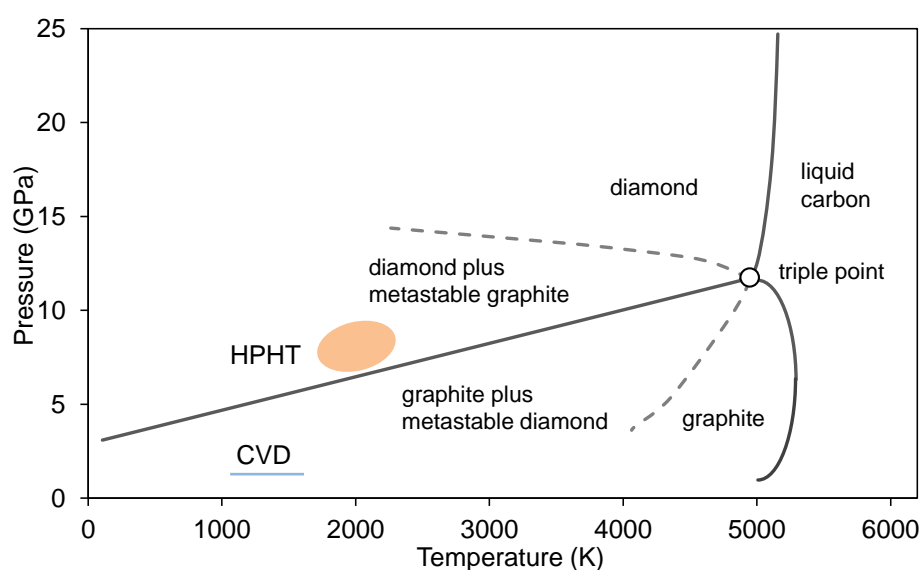
Figure 1.6: The carbon phase diagram. The high-pressure high-temperature (HPHT) and chemical vapour deposition (CVD) diamond formation regions are marked in orange and blue respectively. Figure adapted from [60].

Hence, the newly created carbon free radicals adhere to seed diamond material (either particles on a substrate or bulk material) previously loaded into the reaction chamber. The process initially suffered from slow growth rates, however, samples can now be grown in excess of $1\,\mu m/h$ [68–71]. Due to the high degree of control over the quality of gases injected into the reaction chamber CVD diamond growth has become a popular fabrication method for scientific samples.

1.4.2   Colour Centre Inclusion

Various methods for enhancing the number of colour centres in diamond exist — some tied with the synthesis process and others independent of the growth method. The complexity of these methods vary widely, from relatively simple processes to those requiring multiple steps and elaborate procedures. A subset of these methods containing those most common is listed below.

Atmospheric Inclusion

Nitrogen is the principle impurity in natural diamond material and is responsible for a large number of impurity-related centres. Nitrogen has a high affinity to be incorporated into the diamond lattice due to the number of electrons present in the valence band. Should nitrogen be present in the growth environment it is extremely likely to be included in the lattice of the growing crystal. As such, the amount of nitrogen present during diamonds HPHT growth process influences the concentration of nitrogen related defects in the grown crystals. This inclusion process can be used for the creation of fluorescent nanodiamonds containing high concentrations of NV centers.

Incorporation via CVD Growth

The inclusion of colour centres via CVD growth is undertaken by introducing the desired dopant into the reaction chamber. This can be achieved by either choosing the appropriate substrate or by introducing a dopant as a gas. In the case of the NV centre, even without purposefully injecting nitrogen into the reaction chamber the formation of NV centres occurs due the abundance of nitrogen in the atmosphere — even with the CVD reaction chamber reduced to low-pressure there exists enough residual nitrogen to result in NV formation. To be more accurate, it is most probable that the included nitrogen atom is lodged in the diamond lattice without a neighbouring vacancy. The NV complex can then be created by methods such as the combination of irradiation and annealing (see below). Occasionally NV centres still form completely, and it has been shown that the parameters inside the reactor can be controlled to manipulate the concentration of NVs generated [72].

Ion Implantation

Implantation of ions into the diamond lattice can be achieved through the use of a focused ion beam [73–75]. Ions are accelerated and bombard the host matrix, becoming implanted at depths dependent on the acceleration energy. Ion implantation is typically conduced in conjunction with annealing (covered in the following section) which enables the migration of vacancies through the lattice (and allowing for the creation of colour centres requiring vacancies) [76, 77]. This method allows for both the density and locations of implanted ions to be controlled to a certain degree [78, 79].

Irradiation and Annealing

To enhance the creation of colour centres requiring vacancies, a process of irradiation and subsequent annealing of diamond samples is usually undertaken [40, 80, 81]. A focused electron beam can be used to 'bump' carbon atoms from their sp^3 lattice position, leaving vacancies in the lattice. With the vacancies created, the sample can be annealed (at a temperature greater than ~850 °C [81]) to enable the migration of vacancies into energetically favourable locations, such as adjacent to nitrogen atoms [53, 82].

1.5   NV Applications

Colour centres in diamond are at the vanguard of room-temperature quantum technologies and quantum-enabled sensors. Due to the abundance of nitrogen in the Earth's chemistry NV defects are common in natural diamonds, however, in concentrations too high to be utilised in quantum technologies. Enabled through advances in synthetic diamond growth, the first single-site NV defect was observed in 1997 [51]. Since then, the NV has proven itself as a robust solid-state single-photon source [83–85], demonstrating the absence of photobleaching [85] and only exhibiting blinking when confined in nanodiamonds with sizes on the order on 5 nm [86]. Further investigations have also been conducted towards electrically driving the NV for use as a deterministic single-photon source [87]. This feature has led to NV centres finding use as a viable tool for quantum cryptography [88, 89], and with suitable control may eventually find application in room-temperature optical quantum information processing [90].

The energy level structure of the NV (§ 1.3.2) enables its use as a solid-state qubit [19, 91] — allowing for state initialisation, manipulation, and readout (the satisfaction of DiVincenzo's qubit requirements [92]). This ability has led to the use of the NV for fundamental quantum experiments concerning non-classical states, such as Bell state violation [93]. Spin coupling of two NV centres has been demonstrated, generating efforts towards the development of scalable NV-based multi-qubit systems [94, 95].

The previously mentioned susceptibility to splitting of the ground state $m_s = \pm 1$ sub-levels in the presence of a magnetic field (§ 1.3.2) makes the NV an excellent magnetic sensor. The degeneracy of the state lifts with a field strength of merely $4\,\mathrm{nT}\,\mathrm{Hz}^{-1/2}$ [2], and the degree of splitting is directly proportional to the magnetic field strength (§ 2.1.1). This effect can be read-out through the application of a combination of laser and microwave fields (§ 1.3.2) via the process of optically detected magnetic resonance imaging (ODMR), demonstrated in both bulk diamond [96] and in nanodiamond [86], and implemented in Chapter 2. Through modifications to the ODMR pulse sequence detection of magnetic fields generated from single spins has been detected [58, 59].

Nanodiamonds containing colour centres have also found application in biomedical science due to their small size (tens of nm) and biological inertness [97]. These properties, in addition to the NV fluorescence properties, allow the NV to be used a photostable bio-marker able to be tracked spatially as nanodiamonds traverse through living cells [5].

1.6 Confocal Fluorescence Microscopy

The primary method for optically probing ND crystals is through the use of a fluorescence confocal microscope. Confocal microscopes create sharp images by using point-by-point excitation and detection in a configuration that rejects out-of-focus light. The principle was first realised in 1955 [98] and has since continued to find application as a tool for probing microscopic systems. Compared to a conventional wide-field fluorescence microscope, where the excitation source illuminates the entire sample concurrently, a confocal microscope illuminates only a single spatial point and is able to reject light that is scattered outside of the focal plane.

In a traditional confocal microscope this is achieved by focusing initially divergent light onto a sample, and subsequently collecting this light after passing it through a pinhole, as illustrated in Figure 1.7a. Light generated outside of the focal plane is rejected by the pinhole placement, and hence is not incident on the detector. The size of the pinhole has important implications for the capabilities of the confocal system. It defines the optical sectioning capability of the microscope, and affects the achievable resolution and contrast. Initially it could be thought that the size of the pinhole should be reduced as small as possible to better reject out-of-the-plane scattered light. However, a trade-off must be made for detection efficiency, as decreasing the pinhole size also limits the number of photons arriving at the detector, which will decrease the signal-to-noise ratio.

By scanning the illuminated volume ('voxel') a sharply focused slice of the sample can be imaged. This slice is typically conducted the in xy plane, which is appropriate for our applications imaging ND and nanoparticles in general. However, imaging three-dimension volumes can be achieved by stitching together multiple slices of the sample.

Our constructed confocal microscope is modified from the original design. A laser is used as our excitation source, and pinholes are replaced with single-mode optical fibres, see

Figure 1.7b. These substitutions allow for a bright excitation source, where the laser source can be tailored to the excitation wavelength required for the experiment, and in the general enhanced flexibility of optical setup.

The single point illumination and detection provided by a confocal microscope increases imaging resolution at the expense of time required to create an image, as the illuminated voxel must be raster scanned to form a larger intensity map. However, the increased sensitivity of the system to small, weak light sources enables NDs containing single colour centre defects to be imaged and optically addressed.
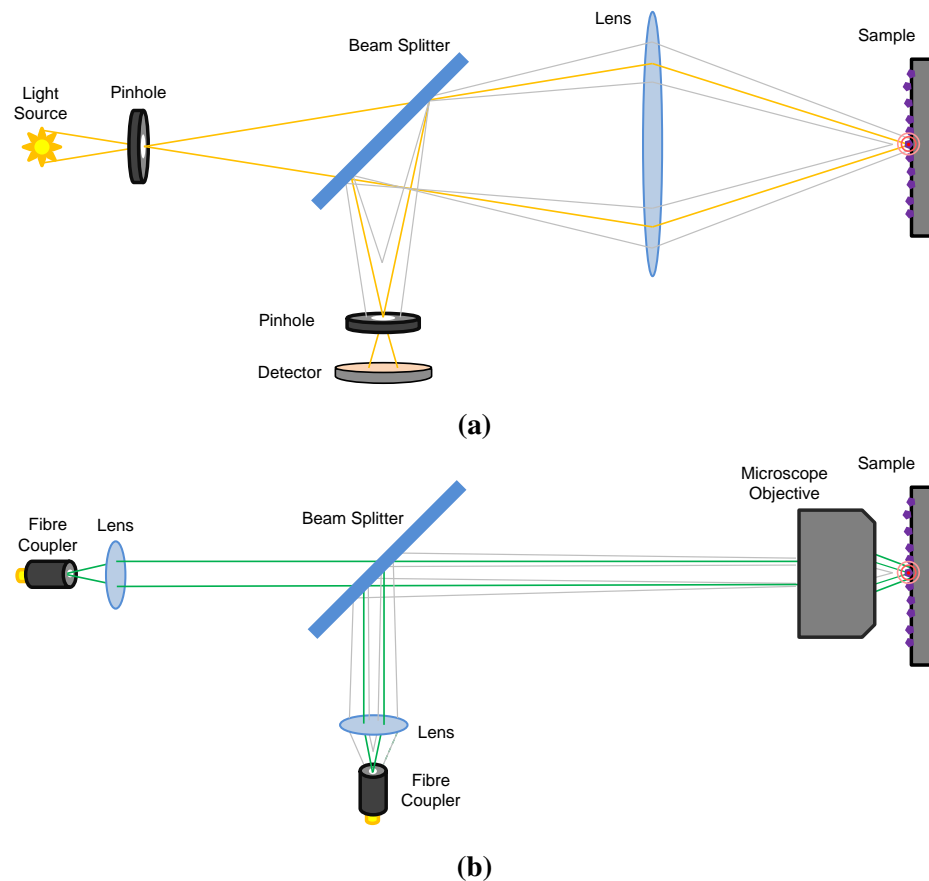
Figure 1.7: Schematic representation of a traditional and modern confocal microscope designs. In both cases only light originating from the sample plane is able to pass through to the detection path. Rejected ray paths are shown in gray. **(a)** A traditional confocal microscope design utilising light from a non-coherent source (shown as yellow rays). The light is first passed through a pinhole, through a beamsplitter, and focused onto the sample. A second pinhole is placed in front of the detector a focal distance away from the focusing lens. Now, only light originating from the focal plane can be incident on the detector — out-of-the-plane scattered light is rejected from passing through the second pinhole, and ultimately from the detector. **(b)** In a modern confocal microscope design, as we will be using repeatedly throughout this thesis, a laser is used as the illumination source (shown as green rays), the focusing lens replaced with a microscope objective, and the second pinhole with a single-mode optical fibre. These substitutions allow for the excitation source wavelength to be tailored to the experiment, and for increased flexibility in the optical design.

2

Coupling of Single NV Centres to a Microwave Cavity

"As for me, I am tormented with an everlasting itch for things remote. I love to sail forbidden seas, and land on barbarous coasts."

Herman Melville

A challenge in the development of NV-based nanodiamond technologies is the effective coupling of single NV centres to microwave fields for spin manipulation. The combination of laser and microwave fields allows for the initialisation, manipulation, and readout of the NV spin state — which is imperative for the use of the NV as a qubit. Conventional experimental methods resort to placing a stripline antenna in close proximity (on the order of $10\,\mu\text{m}$) to a nanodiamond hosting a colour centre. A typical stripline antenna can be as simple as a thin copper wire tens of μm in diameter. The main issues with this type of wire-antenna is that the material undergoes heating and expansion when acting as a microwave waveguide, and, direct heating due to mechanical contact between the antenna and the sample. The sample can thus be displaced (out of focus for optimal optical collection) or heated by tens of $^\circ$C (undesirable in experiments involving biological samples). While loop antennas exist to mediate the limitations of on-chip methods they require much more (orders of magnitude) power to generate equivalent field strengths.

To overcome these problems we developed a macroscopic microwave cavity which can generate a uniform microwave field some distance away (mm to cm) from the sample. The sample can be placed outside and without contact to the cavity, hence avoiding both sample heating and displacement. Such a cavity was developed shortly before the commencement of this project as a collaboration between our research group and the Frequency Standards and Metrology group at the University of Western Australia [99]. The cavity, discussed below, was successfully implemented and used to conduct optically detected magnetic resonance (ODMR) measurements (see § 1.3.2) on a single NV spin. This research is the continuation of that endeavour, attempting to use the cavity for coherent NV spin manipulation measurements. Prior to discussing our result, I first provide the theoretical backbone required to understand spin manipulation in the NV system.
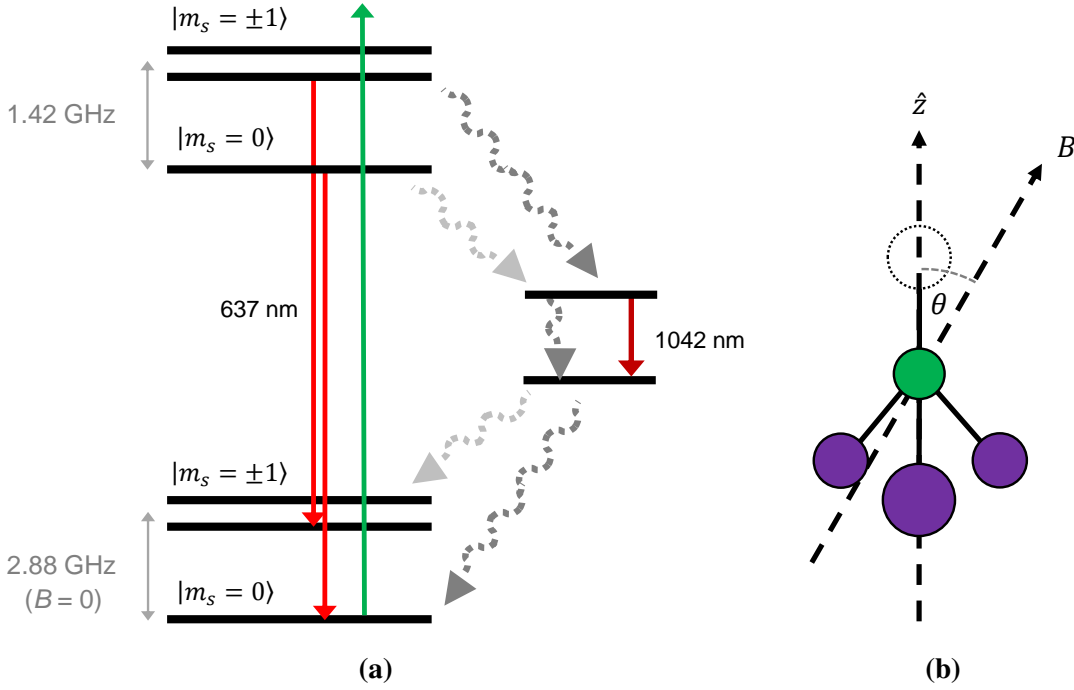
Figure 2.1: The Nitrogen-Vacancy centre in diamond. a) The energy level diagram of the NV, adapted from [100]. **b)** The NV defect in the diamond lattice, showing the conventionally selected z axis and annotated with an off-axis magnetic field (by some degree θ). Carbon atoms shown as purple, nitrogen atom as green, and vacancy as white.

2.1   Theoretical Backbone

Here I discuss various aspects of the spin physics of the NV centre. I will discuss the Hamiltonian of the NV centre, approximate it as a two-level system, and visualise the system geometrically on the Bloch sphere. I will then discuss Rabi frequency and Hahn spin-echo measurements in the context of using the NV as an effective spin qubit.

2.1.1   The NV Ground-State Hamiltonian

The ground state of the NV centre is described by the Hamiltonian [101]

$$\hat{\mathcal{H}}_{gs} = \hbar D_g S_z^2 + \hbar E \left(S_x^2 + S_y^2 \right) + \underbrace{g_e \mu_B \mathbf{B} \cdot \mathbf{S}}_{\text{Zeeman interaction}} \tag{2.1}$$

where $D_g/2\pi \simeq 2.88\,\text{GHz}$ is the zero-field energy difference between the $m_s = 0$ and $m_s = \pm 1$ states, E is the strain induced splitting of the $m_s = \pm 1$ state, g_e is the electron g-factor, μ_B is the Bohr magneton, $\mathbf{B}$ is the magnetic field vector, and $\mathbf{S}\left(S_x, S_y, S_z \right)$ are the Pauli matrices for spin-1 operators.

In matrix form the Hamiltonian is

$$\hat{\mathcal{H}}_{gs} = \begin{pmatrix} \hbar D_g + g_e \mu_B B_z & 0 & \hbar E \\ 0 & 0 & 0 \\ \hbar E & 0 & \hbar D_g - g_e \mu_B B_z \end{pmatrix} \tag{2.2}$$

in the $(m = +1, m = 0, m = -1)$ basis and assuming the external applied magnetic field is along the $\hat{z}$ direction. To determine the energy levels of the system we diagonalise the
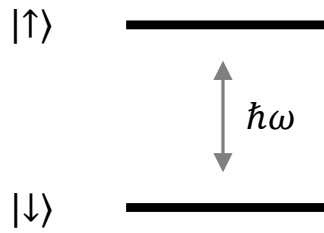
Figure 2.2: A typical two-level atom. The ground, $|\downarrow\rangle$, and excited, $|\uparrow\rangle$, states are annotated, and separated by some energy $\hbar\omega$.

matrix. To do so we solve the Hamiltonian time-independent Schrödinger equation, which will produce the energy eigenvalues of the system as per appendix note A.1. This has the solutions

$$\lambda = \hbar D_g \pm \sqrt{(\hbar E)^2 + (g_e \mu_B B_z)^2}$$
(2.3)

Note that the degeneracy of the $m_s = \pm 1$ state is lifted either by strain, E, or by the magnetic field (i.e. the component along the $\hat{z}$ direction, B_z as per Figure 2.1b, is non-zero). The $m_s = -1$ and $m_s = +1$ levels thus become resolvable in energy. On average, only $\sim 15\%$ of the NV centres in diamond do not display a zero-field splitting of the $m_s = \pm 1$ state (mainly because there is always some residual strain that lifts the degeneracy) [51].

2.1.2   The Interaction Hamiltonian

In the case where the $m_s = \pm 1$ levels are not split, the NV can be considered a pseudo spin-1/2 system[i] and treated as a simple two-level system with the corresponding spin-algebra, Figure 2.2.

The Hamiltonian for such a system is

$$\hat{\mathcal{H}} = 0\,|\downarrow\rangle\langle\downarrow| + \hbar\omega\,|\uparrow\rangle\langle\uparrow| + \frac{\Omega}{2}\left(|\uparrow\rangle\langle\downarrow| + |\downarrow\rangle\langle\uparrow|\right)$$
(2.4)

where $|\downarrow\rangle$ and $|\uparrow\rangle$ represent the ground and excited states, $\Omega_R = Ed/\hbar$ is the Rabi frequency, and d is the dipole moment. The Rabi frequency gives the rate at which the electron can cycle through two atomic levels in the light field. In matrix form, this Hamiltonian is

$$\hat{\mathcal{H}} = \begin{pmatrix} 0 & \Omega/2 \\ \Omega/2 & \hbar\omega \end{pmatrix}$$
(2.5)

We now consider the off-diagonal elements as the interaction Hamiltonian.

$$\hat{\mathcal{H}}_{int} = \frac{\Omega}{2}\left(|\downarrow\rangle\langle\uparrow| + |\uparrow\rangle\langle\downarrow|\right)$$
(2.6)

$$= \begin{pmatrix} 0 & \Omega/2 \\ \Omega/2 & 0 \end{pmatrix}$$
(2.7)

In the absence of a driving field, $\Omega = 0$, the system — as expected — does not evolve. To examine the system when driven by a field we can either solve the Schrödinger equation,

---

[i]In the case that there exists some degree of splitting, but the detuning is small, then the Rabi frequency is only altered by some small degree $\Omega_R = \sqrt{\Omega^2 + (\omega - \omega_0)^2}$.

or look at the unitary evolution of the system. Both of these approaches are presented in appendix note A.2, and both produce the following population solutions. The probability of the system being in the ground state is[ii]

$$P_\downarrow = |\alpha|^2 \tag{2.8}$$

$$= \cos^2\left(\frac{\Omega t}{2\hbar}\right) \tag{2.9}$$

and the probability of being in the excited state

$$P_\uparrow = |\beta|^2 \tag{2.10}$$

$$= \sin^2\left(\frac{\Omega t}{2\hbar}\right) \tag{2.11}$$

Notably, we observe that the population becomes fully inverted when

$$\frac{\Omega t}{\hbar} = \pi \tag{2.12}$$

and in an 'equal' superposition when

$$\frac{\Omega t}{\hbar} = \frac{\pi}{2} \tag{2.13}$$

This is the origin for the commonly used terms π-pulse (full inversion) and $\pi/2$-pulse (superposition).

2.1.3   Phase of a State

I now introduce some phase ϕ to the quantum state. The state now takes the form

$$|\downarrow\rangle = \begin{pmatrix} e^{i\phi} \\ 0 \end{pmatrix} \tag{2.14}$$

This state still satisfies the condition $\left|e^{i\phi}\right|^2 = 1$, and as such is still represented as $|\downarrow\rangle$, but with an extra phase ϕ. We must now make some distinctions between the global phase of a system, which is unmeasurable, and the relative phase of different parts of the same system, which gives rise to quantum interference phenomena. For the global phase

$$|\psi\rangle = \frac{1}{\sqrt{2}}\left(e^{i\phi}|\downarrow\rangle + e^{i\phi}|\uparrow\rangle\right) \tag{2.15}$$

$$= \frac{e^{i\phi}}{\sqrt{2}}(|\downarrow\rangle + |\uparrow\rangle) \tag{2.16}$$

with our definition above that each state $|\downarrow\rangle$ and $|\uparrow\rangle$ have some phase ϕ associated with them. As this phase is 'global' — that is to say that it affects the amplitudes of both states equally — there is no measurement that can be conducted to determine the global phase factor.

Alternatively if the phase is associated with only one of the state vectors, then we could conduct an interference experiment to determine the phase. Such a state with only a local phase would take the form

$$|\psi\rangle = \frac{1}{\sqrt{2}}\left(|\downarrow\rangle + e^{i\phi}|\uparrow\rangle\right) \tag{2.17}$$

[ii]True only if at $t = 0$ the state is entirely in the spin down (i.e. ground) state $|\downarrow\rangle$, with no spin up component.
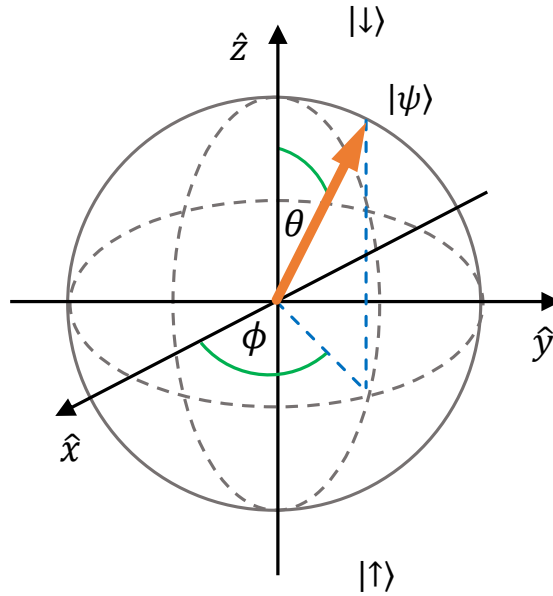
Figure 2.3: The Bloch sphere. A geometrical representation of a two-level quantum system. The projection of the state $|\psi\rangle$ onto the $\hat{z}$ axis gives the coefficients α and β.

2.1.4 The Bloch Sphere

The Bloch sphere provides a geometrical representation of the state space of a two-level quantum system, represented in Figure 2.3. The basis states of the system, in this case $|\downarrow\rangle$ and $|\uparrow\rangle$, are located at the poles of the sphere. For this section let us only consider states that lie on the surface of the Bloch sphere — these are known as pure states, and the vector that points to them from the centre of the Bloch sphere is known as the Bloch vector. A state on the surface of the sphere can be described by a state vector

$$|\psi\rangle = \frac{1}{\sqrt{2}} \left(\cos\left(\frac{\theta}{2}\right) |\downarrow\rangle + e^{i\phi} \sin\left(\frac{\theta}{2}\right) |\uparrow\rangle \right) \tag{2.18}$$

$$= \frac{1}{\sqrt{2}} \left(\cos\left(\frac{\theta}{2}\right) |\downarrow\rangle + (\cos\phi + i\sin\phi) \sin\left(\frac{\theta}{2}\right) |\uparrow\rangle \right) \tag{2.19}$$

where $0 \leq \theta \leq \pi$ and $0 \leq \phi \leq 2\pi$, providing a unique mapping between the wavefunction amplitudes α and β.

2.1.5 Rotations on the Bloch Sphere

The state 'moves' across the surface of the Bloch sphere under a driving field that causes the state to 'rotate' about $\hat{x}$, $\hat{y}$, or $\hat{z}$ axis. When the system is initialised into the ground state $|\downarrow\rangle$ the choice of the angle of rotation about $\hat{z}$ is arbitrary, so we choose the 'rotational orientation' of the xy plane such that it is convenient.

To demonstrate the process, let the first pulse induce a rotation about the $\hat{x}$ axis by an amount $\pi/2$, such that the state now lies on the equator (superposition). Recall from § A.2 that this state is now in an 'equal' superposition of our two basis states. For all rotations after this initial pulse, the axis around which the Bloch vector rotates is determined by the phase of the pulse relative to that of the first. Some series of rotations[iii], known as pulse sequences, can induce rotations about both the $\hat{x}$ or $\hat{y}$ axes by inducing a relative phase of $90\,^\circ$ between

the pulse that moves the Bloch vector to the equator and the pulse that rotates around the $\hat{x}$ or $\hat{y}$ axis. If the initial pulse rotated the Bloch vector about the $\hat{x}$ axis, then this second pulse would rotate the vector about the $\hat{y}$ axis.

The rotation angle, Θ, is described by

$$\Theta = \left| \frac{d}{\hbar} \int_{-\infty}^{+\infty} E(t) \, dt \right| \tag{2.20}$$

$$= \frac{dEt}{\hbar} \tag{2.21}$$

$$= \frac{\Omega t}{\hbar} \tag{2.22}$$

where d is the dipole moment for the $|\downarrow\rangle \rightarrow |\uparrow\rangle$ transition and E is the time-dependent electric field amplitude of the pulse. We can observe that if we initially start in the ground state $|\downarrow\rangle$ and apply a π-pulse, which is $\Omega t/\hbar = \pi$ then we move to the excited state $|\uparrow\rangle$ (full inversion). Similarly, if again we start in the ground state and apply a $\pi/2$-pulse, we end up on the equator of the Bloch sphere, where $|\psi\rangle = 1/\sqrt{2}\,(|\downarrow\rangle + |\uparrow\rangle)$ (superposition).

I now consider the rate at which these state rotate about the axes of the Bloch sphere. The state will evolve under the unitary evolution as

$$|\psi(t)\rangle = \hat{U}(t) |\psi(0)\rangle \tag{2.23}$$

$$= \frac{1}{\sqrt{2}} e^{-\frac{it}{\hbar}\hat{\mathcal{H}}} \begin{pmatrix} 1 \\ 1 \end{pmatrix} \tag{2.24}$$

$$= \frac{1}{\sqrt{2}} \begin{pmatrix} 1 & 0 \\ 0 & e^{-it\omega} \end{pmatrix} \begin{pmatrix} 1 \\ 1 \end{pmatrix} \tag{2.25}$$

$$= \frac{1}{\sqrt{2}} \begin{pmatrix} 1 \\ e^{-it\omega} \end{pmatrix} \tag{2.26}$$

The state

$$|\psi(t)\rangle = \frac{1}{\sqrt{2}} \left(|\downarrow\rangle + e^{-it\omega} |\uparrow\rangle \right) \tag{2.27}$$

precesses around the equator at some rate ω. This is the Larmor frequency — the precession around the plane that is perpendicular to the magnetisation axis $\hat{z}$ (through the angle ϕ in Figure 2.3). Conversely, the frequency at which the state rotates through the polar angle θ is known as the Rabi frequency.

2.1.6 Within the Bloch Sphere

States that do not lie on the surface of the Bloch sphere are known as mixed states — they are states that have lost some degree of their quantum coherence. To describe such a state we make use of the density matrix. I consider first a pure state (one that lies on the surface of the Bloch sphere), then I build upon this framework to discuss the case of a mixed state. Consider again the generic pure state

$$|\psi\rangle = \cos\left(\frac{\theta}{2}\right) |\downarrow\rangle + e^{i\phi} \sin\left(\frac{\theta}{2}\right) |\uparrow\rangle \tag{2.28}$$

[iii]CPMG and XY8 are 'common' pulse sequences used with the NV centre that use rotations about both the $\hat{x}$ and $\hat{y}$ axes on the Bloch sphere.

The corresponding density matrix for this generic state is

$$\rho \equiv |\psi\rangle\langle\psi| \tag{2.29}$$

$$= \left(\cos\left(\frac{\theta}{2}\right)|\downarrow\rangle + e^{i\phi}\sin\left(\frac{\theta}{2}\right)|\uparrow\rangle\right)\left(\cos\left(\frac{\theta}{2}\right)\langle\uparrow| e^{-i\phi}\sin\left(\frac{\theta}{2}\right)\langle\downarrow|\right) \tag{2.30}$$

$$= \cos^2\left(\frac{\theta}{2}\right)|\downarrow\rangle\langle\downarrow| + e^{-i\phi}\cos\left(\frac{\theta}{2}\right)\sin\left(\frac{\theta}{2}\right)|\downarrow\rangle\langle\uparrow|$$

$$+ e^{i\phi}\cos\left(\frac{\theta}{2}\right)\sin\left(\frac{\theta}{2}\right)|\uparrow\rangle\langle\downarrow| + \sin^2\left(\frac{\theta}{2}\right)|\uparrow\rangle\langle\uparrow| \tag{2.31}$$

$$= \begin{pmatrix} \cos^2\left(\frac{\theta}{2}\right) & e^{-i\phi}\cos\left(\frac{\theta}{2}\right)\sin\left(\frac{\theta}{2}\right) \\ e^{i\phi}\cos\left(\frac{\theta}{2}\right)\sin\left(\frac{\theta}{2}\right) & \sin^2\left(\frac{\theta}{2}\right) \end{pmatrix} \tag{2.32}$$

To account for the decay from a pure state to a mixed state, I introduce an exponential term to reduce the off-diagonal elements of the density matrix over time

$$\rho = \begin{pmatrix} \cos^2\left(\frac{\theta}{2}\right) & e^{-\gamma t}e^{-i\phi}\cos\left(\frac{\theta}{2}\right)\sin\left(\frac{\theta}{2}\right) \\ e^{-\gamma t}e^{i\phi}\cos\left(\frac{\theta}{2}\right)\sin\left(\frac{\theta}{2}\right) & \sin^2\left(\frac{\theta}{2}\right) \end{pmatrix} \tag{2.33}$$

where γ is the decay rate induced by the dephasing of the system.

2.1.7 Measurement

The expectation value is the probabilistically expected value of the result of a measurement. To calculate the expectation value we multiply the density matrix by the measurement axis, in this case σ_z, and take the trace

$$\langle\sigma_z\rangle = Tr\left[\hat{\rho}\sigma_z\right] \tag{2.34}$$

$$= Tr\left[\begin{pmatrix} \cos^2\left(\frac{\theta}{2}\right) & e^{-\gamma t}e^{-i\phi}\cos\left(\frac{\theta}{2}\right)\sin\left(\frac{\theta}{2}\right) \\ e^{-\gamma t}e^{i\phi}\cos\left(\frac{\theta}{2}\right)\sin\left(\frac{\theta}{2}\right) & \sin^2\left(\frac{\theta}{2}\right) \end{pmatrix}\begin{pmatrix} 1 & 0 \\ 0 & -1 \end{pmatrix}\right] \tag{2.35}$$

$$= Tr\left[\begin{pmatrix} \cos^2\left(\frac{\theta}{2}\right) & -e^{-\gamma t}e^{-i\phi}\cos\left(\frac{\theta}{2}\right)\sin\left(\frac{\theta}{2}\right) \\ e^{-\gamma t}e^{i\phi}\cos\left(\frac{\theta}{2}\right)\sin\left(\frac{\theta}{2}\right) & -\sin^2\left(\frac{\theta}{2}\right) \end{pmatrix}\right] \tag{2.36}$$

We find that

$$\langle\sigma_z\rangle = \cos^2\left(\frac{\theta}{2}\right) - \sin^2\left(\frac{\theta}{2}\right) \tag{2.37}$$

and we recover that if $\theta = 0$ then $Tr\left[\sigma_z\right] = 1$, corresponding to $|\uparrow\rangle$, and if $\theta = \pi$ then $Tr\left[\sigma_z\right] = -1$, corresponding to $|\downarrow\rangle$.

2.1.8 Relaxation, Dephasing, and Decoherence

To properly understand the transition of the system from a pure state to a mixed state we must make some distinctions of terms, some of which are often used interchangeably.

Relaxation T_1

The spin-lattice relaxation rate, T_1, is the rate at which a system returns to thermal equilibrium with the surrounding lattice — it is the rate at which a system relaxes into its equilibrium state given by the Boltzmann distribution. In our two-level system this is represented by the Bloch vector moving to the ground state $|\downarrow\rangle$, illustrated in Figure 2.4a.

(a)　　　　　　　　　　　　　　　　　　　　**(b)**
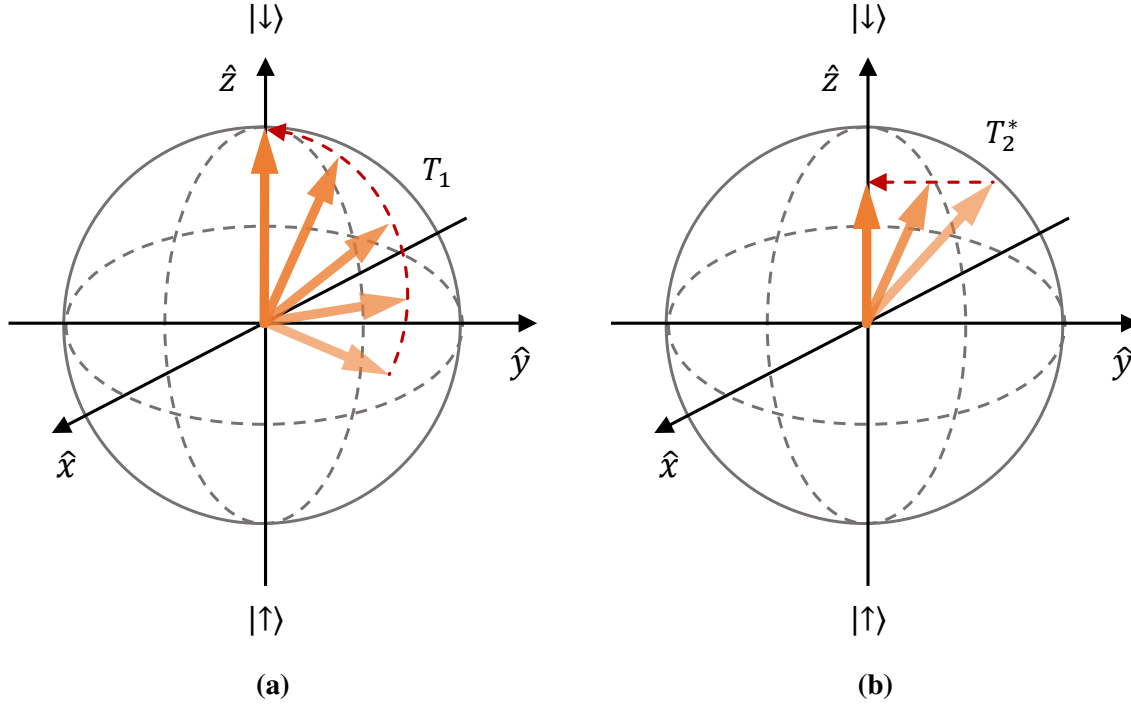
Figure 2.4: T_1 **and** T_2^* **illustrated on the Bloch sphere.** Adapted from [102]. **a)** Spin-lattice relaxation. This relaxation into the ground state occurs at a rate T_1. This is represented by the state transitioning towards $|\downarrow\rangle$ **b)** Spin-spin dephasing. This transition from a pure state to a mixed state occurs at the rate T_2^*. This is represented by the shortening of the Bloch vector.

Dephasing T_2^*

The spin-spin relaxation time, T_2^*, is the rate at which a pure state decays into a mixed state. On the Bloch sphere this is represented by the shortening of the Bloch vector — the vector coming off the surface of the Bloch sphere, Figure 2.4b.

T_2^* dephasing is a result of a magnetic field inhomogeneity introduced by surrounding spins and interactions with nearby surface states. The slow- or non-varying component of T_2^*, written as T_2, can be reversed by measurement procedures like the Hahn spin-echo sequence, which will be described below. Removing the slow- or non-varying component of the environment reveals the underlying rate at which the system transitions to a mixed state — the decoherence rate T_2'. This rate is intrinsic to the system and it does not take into account magnetic field gradient fluctuation. This is represented by the equation

$$\frac{1}{T_2^*} = \frac{1}{T_2} + \frac{1}{T_2'} \tag{2.38}$$

$$= \frac{1}{T_2} + \gamma \Delta B_0 \tag{2.39}$$

where T_2' is the inhomogeneous dephasing, γ is the gyromagnetic ratio, and ΔB_0 is deviation from the local B field. The overall spin-spin relaxation time T_2^* will always be shorter than the intrinsic dephasing rate T_2', which in turn is, almost always, shorter than the spin-lattice relaxation rate T_1.

Incorporating T_2^* into the density matrix representing our two-level system

$$\rho = \begin{pmatrix} \cos^2\left(\frac{\theta}{2}\right) & e^{-\frac{t}{T_2^*}} e^{-i\phi} \cos\left(\frac{\theta}{2}\right) \sin\left(\frac{\theta}{2}\right) \\ e^{-\frac{t}{T_2^*}} e^{i\phi} \cos\left(\frac{\theta}{2}\right) \sin\left(\frac{\theta}{2}\right) & \sin^2\left(\frac{\theta}{2}\right) \end{pmatrix} \tag{2.40}$$

we can see that when $t \gg T_2^*$ the off-diagonals decay to zero and the system transitions to a mixed state

$$\rho_{t \gg T_2^*} = \begin{pmatrix} \cos^2\left(\frac{\theta}{2}\right) & 0 \\ 0 & \sin^2\left(\frac{\theta}{2}\right) \end{pmatrix} \tag{2.41}$$

where, if the Bloch vector lies on the equator, $\theta = \pi/2$, then the system will be found with equal probability in either the ground $|\downarrow\rangle$ or excited $|\uparrow\rangle$ state

$$\rho_{t \gg T_2^*, \theta = \pi/2} = \begin{pmatrix} {}^1/_2 & 0 \\ 0 & {}^1/_2 \end{pmatrix} \tag{2.42}$$

This loss of off-diagonal coherence of the density matrix is clearly non-unitary. However, it is important to remember that this is a high-level heuristic description. Some of this loss of coherence arises from the fact that individual atoms experience different energy shifts due to their local environment. If these energy shifts can be reversed we can regain the coherence. This is the difference between T_2 and T_2'. To demonstrate how the effects of T_2 can be reversed we consider a case where an atom has its excited state energy shifted by ϵ. The interaction Hamiltonian then takes the appearance

$$\hat{\mathcal{H}}_{int} = \begin{pmatrix} 0 & \Omega/2 \\ \Omega/2 & \epsilon \end{pmatrix} \tag{2.43}$$

where ϵ is the deviation in energy from the unperturbed energy level separation. We repeat the unitary evolution process of the ground state $|\downarrow\rangle$, previously undertaken in § A.2. For neatness[iv] we will let $\kappa = \sqrt{\epsilon^2 + \Omega^2}$.

$$|\psi(t)\rangle = \hat{U}(t) |\psi(0)\rangle \tag{2.44}$$

$$= e^{\frac{it}{\hbar} \hat{\mathcal{H}}_{int}} |\psi(0)\rangle \tag{2.45}$$

$$= \exp\left[\frac{it}{\hbar} \begin{pmatrix} 0 & \Omega/2 \\ \Omega/2 & \epsilon \end{pmatrix}\right] \begin{pmatrix} 1 \\ 0 \end{pmatrix} \tag{2.46}$$

$$= \begin{pmatrix} e^{-\frac{it\epsilon}{2\hbar}} \left(\kappa \cos\left(\frac{\kappa t}{2\hbar}\right) + i\epsilon \sin\left(\frac{\kappa t}{2\hbar}\right)\right) & -ie^{-\frac{it\epsilon}{2\hbar}} \frac{\Omega \sin\left(\frac{\kappa t}{2\hbar}\right)}{\kappa} \\ -ie^{-\frac{it\epsilon}{2\hbar}} \frac{\Omega \sin\left(\frac{\kappa t}{2\hbar}\right)}{\kappa} & e^{-\frac{it\epsilon}{2\hbar}} \left(\kappa \cos\left(\frac{\kappa t}{2\hbar}\right) - i\epsilon \sin\left(\frac{\kappa t}{2\hbar}\right)\right) \end{pmatrix} \begin{pmatrix} 1 \\ 0 \end{pmatrix} \tag{2.47}$$

$$= \begin{pmatrix} e^{-\frac{it\epsilon}{2\hbar}} \left(\kappa \cos\left(\frac{\kappa t}{2\hbar}\right) + i\epsilon \sin\left(\frac{\kappa t}{2\hbar}\right)\right) \\ -ie^{-\frac{it\epsilon}{2\hbar}} \frac{\Omega \sin\left(\frac{\kappa t}{2\hbar}\right)}{\kappa} \end{pmatrix} \tag{2.48}$$

$$= \begin{pmatrix} \alpha(t) \\ \beta(t) \end{pmatrix} \tag{2.49}$$

Using these probability coefficients we can again calculate the probability of being in the ground state

$$P_\downarrow = |\alpha|^2 \tag{2.50}$$

$$= \cos^2\left(\frac{\sqrt{\epsilon^2 + \Omega^2}}{2\hbar} t\right) + \frac{\epsilon^2}{\epsilon^2 + \Omega^2} \sin^2\left(\frac{\sqrt{\epsilon^2 + \Omega^2}}{2\hbar} t\right) \tag{2.51}$$

[iv]Read as 'so that this matrix will fit on the page'

We can see that when $\epsilon = 0$ we recover $|\alpha|^2 = \cos^2(\Omega t/2\hbar)$, as in § A.2 where we neglected the dephasing. Similarly, we can calculate the probability of being in the excited state

$$P_\uparrow = |\beta|^2 \tag{2.52}$$

$$= \frac{\Omega^2}{\epsilon^2 + \Omega^2} \sin^2\left(\frac{\sqrt{\epsilon^2 + \Omega^2}}{2\hbar}t\right) \tag{2.53}$$

and again with $\epsilon = 0$ we recover the case where we did not consider dephasing; $|\beta|^2 = \sin^2(\Omega t/2\hbar)$. The insight is that depending on the energy shift ϵ the probabilities will evolve at different rates in time. So, if the local environments of individual atoms are different, with different excited state energy shifts, they become out of phase with each other. In the Bloch sphere picture we no longer represent this as a path but as a wedge on the surface of the sphere that expands as the state traverses the surface, Figure 2.5. In this picture the expectation value $\langle \sigma_z \rangle$ can be interpreted as the ratio between the sphere enclosed by the wedge above and below the equator. At short time scales this ratio can be determined with some certainty but at longer time scales the ratio tends towards parity, indicating equal probability of the system being found in either the ground $|\downarrow\rangle$ or excited $|\uparrow\rangle$ state. T_2^* is the time after which the ratio surpasses a difference of $1/e$, where we no longer know the state with certainty (i.e. loss of coherence). But, if this energy shift could be reversed it would be possible to evolve all the atoms back into phase, removing the effect of T_2. We can achieve this reversal by techniques such as the Hahn spin-echo sequence, which will be discussed in § 2.1.9.

Decoherence T_2'

Decoherence is the irreversible loss of phase information of the system to the environment; it can be thought of as the system losing its information via loss of its set quantum state. The difference between decoherence and dephasing is in that if it is known how the system has dephased we can perform actions to re-phase the system, see § 2.1.9, while we cannot reverse decoherence. In the Bloch sphere picture this is represented by the shortening of the Bloch vector, as we saw in § 2.1.6 discussing transitions from a pure state to a mixed state, and as illustrated in Figure 2.4b. This is the T_2' time, as opposed to the T_2^* time which is the combination of both the T_2 dephasing time and the T_2' decoherence time, as per Equation 2.39. Again, it can be thought of by the decay of the off-diagonal elements of the density matrix, seen previously in Equation 2.40.

2.1.9   Spin Measurements

To determine the values of the Rabi frequency, Ω_R, and the spin-spin dephasing rate, T_2^*, we can implement specific sequences of pulses to initialise, manipulate, and readout[v] the state of our two-level system. Long T_2^* times (coherence times) are a technologically desirable characteristic for quantum spin systems. A long coherence time allows for a period of time after the initialisation of the system that the spin state and be manipulated and read-out before the information is lost due to interactions with the environment. For these examples we will still consider our generic two-level system, and subsequently discuss them in the context of the NV centre. Let us imagine we have control over some field that can be used to initialise the system deterministically into the ground state $|\downarrow\rangle$, while some other field can drive the

---

[v]Recall that the ability to undertake these actions are the three core requirements for a qubit [92].
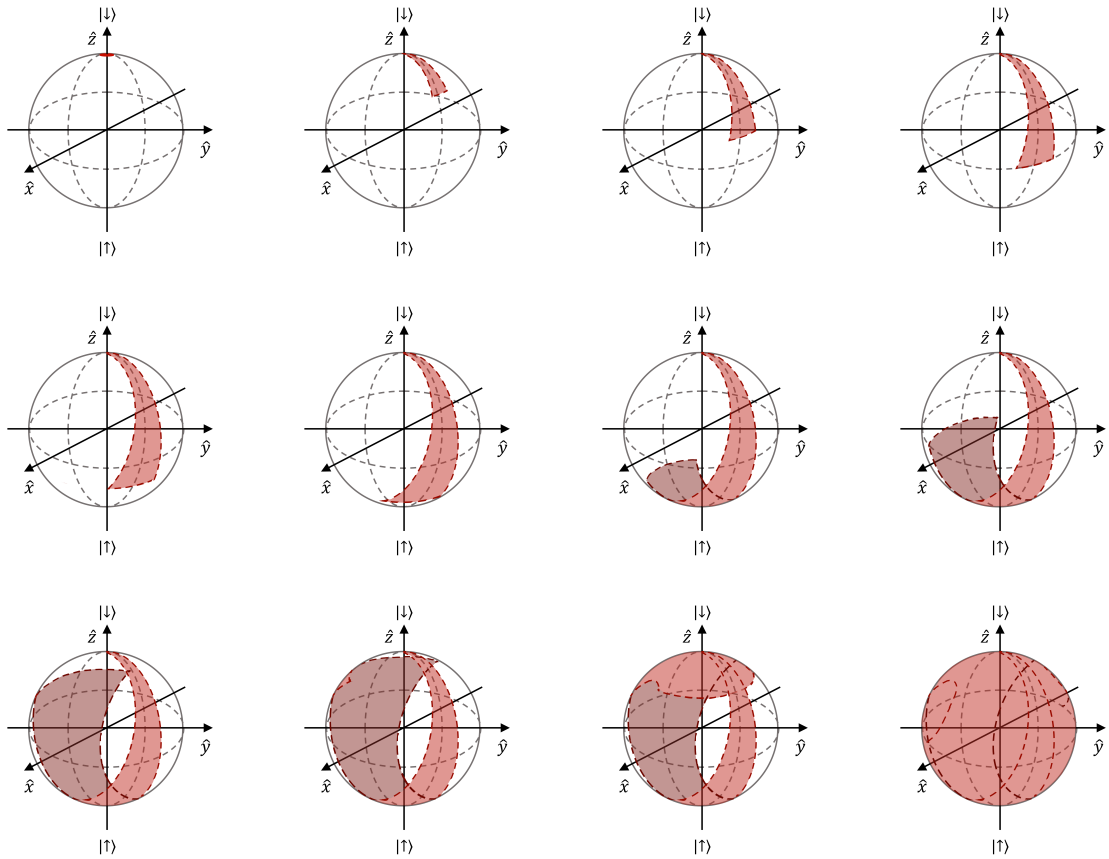
Figure 2.5: Dephasing represented on the Bloch sphere. We represent the phase uncertainty of the driven evolution of our state as a wedge on the Bloch sphere. As $t \gg T_2^*$ the uncertainty spans the Bloch sphere, the information about the state is lost, and when a measurement is undertaken the state will be read-out with equal probability $|\downarrow\rangle$ or $|\uparrow\rangle$.

state from $|\downarrow\rangle$ to $|\uparrow\rangle$. We also have some apparatus which allows us to make a measurement of which state the system is in.

Rabi Frequency Measurement

Measuring the Rabi frequency of a given two-level system requires undertaking a specific sequence which determines both the π-pulse duration and the characteristic T_2^* time. Recall from § A.2 that the probability of the system being in the excited state is $P_\downarrow = \cos^2\left(\Omega t/2\hbar\right)$; if we apply a π-pulse then we the system is driven from its ground to excited state.

Therefore for this sequence our procedure is as follows. First, a field is applied to initialise the system into the ground state. Next, we apply the required field to drive the state towards the excited state (a rotation through the polar angle Θ in our Bloch sphere diagram, Figure 2.3). If we only apply this driving field for some short time scale, insufficient to fully invert from $|\downarrow\rangle$ to $|\uparrow\rangle$ on the Bloch sphere, and then perform a readout (state projection) measurement the system will still be 'in average' in the ground state (the amplitude coefficients are $|\alpha|^2 \sim 1$, $|\beta|^2 \sim 0$). If then we repeat this sequence and gradually expand the duration of the driving field [vi] we will eventually 'move' closer to the excited state $|\uparrow\rangle$ (full inversion). This is reflected in our measured α and β values, and we will have slowly transitioned from $|\alpha|^2 \sim 1$, $|\beta|^2 \sim 0$ to $|\alpha|^2 \sim 0$, $|\beta|^2 \sim 1$ when we achieve a π-pulse, illustrated as oscillations
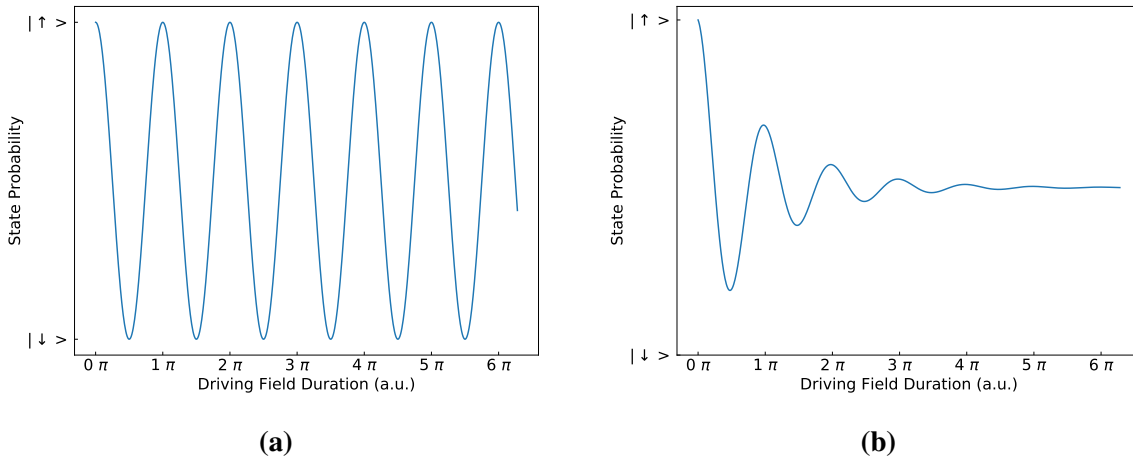
Figure 2.6: Simulated Rabi and Hahn-echo data. (a) Simulated measurements of the Rabi cycle, showing the system oscillating between the ground $|\downarrow\rangle$ and excited $|\uparrow\rangle$ states, and decohering over time into a mixed state where $\alpha = \beta$. (b) Simulated T_2 decay data, showing the spin-echo signal.

in Figure 2.6a. If we continue to increase the duration of the driving field pulse from this point we 'overshoot' $|\uparrow\rangle$ on the Bloch sphere, and start returning to the $|\downarrow\rangle$ state. This cycle will continue indefinitely if there are no decay processes present, and is referred to as the Rabi cycle or Rabi flopping, with the Rabi frequency given by the rate at which we can drive a complete cycle around the Bloch sphere (i.e. from $\Theta = 0$ to $\Theta = 2\pi n$ where n is an integer number of round trips).

If we now factor dephasing into our model, then the system will transition from a pure state to a mixed state at a rate e^{t/T_2^*}. This transition will take us to a state where all knowledge of our initial system has disappeared and when a measurement is performed we will be equally likely to measure our state as being in the ground or excited state ($|\alpha|^2 = |\beta|^2$), illustrated by the decay in Figure 2.6a.

Hahn Spin-Echo Measurement

The Hahn spin-echo sequence [103] is designed to reverse the effects of dephasing, removing the T_2 contribution from the T_2^* time. The sequence works to re-phase the dephasing by periodically inverting the spins on the Bloch sphere (a π rotation about the $\hat{x}$ axis in the Bloch sphere illustration, Figure 2.3), effectively reversing the magnetisation axis (our $\hat{z}$ axis). In experiments we quote the measured values still as T_2^*, as we cannot be completely certain that we have fully removed T_2 (recall this relationship from Equation 2.39). The sequence is conducted as follows.

Again, an initial pulse of some field is used to initialise the system into the ground state. From here, a pulse from our driving field of duration $\pi/2$ (the duration of a π-pulse already having been determined from our measurement of the Rabi frequency) is used to rotate the spin about the $\hat{x}$ axis of the Bloch sphere — moving it on to the equator. If the state 'sits' on the equator, for some time t, if starts dephasing. This can be thought of as the initially single arrow of the Bloch vector spreading into a wedge that still lies in this plane. The wedge represents the uncertainty regions where the state lies. At a time $2t$ a π-pulse is created that

---

[vi]With no change to the power of the driving field, as the Rabi frequency is also proportional to the square root of the power.

inverts the sphere around the $\hat{x}$ axis. Because we have now reversed the magnetisation axis the state continues to dephase but in opposite direction, effectively rephasing the state and refocusing the Bloch vector. A subsequent $\pi/2$-pulse is created and projects the state into $|\uparrow\rangle$ prior to a readout measurement being conducted.

For each consecutive measurement cycle we increase the time between each of the driving field pulses, $t = t + \Delta t$. The dephasing effects continue to be removed by the sequence, and allow us to gain information about the underlying decoherence rate T_2'.

2.1.10   Application to the NV Centre

In the NV centre, initialisation, manipulation, and readout of the spin state can be achieved by implementing combinations of laser pulses (at 532 nm), microwave pulses (at ~2.88 GHz), and fluorescence (photon counts) measurements, respectively [19, 20]. For NV spins in diamond residual Nitrogen atoms are the largest source of dephasing [19, 104], and for diamond material in which the Nitrogen concentration is very low (5×10^{-2} ppb), the main source of decoherence becomes the nuclear spin bath constituted by ^{13}C atoms. In these samples, T_2 can be as long as 2 ms [2, 105, 106]. These T_2^* times are orders of magnitude greater than the π-pulse durations required for manipulation of the NV spin (which are of course dependent on both the power of the driving field and its detuning from the transition frequency). For comparison, T_2^* times in semiconductor quantum dots are $\sim 1\,\mu$s [107], and in single molecules 1–10 ns [108, 109].

2.2   Experiment Overview

We draw upon the experimental setup outlined in § 2.2.1, with our microwave cavity suspended above the surface of a ND sample. The sample itself was selected such that few NDs contained colour centre defects, and those that did were likely to contain only a single NV centre, § 2.2.3.

To first establish our experimental methods we run the experiment initially without the microwave cavity, but rather using a stripline antenna placed in close proximity (on the order of 10μm) to a ND hosting a single NV centre. This served as our control experiment as the strip antenna is a well-established method (§ 2.2.1). The stripline antenna results in significant heating and undesirable sample drift, which is the primary motivation for developing a dielectric-loaded resonator (DLR) cavity for use with NV centres. Further details about this cavity can be found in § 2.2.2. The DLR cavity allows contactless application of microwave fields to NV centres without direct heating of the sample.

We then changed samples (required as the cavity cannot be above the micro-wire sample) and implement the microwave DLR cavity into the setup[vii]. A new, single-centre ND was identified and a ODMR signal recorded. We present the results of this experiment side-by-side with our stripline antenna measurements for comparison.

[vii]NDs on a gridded coverslip which could be shared by both microwave delivery experiments would provide a more ideal method in order to further remove material properties from the investigation, however, this was unfortunately overlooked.

2.2.1 Experiment Architecture

A lab-built confocal microscope was utilised to conduct these measurements. For optical excitation we employ a $\lambda = 532$ nm CW laser (Compass 315M-100; Coherent), which is focused onto the sample via a 100× oil immersion objective (UplanFL N, NA 1.3; Olympus) to maximise collection efficiency. The excitation beam passes through an acousto-optic modulator (AOM) (OD-8813A; NEC) to control its switching when implementing pulse sequences. To separate the excitation and collection paths we use a 550 nm long pass filter (FEL0550; Thorlabs) to suppress the excitation laser. For photon counting we use a pair of avalanche photodiodes (APDs) (SPCM-AQR-14; Perkin Elmer) arranged in a Hanbury-Brown and Twiss (HBT) interferometer configuration [110]. This allowed us to either use a single APD when operating the confocal, or to use both APDs when conducting autocorrelation measurements [111]. The collected light could also be directed by fibre to a spectrometer (SpectraPro Monochromator Acton SP2500, dispersion 6.5 nm/mm at 435.8 nm; Princeton Instruments) for spectroscopy measurements.

To deliver the microwave field, we either use a lab-build stripline antenna constructed from copper wire of diameter $\sim 20\,\mu$m (Figure 2.8a), or use the DLR microwave cavity suspended above the sample (Figure 2.8b). For microwave generation we use a laboratory microwave source (SMIQ06B; Rohde & Schwarz) and amplify its signal (ZHL-16W-43-S+; MiniCircuits). We pass the microwaves through a switch (ZASWA-2-50DR+; MiniCircuits), controlled by a fast TTL pulse generator (PulseBlaster; SpinCore), which also controls the lasers AOM switch, therefore providing full pulse sequence control. A diagrammatic representation of the measurement architecture is provided in Figure 2.7.

2.2.2 DLR Cavity

Traditionally, telecommunication (GSM, UMTS, etc), radar (military and civilian), and more recently navigation (GNSS, GPS, etc) systems have been based on microwave cavities – first empty, then loaded with dielectric materials. Driven by the requirements of the telecommunications industry, new materials and strategies have been developed to reduce microwave losses, leading to the creation of cost-effective and high-performance devices [112]. Microwave cavities are of extreme interest for the characterization of materials [112–114], in bulk semiconductor materials [115, 116], and even adjusted for ferroelectric thin and very thin films [117, 118]. Recently, experiments on paramagnetic impurities in single crystals at the ppm and even ppb level have been possible using whispering gallery mode cavities [119, 120].

Our DLR cavity, developed externally, is an open cylindrically symmetric cavity design with a pure transverse electric (TE) mode with two non-vanishing magnetic-field components, H_r and H_z. A dielectric rod constructed from high-permittivity, low-loss microwave material, in our case titanium dioxide (TiO_2) rutile, is inserted into the cavity (itself made of copper), annotated in Figure 2.9. This confines the field to an area roughly 10×10 mm^2. The fundamental mode of the cavity is 2.2 GHz as a result of the TiO_2 material used. For NV spin manipulation we use the higher-order $TE_{0,1,3}$ mode which resonates at 2.7 GHz. The frequency of the cavity can be fine tuned by the mechanical insertion of a metallic plunger into the core of the cavity cylinder. This directly affects the electric field and can shift the resonance frequency up to a value 3.1 GHz. The Q-factor of the $TE_{0,1,3}$ cavity mode is ~ 1000, however, the cavity coupling coefficient (the percentage of input power converted into the
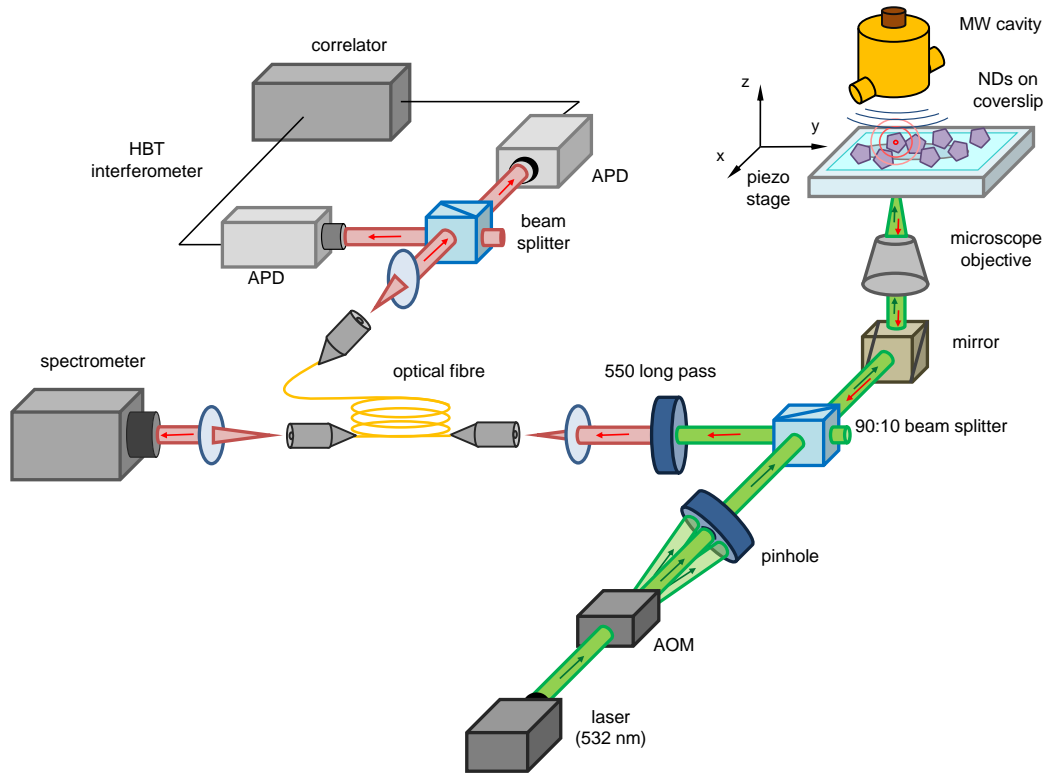
Figure 2.7: Experiment architecture employed for our NV spin measurements. Our experimental setup for this investigation, consists of a lab-built confocal microscope and peripheral instruments. A $\lambda = 532$ nm CW laser is used as our excitation source and directed through an acousto-optic modulator (AOM), itself controlled via a fast TTL pulse generator. Light in the optical collection path is passed through a 550 nm long pass filter, then can be directed via a fibre to either a set of APDs in a HBT configuration or to a spectrometer. Either a stripline antenna or our microwave cavity, as per Figure 2.8, is mounted with the nanodiamond sample (the case of the microwave cavity is shown above). Our microwave source first passes through a switch, controlled by the same fast TTL pulse generator, and then is boosted by an amplifier.
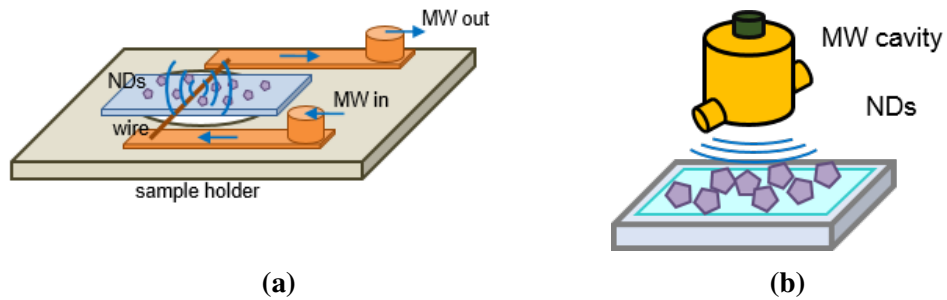
Figure 2.8: Schematic representation of the configuration of each sample. a) The stripline antenna constructed with copper wire of diameter $\sim 20\,\mu$m. To achieve adequate intensity the antenna must be placed within $\sim 10\,\mu$m of the target ND. **b)** The dielectric-loaded resonator (DLR) cavity is suspended ~ 1 cm above the ND sample.
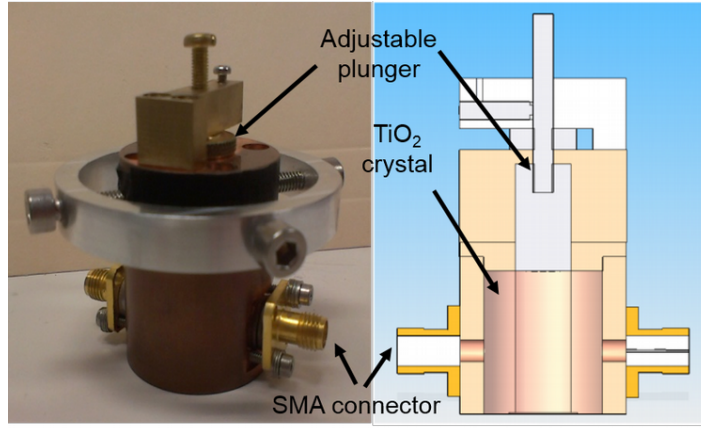
Figure 2.9: The dielectric loaded resonator (DLR) microwave cavity. The physical dimensions of the cavity are 32 mm along the $\hat{z}$-axis and 20 mm in diameter. TiO_2 rutile is placed inside a coper cavity, and a metallic plunger can be inserted to tune the cavity mode.

cavity mode) is small at a value of $\sim 1\%$.

2.2.3 Materials Characterisation

Samples (Microdiamant type Ib HPHT powder, N concentration >20 ppm, nominal average size ~100 nm) were prepared by placing a droplet of ND-containing water (Milli-Q) solution (0.1% w/v concentration) onto a standard microscope coverslip (BB022022A1; Menzel-Glaser) and allowing the water to evaporate. Once dried, samples were placed in a furnace (CMF-1100; MTI Corporation) for 15 minutes at 550 °C to remove surface graphite and other contaminants.

In the case of the cavity sample, this is the extent of the sample preparation (Figure 2.8b). For the micro-wire sample, the coverslip was then attached to a mounting bracket and a copper wire of diameter $\sim 20\,\mu m$ placed on the surface of the sample in close proximity to the scanned area, see Figure 2.8a.

Confocal Microscopy

Our confocal microscopy setup (§ 2.2.1) was used to optically characterise both samples. Regions ($40\mu m \times 40\mu m$) were selected with an appropriate density of NDs (Figure 2.10) and, in the case of the stripline sample, the region was located sufficiently close (1–10 μm) to the micro-wire antenna.

Identification of Single-Centre NDs

Our aim was to manipulate single spin qubits. Hence, NDs containing only a single NV centre were identified for the measurement. This was achieved by aligning the confocal to the target ND and recording the second-order autocorrelation function (Equation 2.54) via the use of two single-photon detectors in a Hanbury-Brown and Twiss (HBT) interferometer configuration (described in § 2.2.1):

$$g^{(2)}(\tau) = \frac{\langle I(t)I(t+\tau)\rangle}{\langle I(t)\rangle\langle I(t+\tau)\rangle} \tag{2.54}$$
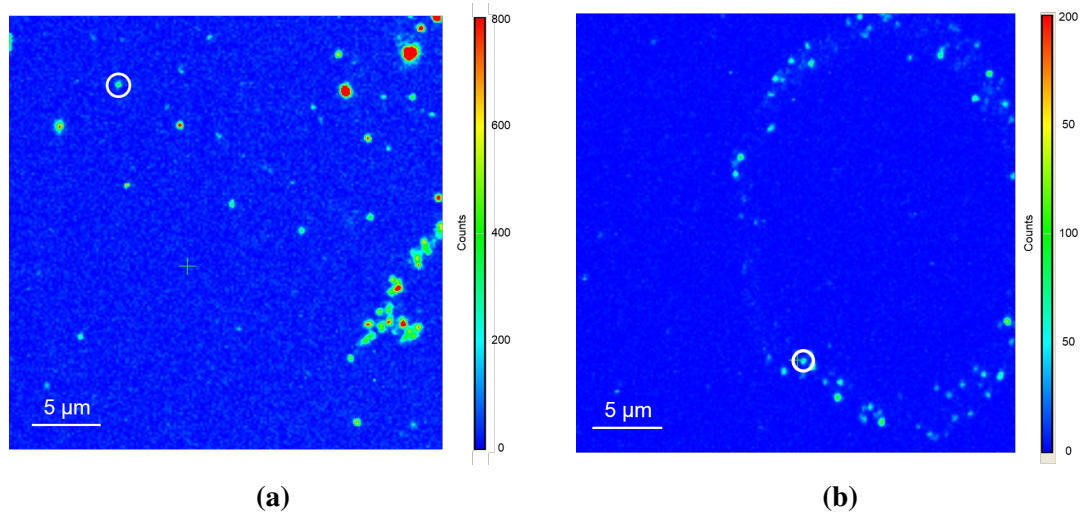
Figure 2.10: Confocal microscopy. Intensity colour-maps spanning a 40μm $\times$ 40μm region, with each respective target ND circled. **a)** The stripline antenna sample. **b)** The cavity sample.
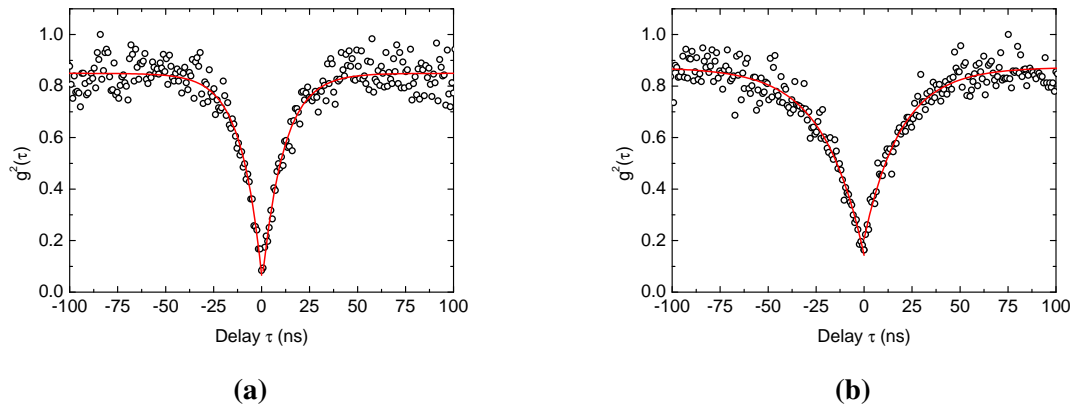
Figure 2.11: Autocorrelation measurements. Second-order autocorrelation function, $g^{(2)}(\tau)$, measurements displaying antibunching. The presence of this behaviour indicates that both systems contain only a single emitter — in our case a single NV defect in the ND. **a)** The stripline antenna sample, and **b)** the cavity sample.

where I is the luminescence signal intensity, and $g^{(2)}(0)$ is the second-order correlation function. The value $g^{(2)}(\tau)$ is proportional to the conditional probability of detecting a second photon at time $t = \tau$ given that we detected one at $t = 0$. An antibunching dip at $g^{(2)}(0)$ indicates a single quantum emitter[viii] — as the probability that two photons are emitted simultaneously approaches zero. This is indeed what we observe in both cases. An antibunching dip at $g^{(2)}(\tau = 0)$, greater than $\sim$80%, indicating that both selected NDs contain a single NV centre (a contrast of $\sim$50% is usually attributed to a single quantum emitter), Figure 2.11.

Spectral Data

The photoluminescence spectrum was recorded to ensure the fluorescent spot had been correctly identified as a NV centre. Under excitation with a 532 nm laser we observe the characteristic NV spectrum, Figure 2.12.

[viii]The contrast of the $g^{(2)}$ function scales as $1/n$, where n is the number of emitters [84, 121].

(a)   **(b)**
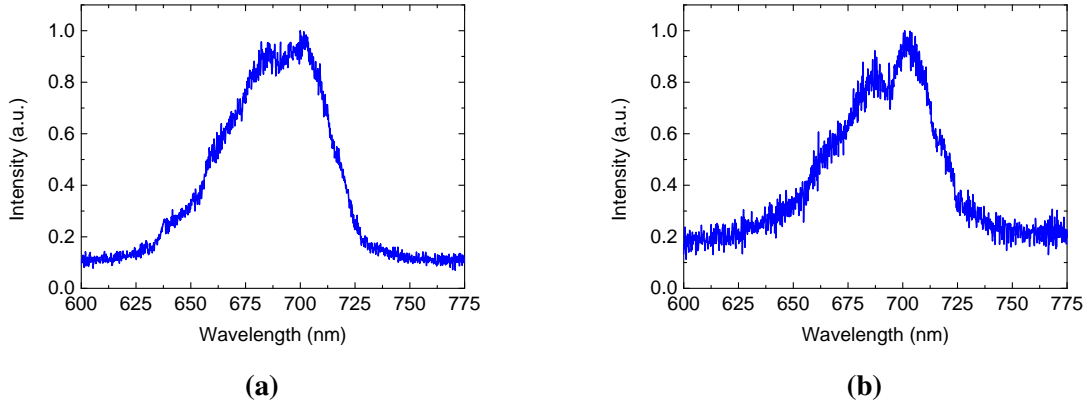
Figure 2.12: Photoluminescence spectrum under 532 nm excitation. A λ = 532 nm laser is employed to excite both ND samples respectively. Note that the spectra in the figure are recorded from ND material, which can give rise to 'unusual' spectral features due to several factors, including stress, strain, and surface chemistry. **a)** The stripline antenna sample ND spectrum, and **b)** the cavity sample ND spectrum.

2.3   Interactions with the Microwave Field

To ensure adequate interaction between the generated microwave field and the selected NDs we conducted continuous-wave optically detected magnetic resonance (ODMR) measurements. The contrast of the measurement is dependent on both the strength and direction of the magnetic field — for maximum contrast the field should be aligned to the orientation of the NV axis, Figure 2.1b. In the case of the cavity sample the intensity of the field is also dependent on the mode of the microwave cavity.

The $TE_{0,1,3}$ mode of the microwave cavity was tuned to the position of the ODMR peak at 2.875 GHz, seen in Figure 2.13. The FWHM of the cavity mode is 3.5 MHz and the cavity has a Q-factor of 1000.

We ran an ODMR measurement on both the micro-wire and cavity samples (Figure 2.14). In the case of the stripline antenna we observed a zero-field splitting of the $m_s = \pm 1$ microwave transition, with ODMR contrast of 13% for the most prominent peak. In the case of the cavity a contrast of 8% was measured, with no apparent zero-field splitting (evident in ~15% of NVs [51]). We note that the ODMR contrast using the microwave cavity is within 3% of the 11% maximum contrast recorded previously with this cavity [99].

2.4   Rabi Cycles

We commence our NV spin manipulation endeavours with the generation of Rabi oscillations in each respective sample. We achieved this in both cases, however, we find disparity in the Rabi frequency, Ω_R, of the two NV centres, with the oscillations being slower in the case of the cavity implementation. The poor 1% coupling efficiency of power into the microwave cavity mode makes it impossible for us to deliver a comparable amount of power into the field by this method. This results in a lower Rabi frequency for this sample, as the Rabi frequency is dependent on the power of the driving field.
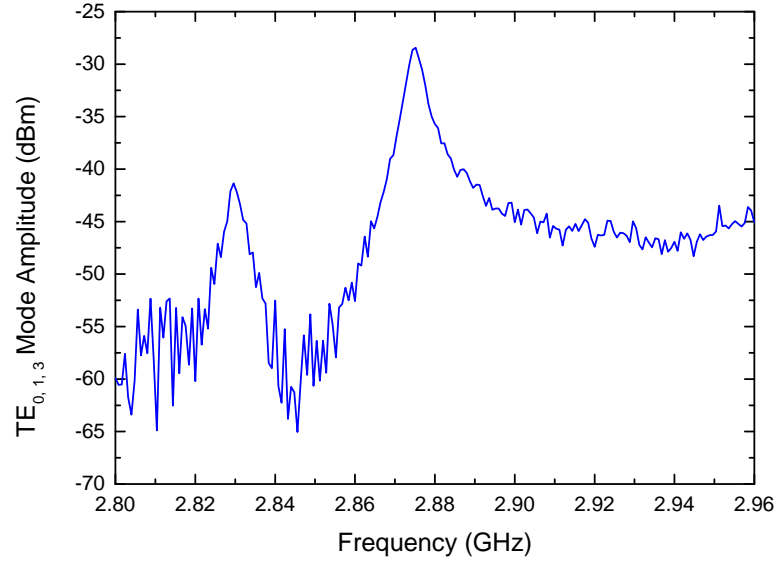
Figure 2.13: Cavity transmission spectrum. The microwave cavity is tuned to match the 2.875 GHz ODMR dip of the targeted ND, Figure 2.14b. The measured FWHM of 3.5 MHz corresponds to a Q-factor of 1000. The spectrum has been recorded via the use of a vector network analyser (VNA) (FieldFox N9918A; Agilent Technologies).
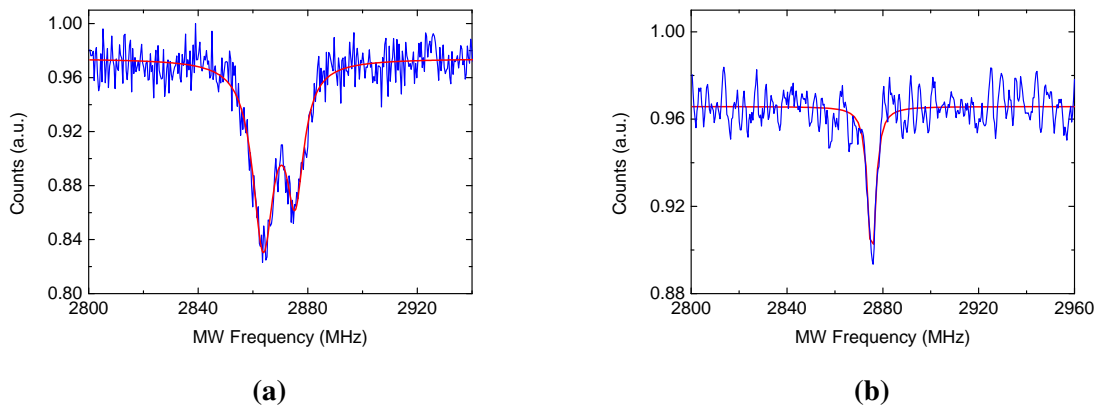
Figure 2.14: Optically detected magnetic resonance. Peaks in the observed data are fitted with Lorentzians, shown in red. **a)** The stripline antenna sample; zero-field splitting peaks at 2.865 GHz and 2.875 GHz, contrast of the deepest peak (2.865 GHz) is 13%. **b)** The cavity sample; single peak at 2.875 GHz with a contrast of 8%. Note that the ODMR signal is a convolution of both the NV response and the transmission of the cavity, which acts as a filter.
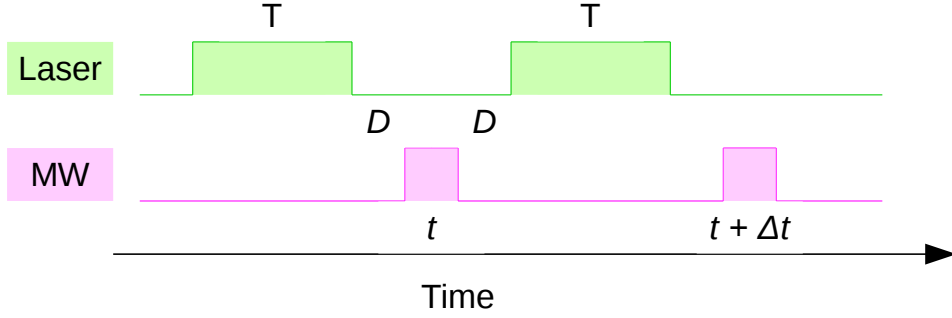
Figure 2.15: Rabi pulse sequence. Pulse sequence used both in the case of the micro-wire and the cavity as discussed in § 2.4.1. The laser pulse is on for 3000 ns, and the delay, D, is set to 600 ns. In the case of the micro-wire, $t = 50$ ns and $\Delta t = 25$ ns. In the case of the cavity, $t = 50$ ns and $\Delta t = 100$ ns.

2.4.1   Measurement

The specific pulse sequence employed is shown in Figure 2.15. A laser pulse duration of 3000 ns was chosen, and an initial microwave pulse duration of $t = 50$ ns, expanded in duration by $\Delta t = 25$ ns each pulse for 50 increments, such that they periodically sweep through multiples of π, Figure 2.15. The microwave source output was selected to be at the frequency of the ODMR dip to transfer spin into the $m_s = \pm 1$ state, 2.865 GHz for the stripline antenna sample (the prevalent ODMR peak) and 2.875 GHz for the cavity sample, as per Figure 2.14. We use the same laser pulse for readout and re-initialisation of the system — the closer we are to the excited $|\uparrow\rangle$ state the greater decrease we observe in the fluorescence, then after a few optical cycles of the NV the system is reinitialised back into the ground $|\downarrow\rangle$ state.

2.4.2   Results

This sequence resulted in a periodic fluorescence signal as a function of microwave pulse duration, Figure 2.16. A damped-sinusoidal function (which is appropriate [20, 91]) was fitted to the extracted data.

$$y = y_0 + A e^{-\frac{x}{t_0}} sin\left(2\pi \frac{t - t_c}{T}\right) \tag{2.55}$$

where $\Omega_R = 1/T$, π-pulse $= T$, and $T_2^* = t_0$. In the case of the stripline antenna we measured $\Omega_R = 4.8$ MHz, and $\pi = 104$ ns. And, in the case of the microwave cavity sample, we found $\Omega_R = 0.83$ MHz, and $\pi = 612$ ns. To more accurately determine T_2^* Hahn spin-echo measurements will be conducted, § 2.5.

2.4.3   Power Ramping

To further manipulate the behaviour of the NV spin, in the case of the stripline antenna sample we briefly investigated the dependence of the Rabi frequency, Ω_R, on the microwave power, P_{MW}. By ramping the microwave power we were able to confirm the square-root relationship between these parameters, $\Omega_R \propto \sqrt{P_{MW}}$. This data is presented Figure 2.17 where the expected trend can be clearly observed. A similar experiment was not possible on the cavity sample due to the low power throughput of the microwave cavity.
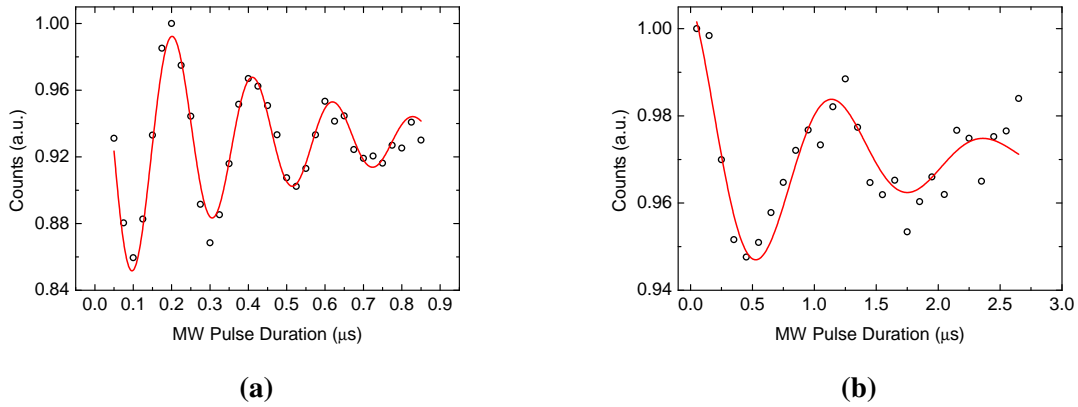
Figure 2.16: Rabi oscillations. A damped-sinusoidal function is fitted and displayed in red. From this the Rabi frequency, Ω_R, duration of a π pulse and T_2^* can be extracted. **a)** The stripline antenna sample; $\Omega_R = 4.8\,\text{MHz}$, and $\pi = 104\,\text{ns}$. **b)** The cavity sample; $\Omega_R = 0.83\,\text{MHz}$, $\pi = 612\,\text{ns}$.

2.5 Spin-Echo Measurements

We implement a Hahn spin-echo pulse sequence to measure the decoherence of the NV spin without the dephasing influence from surrounding lattice and impurities (i.e. nitrogen and carbon-13). We were able to achieve this result in the case of the stripline antenna sample, however as we will see, we were unable to achieve this in the case of the microwave cavity sample due to the properties of the DLR cavity.

2.5.1 Measurement

As in the case of Rabi oscillations, we again use optical initialisation and readout combined with microwave pulses to manipulate the spin of the NV. We use a Hahn spin-echo sequence to remove any influence of dephasing from the surrounding lattice, measuring the decoherence of the NV spin. The theory of this measurement was presented in § 2.1.9, and a representation of the sequence is shown in Figure 2.18. We use measurement specific values of the π-pulse durations from the Rabi cycle measurements, and use $t = 50\,\text{ns}$, and $\Delta t = 10\,\text{ns}$ for the stripline antenna sample and $\Delta t = 100\,\text{ns}$ for the cavity sample.

2.5.2 Results

This Hahn spin-echo sequence produces data of the echo signal decaying over time. In the case of the stripline antenna sample we observe the expected exponential decay of the signal, Figure 2.19a. From our negative exponential fit to the data we extract a T_2^* value of $3.7\,\mu\text{s}$. However, in the case of the cavity sample we struggle to observe such a trend, Figure 2.19b. At short time scales, $t + \Delta t \leq\sim 1\,\mu\text{s}$, the clarity of the signal is poor — indicating poor spin coherence at these time scales. We speculate that the high Q-factor of the DLR cavity alters the shape of the microwave pulses and is particularly critical at short time scales. We neglect data points where this affect is present from the fit, and extract $T_2^* = \sim 2.8\,\mu\text{s}$.
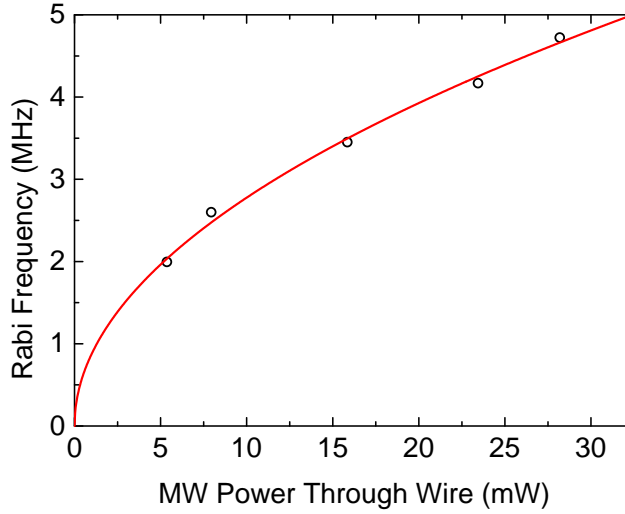
Figure 2.17: Microwave power ramping measurement. To confirm the relationship $\Omega_R \propto \sqrt{P_{MW}}$, we briefly investigated the dependence of the Rabi frequency, Ω_R, on the microwave power, P_{MW}. This measurement was only possible on the stripline antenna sample, with the insufficient power throughput of the microwave cavity preventing a similar measurement on that sample.

2.6   Outlook

We have used the DLR cavity as a new tool for generating microwave fields for single NV spin manipulation. The design of the cavity of this specific application has some shortfalls, namely its 1% coupling efficiency of power into the microwave cavity mode, and, the cavity's inability to support pulse widths below $\sim 1\,\mu$s. As a result, we have been unable to demonstrate coherent control of the NV spin. The DLR cavity has been used to generate NV spin Rabi oscillations, with the cavity suspended ~ 1 cm above the sample surface. This method is non-invasive, allows uniform spin-addressing over large distances (mm to cm), enabling stable long-term, no-destructive observations that could find strong application in biologic environments.
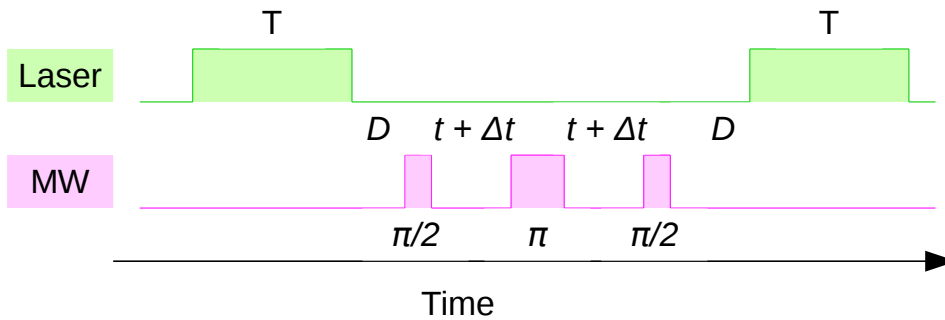
Figure 2.18: Hahn spin-echo pulse sequence. The pulse sequence used both in the case of the micro-wire and the cavity as discussed in § 2.5.1. In the case of the micro-wire; $D = 500$ ns, $t = 50$ ns, $\Delta t = 10$ ns and $\pi = 104$ ns. And, in the case of the cavity; $D = 600$ ns, $t = 50$ ns, $\Delta t = 100$ ns and $\pi = 612$ ns.
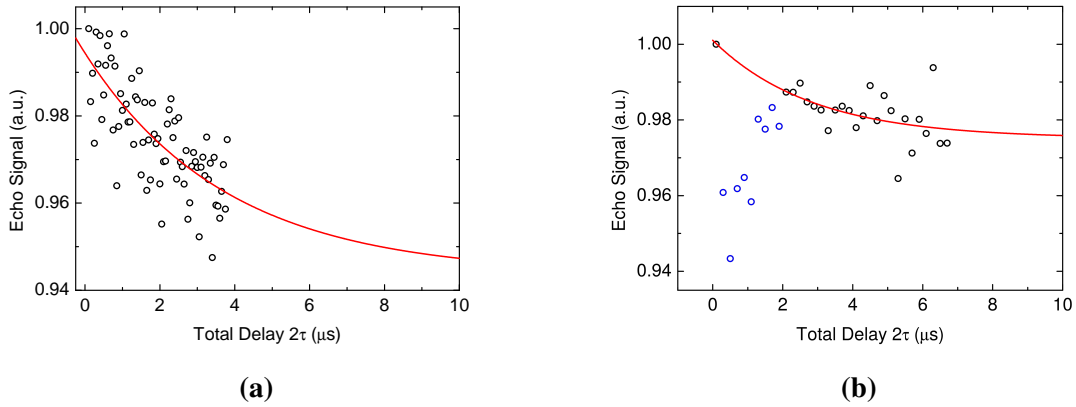
Figure 2.19: Spin-echo measurements. a) The stripline antenna sample; with a negative exponential fitted and extrapolated to show the tail of the T_2^* decay curve (recall discussions in § 2.1.8 and § 2.1.9 regarding T_2^*, T_2, and T_2'). The extracted coherence time is $T_2^* = 3.7\,\mu s$. **b)** The cavity sample; with a negative exponential fitted and projected. Only the black data points have been included in the fit — blue data points are in the temporal region where the ringing of the cavity does not allow the cavity to function appropriately at short time scales, discussed in § 2.5.2. The extracted coherence time in this case is $T_2^* = \sim 2.8\,\mu s$.

For future application of this technology we recommend four key features for a second-generation DLR cavity to address NV spins. First and foremost, the coupling efficiency into the cavity mode should be increased from the current 1% value. This could be achieved by decreasing the Q-factor of the cavity. This decrease would also enable shorter pulse widths to be created, which may enable coherent NV spin control.

To increase ease of alignment above the sample, it would be desirable for the next iteration of the design to include axial optical access. This would enable a system such as a suspended camera to be used to gain awareness of the alignment of the cavity with respect to the objective of the confocal system. The more reliably the cavity can be placed in an effective position, the more microwave power is incident on the target NDs, and the greater the ODMR contrast value.

Finally, a second generation cavity should have mechanical control of the plunger — used itself to tune the cavity mode. The current mechanism requires dismounting the cavity from above the sample for tuning, and is static thereafter. Making this a dynamic variable that could be computer controlled, and hence algorithmically adjustable, the cavity mode could be optimised for each specific ND, and active feedback could be implemented to periodically maintain this optimisation. Alternatively, a resonant circuit e.g. capacitor/inductor could be used.

To better understand interactions between NV centres in the pursuit of diamond-based quantum technologies it is also important to investigate mechanisms for the control of many-NV systems. We now continue and explore the dynamics of superradiant emission and cooperative behaviour originating from individual NDs containing high-densities of NV centres.

3

NV Superradiance in Nanodiamond

"I leave Sisyphus at the foot of the mountain. One always finds one's burden again. But Sisyphus teaches the higher fidelity that negates the gods and raises rocks. He too concludes that all is well. This universe henceforth without a master seems to him neither sterile nor futile. Each atom of that stone, each mineral flake of that night-filled mountain, in itself, forms a world. The struggle itself toward the heights is enough to fill a man's heart. One must imagine Sisyphus happy."

Albert Camus

The feasibility of many nanodiamond-based applications heavily relies on the spin and optical properties of the NV centre. Here we investigate the optical properties of diamond nanoparticles containing a high density of NV centres. Specifically, we report the observation of room-temperature superradiance for single nanodiamonds containing many NV centres ($\sim 10^3$ in a ~ 100 nm nanoparticle). Superradiance is a collective quantum effect that occurs when several identical emitters are highly confined in space ($V \ll \lambda^3$) and build up coherence amongst each other. This leads to a significant speed-up in the photon emission rate and to specific quantum correlations that are distinct from a collection of independent emitters, which we observe experimentally in our nanodiamond-NV centres.

Our observation of cooperative effects in nanodiamond NV centres [122] is the first for a solid-state, room-temperature system analogous to what was originally proposed by Dicke in his pioneering paper in 1954[i] [123]. The project origins lie in an experiment conducted by the research group where a new approach was implemented to control nanodiamond material in an optical tweezer setup, discussed immediately below. Alongside our superradiance results, we also discuss how our findings are relevant, ultimately, for developing diamond-based quantum engineered superradiant systems at room-temperature — which might lead to applications including efficient photon detection, energy harvesting and quantum sensing.

3.1   Background

In 1970 Ashkin[ii] demonstrated that particles approximately 1 μm in size could be trapped in the focused beam of a laser [124]. This demonstration stemmed the creation of two separate and distinct fields of research; optical tweezing and atomic trapping [125].

With optical tweezers, dielectric nanoparticles in a liquid environment are trapped both transversely and longitudinally. Optical tweezers rely on the bulk polarisability of the particle, with the trapping force itself depending on the contrast in the refractive index between the trapped particle and the surrounding medium. Below a certain size threshold, the ability to trap a particle becomes more and more difficult. In the case of nanodiamond material, and with the use of conventional far-field optics, this size limit threshold occurs at around 100 nm [7] — below which this technique cannot be applied successfully. Conversely, atomic dipole trapping is enabled by the near-resonant polarisability of single atoms [126]. This ability to manipulate neutral atoms has enabled quantum technologies such as atomic clocks [127], optical lattices [128], and quantum simulations [129].

Previous investigations in our lab have demonstrated a new approach involving the combination of the two trapping mechanisms described above [26]. Nanodiamonds containing a high density of NV centres (although this applies to the trapping of any dielectric nanoparticles containing high densities of any atom-like impurities), while held in a conventional optical tweezers trap, were exposed to a near-resonant laser beam slightly detuned from the NV zero-phonon line (ZPL) transition. The near-resonant atomic dipole forces act on the system to either increase or decrease the trap stiffness, which is a measure of how tightly the particle is held in the trap. The effect is dispersive — red-detuned light increasing the trap stiffness and blue-detuned light decreasing the trap stiffness, by approximately 10% compared to the case where only bulk polarisability effects are considered [26]. Despite being quantitatively modest the effect is remarkable. The observable trapping effect is generated by a number of emitters $\sim 10^4$ times smaller than the number of carbon atoms of the host nanodiamond, and could potentially allow for the manipulation of nanoparticles on the scale of just a few tens of nanometres.

Interestingly the fit to the data revealed that the measured trap stiffness was 40 times[iii] greater than the theoretical prediction [26]. Moreover, when the fit was conducted leaving the number of NV centres in the nanodiamond unconstrained, and the NV centres were assumed to act independently rather than collectively, the best possible fit was achieved for 410,000 NV centres — significantly greater than the estimated 9,500 NVs hosted in the nanodiamond. To understand the behaviour of the nanodiamonds in the trap, cooperative effects [123] were included in the theoretical model resulting in a more accurate description of the system. Three separate models were fitted to the trapping data;

- **No limit to the number of NV centres.** The fits produced by imposing no limits on the number of NV centres in the ND estimate either 410,000 NV centres acting

---

[i]"For want of a better term, a gas which is radiating strongly because of coherence will be called 'superradiant'." — Robert H. Dicke

[ii]Nobel Prize in Physics 2018 "for the optical tweezers and their application to biological systems."

[iii]We expect a 0.25% increase in trap stiffness if all NV centres act independently. The observed effect (10%) is 40 times greater than this value.

independently (a number much greater than permitted from the nitrogen doping of the sample), or 1,600 NV centres acting cooperatively (distributed over 5 cooperative domains).

- **Assume the maximum number of NV centres.** In this case the parameter for the average number of NV centres in the ND volume was locked at 95,000 — the assumption that every nitrogen implanted from the doping process (300 ppm) was converted to an NV centre via annealing[iv]. Again, the fits indicated the same result of the cooperatively enhanced trapping force being generated by 1,600 NV centres spread over 5 cooperative domains.

- **Fix the number of NV centres to the estimated value.** This case sets the average number of NVs per ND volume to 9,500 — the value to be expected from the nitrogen doping and annealing process used in preparation of the specific ND sample. The best fits are produced in this parameter space, indicating the 9,500 NV centres acting cooperatively, distributed over 85 − 100 domains.

Whilst the trapping experiment supported the possibility of cooperative effects being present among NV centres in diamond nanoparticles[v], direct evidence was still missing as were many of the details including characteristics, number and size of the cooperative domains. Conveniently, cooperative effects are at the crux of superradiance, whose occurrence can be tested via specifically designed experiments including, for instance, direct lifetime measurements.

3.1.1 Superradiance

Predicted in 1954 by Dicke [123], superradiance is the rapid release of energy in an intense radiation burst, arising from collective quantum effects between the emitters. According to Dicke's model, superradiance takes place when identical, indistinguishable emitters are confined in a space much smaller than the wavelength of the interacting radiation field — which makes atom-like emitters in a nanoparticle a suitable candidate. However, superradiance from atom-like emitters in a nanoparticle had never been observed experimentally, for the indistinguishability of emitters in a solid-state system is usually compromised due to local inhomogeneities. Specifically, to exhibit cooperative behaviour the NVs-nanodiamond system must abide by two fundamental rules:

- **Spectral Indistinguishability.** The ZPL energy of each individual NV centre in the NV ensemble must be indistinguishable — in frequency space the ZPL of each NV centre must be within the ZPL FWHM of any other cooperating NV centres. This is represented in Figure 3.1, showing that the inhomogeneous broadening (different for each emitter) must be less than the homogeneous broadening (for the ensemble of emitters).

- **Spatial Indistinguishability.** Similar to the condition of spectral indistinguishability, it must be impossible to determine from which emitter a given photon originated in the spatial domain. That is, the emitters contributing to the cooperative effects must be confined to a volume less than the cube of the wavelength ($V \ll \lambda^3$).

[iv]A 100% conversion from N to NV, nor a 300 ppm NV concentration, if not technically feasible. These parameters are included to highlight that superradiance effects must be in play.

[v]The enhanced dipole moment associated with superradiance can lead to enhanced trapping stiffness.

Superradiant behaviour has been observed in a number of systems [130–143], a subset of which are presented below. The first experimental observation of superradiance occurred in 1973 in a system of hydrogen fluoride gas [137]. In this experiment hydrogen fluoride gas at low-pressure was confined to cylindrical sample cells (length 30–100 cm) and a laser pulse ($\lambda \sim 2.5\,\mu$m) was used to excite the system. A superradiant pulse, delayed by a time-scale on the order of microseconds, was then recorded as being generated from the sample. The experimental results could be completely explained through the description of the system in terms of Dicke states, see § 3.3.

Another system shown to exhibit superradiant behaviour is that of two trapped ions [134]. The experiment, conducted in 1995, used two laser-cooled trapped ions and measured the degree of superradiance in the emission directly as a function of the ion separation distance (a variation in the degree of spatial distinguishability, § 3.1.1).

The first experiment to investigate and observe superradiance in a solid-state system was conducted in 2007 [135]. Here quantum dots were grown with a high density on a gallium arsenide (GaAs) substrate. The quantum dots were of size 6–10 nm, and separated by a spacing of ~35 nm — much smaller than the 363 nm wavelength of the excitation laser. The authors recorded the lifetime of the ensemble of quantum dots and observed superradiant behaviour — manifested by the shortening of the quantum dots lifetime. Then, the substrate was etched to create separated 'mesa' structures (flat-topped islands) to effectively reduce the number of emitters able to contribute to superradiant behaviour. The lifetime of the samples became longer — returning to what would be expected from a system of independent emitters.

Superradiance was also observed in 2014 in superconducting qubits weakly coupled to a fast-decaying microwave cavity [132]. Again, the lifetime of the system, in combination with reconstruction of the density matrix of the emitted field, was used as a key indicator of superradiant behaviour.

Since demonstrating the experimental occurrence of superradiance from ensembles of NV centres in nanodiamond in our laboratory, described hereafter, two additional papers reporting superradiance in diamond systems have been published. The first was the report of superradiant emission from two silicon-vacancy (SiV) colour centres coupled via a diamond photonic crystal cavity [142]. The second was the demonstration of superradiance from NV centres coupled to a microwave resonator in the fast cavity limit [143].

3.2   Experiment: Ultra-Fast Radiative Lifetimes

One of the signature indicators of superradiant behaviour is a shortening of the emitters lifetime. When a system of N emitters act cooperatively, they radiate spontaneously at a rate that grows non-linearly with their number and can be as high as N^2 in the middle of the Dicke ladder (see § 3.3) — faster than that of N independent emitters [144]. We thus designed an experiment aimed at measuring the lifetimes of 100 individual NDs, drawn from the sample used in the previous trapping experiment [26] (see § 3.2.2).

3.2.1   Experiment Architecture

The experimental setup is described in brief below, with a schematic representation provided in Figure 3.4. A lab-built confocal microscope served as the platform for this experiment,
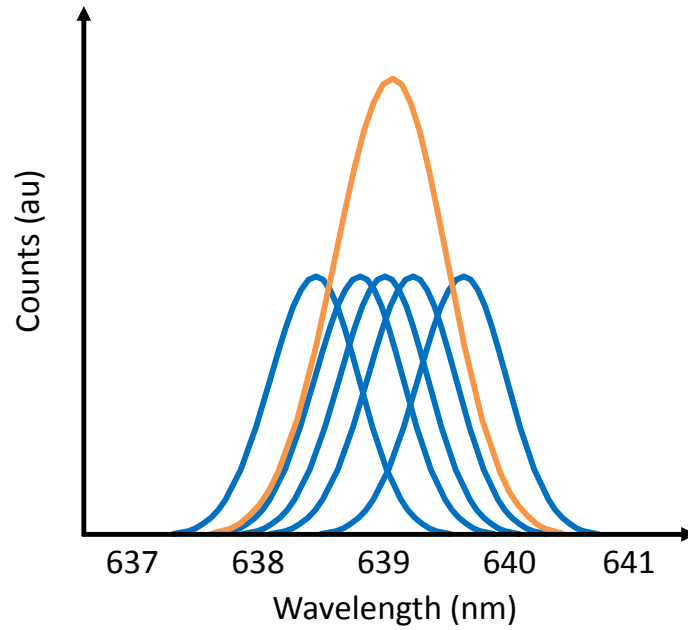
Figure 3.1: Homogeneous and inhomogeneous ZPL broadening. In this representation the ZPLs of individual NV centres (blue peaks) fall predominantly within the FWHM of their neighbours. This demonstrates the case where the inhomogeneous broadening is less than the homogeneous broadening (orange peak), fulfilling the condition of spectral indistinguishability.

utilising an 100× oil immersion objective (UplanFL N, NA 1.3; Olympus) to maximise the collection efficiency. A commercial atomic force microscope (AFM) system (Ntegra AFM; NT-MDT) was integrated with the confocal to directly measure the size of each individual ND.

A λ = 532 nm pulsed laser was used as the excitation source for the experiment (LDH-P-FA-530; PicoQuant), operating at either 5 MHz or 20 MHz. A short investigation was conducted to ensure the produced pulses were consistent and well shaped. This was undertaken by looking for correlations between the electronic laser trigger pulse and the laser photons arriving at an avalanche photodiode (APD). We observed that above a particular power threshold the shape of the laser pulses deteriorated, Figure 3.2. As such, care was taken to ensure all measurements were conducted below this threshold.

For photon detection two APDs (SPCM-AQR-14; Perkin Elmer) were used in a Hanbury-Brown and Twiss (HBT) interferometer configuration. This allowed for either a single APD to be used for fluorescence detection, or for both detectors to be used to measure the second-order autocorrelation function $g^{(2)}(\tau)$. For lifetime measurements, a different set of APDs were used (id100-20-ULN; ID Quantique), as they have a faster response time at the expense of detection efficiency.

A photon correlator (PicoHarp 300; PicoQuant) was used to collect both the lifetime and the autocorrelation measurement data. For the lifetime measurement, the start and stop signals passed to the PicoHarp were the electronic laser trigger signal and the signal from the detection APD, respectively. For the second-order autocorrelation measurements, the start and stop signals originated from photons detected by the APDs in the HBT configuration.
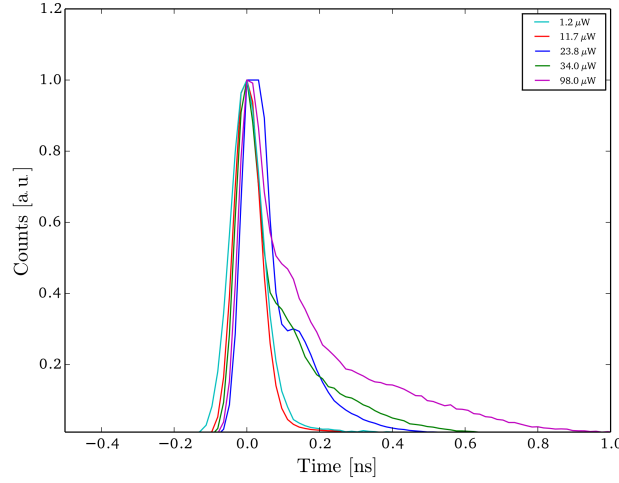
Figure 3.2: Laser pulse shapes at various laser power settings. Correlations between the electronic laser trigger pulse and the laser photons arriving at an APD, recorded at 5 MHz pulse repetition rate. Care was taken to ensure all measurements were conducted below the threshold where the pulse shape deteriorated.

Table 3.1: ND sample properties. The table summarizes the key properties of the ND sample. These values are extracted from physical and optical measurements of the NDs, presented themselves in Figure 3.5.

Mean ND size	(110 ± 30) nm
Mean NV concentration	$9,500$
Mean NV ZPL FWHM	2.09 nm
Mean NV ZPL position	(639.1 ± 0.7) nm

To filter for NV emission (Figure 3.3), either long pass filters were used (FEL0650, FEL0700; Thorlabs), or in the case of second-order correlation function measurements a spectrometer acting as a monochromator to select only the NV ZPL (SpectraPro Monochromator Acton SP2500, dispersion 6.5 nm/mm at 435.8 nm; Princeton Instruments).

3.2.2   Materials

The full characterisation of the material had been carried out for the near-resonant trapping experiment performed in our laboratory [26]. A summary of the sample's properties is shown in Table 3.1. A control sample was also prepared which consisted of synthetic type-Ib ND powder (MSY $\leq 0.1\,\mu$m; Microdiamant) containing mostly single, or at most a few, NV centres [26].

Sample Preparation

The ND sample was purified in concentrated sulphuric and nitric acid (H_2SO_4-HNO_3), rinsed in deionized water, irradiated by a 3 MeV proton beam with a dosage of 1×10^6 ions per cm^2, and annealed in vacuum at 700 °C for 2 hours to induce the formation of NV centres (Academia Sinica, Taipei Taiwan [145]). The sample (0.1 g/ml concentration) was then
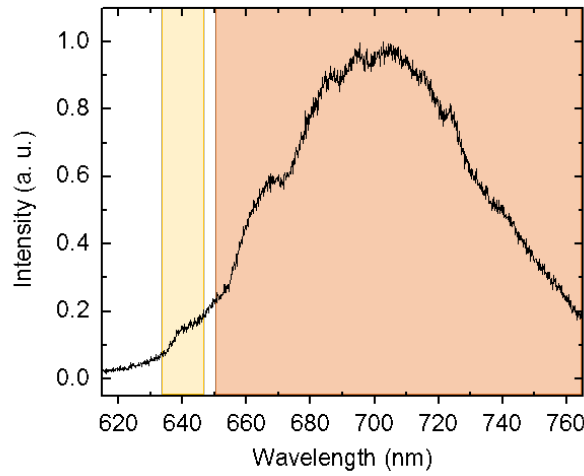
Figure 3.3: Spectrum of the NV centre with filtering bands overlaid. Representative spectrum of an NV centre recorded for the study. The leftmost highlighted band (yellow) marks the narrow spectral region where photons were collected when directing the collection path through a monochromator. The rightmost band (orange) shows the region of photon collection with the filters in place. This spectrum is from an ensemble of NV centres and the therefore the ZPL is not visible due to inhomogeneous broadening. In the context of superradiance, this does not hinder the mechanism as within the range of the ZPL there will be overlapping ZPLs.

dropcast on a 150 μm thick BK7 glass coverslip (BB022022A1; Menzel-Glaser), which had been sonicated and rinsed in acetone (C_3H_6O, purity $\geq$ 99.5; Sigma-Aldrich) for 10 minutes.

Nanodiamond Size

Atomic force microscopy measurements of the nanodiamond sample were undertaken. We measured a mean ND size of (110 $\pm$ 30) nm.

Optical Properties

We investigated the photoluminescence spectra of the nanodiamonds to extract information on the NV ZPL. We measured the mean FWHM of the ZPL to be 2.09 nm, approximated by fitting a normal distribution to the collected spectra, Figure 3.5a. We determined the mean position of the ZPL to be (639.1 $\pm$ 0.7) nm, extracted from a fitting to the data with two normal distributions, Figure 3.5b.

NV Concentration

The mean concentration of NV centres in each ND is estimated to be 9,500. The sample [145] had been proton-irradiated and annealed to increase the formation of NV centres: a resulting concentration of 300 ppm Nitrogen was achieved, with 1 in 10 nitrogen atoms estimated to form an NV centre upon annealing (NV concentration $\sim$ 30 ppm). Figure 3.5c shows the estimated concentration of NVs per nanoparticle normalised to a 150 nm ND ($\sim 3 \times 10^6$ NV/μm^3) as determined by the Nitrogen concentration given by the sample provider. We confirmed this estimated concentration of NV per ND by measuring the photon counts from tens of NDs. This value is in agreement with Table 3.2, which contains the
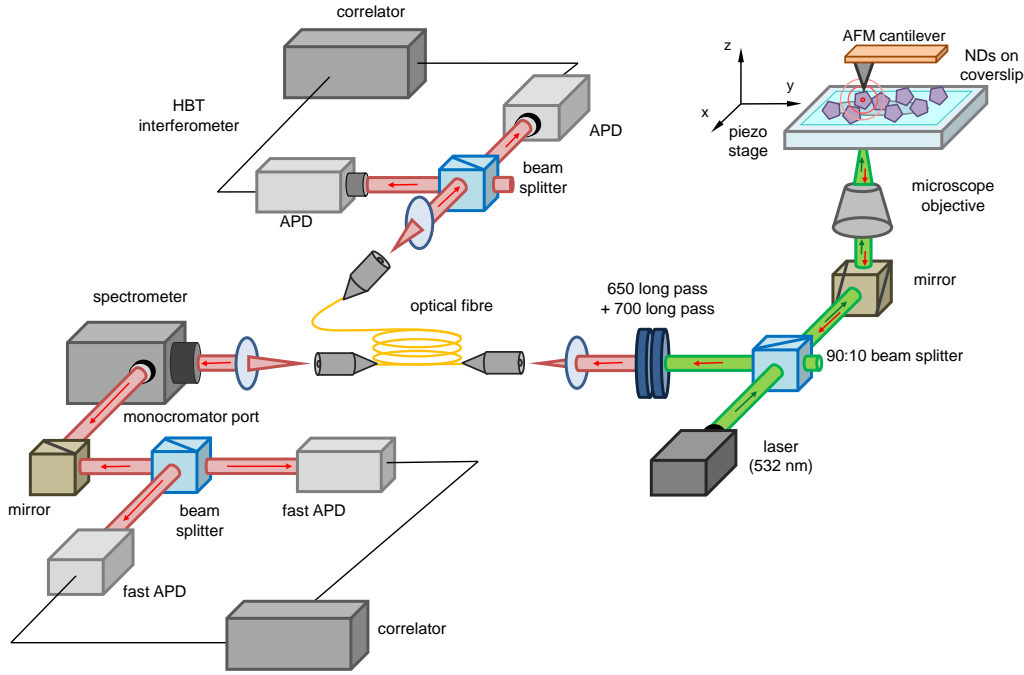
Figure 3.4: Experimental setup for the investigation of superradiant emission. The schematic shows the combined confocal and atomic force microscopy (AFM) setup and peripheral instrumentation, used in this experiment. A pulsed 532 nm laser (operating at either 5 MHz or 20 MHz) is directed to the ND sample. The collection path is first filtered to remove the excitation light, then coupled to a single-mode optical fibre acting as a pinhole. The collected light is then parsed to various detection paths: 1) to slower, more efficient APDs, 2) to faster, less efficient APDs, or 3) to the spectrometer. Each set of APDs is arranged in the Hanbury-Brown and Twiss (HBT) configuration in order to conduct autocorrelation measurements. Autocorrelation measurements presented in this thesis (and the published manuscript) were recorded on the faster, less efficient set of APDs after filtering the collected photons through the spectrometer functioning as a monochromator.

estimated number of NVs centres for NDs of various sizes based on the concentration given by the sample provider.

3.2.3   Laser Power

For each measurement the laser power was selected such that we operated it in the linear regime of the NV saturation curve. For the four representative NDs, saturation curves are shown in Figure 3.6. Care was also taken to only operate at laser powers which preserved good pulse shape, Figure 3.2.

3.2.4   Representative Lifetime Results

One of the most characteristic indicators of superradiant behaviour is accelerated optical emission, where the intensity of the radiation burst scales faster than linearly with the number of emitters. We thus performed fluorescence decay measurements on 100 individual NDs
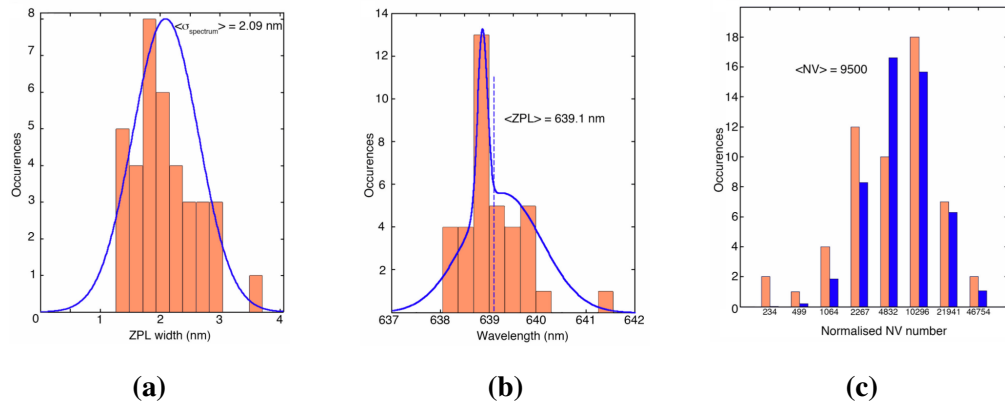
Figure 3.5: Sample characterisation. Adapted from [26], 40 NV spectra from the ND sample were analysed — data is presented in orange and fitted models in blue. **a)** Mean ZPL FWHM estimated at 2.09 nm, approximated by fitting a normal distribution to the collected spectra. **b)** Mean ZPL position determined at (639.1 ± 0.7) nm, extracted from a fitting to the data with two normal distributions. **c)** Estimated number of NV centres in the nanodiamonds, with a mean value of 9,500, normalised to a nanodiamond 150 nm in size.

(see Figure 3.7). We measured lifetimes with decay rates much faster than that of single NV centres (Figure 3.8 shows the lifetimes of four representative NDs in contrast to the lifetime of a single NV center).

To extract the indicative lifetime of each fluorescence decay curve a standard exponential was fitted to the first 3 ns of each dataset. The model (§ 3.3), convolved with the system response, fitted to each of the representative fluorescence decay curves shows excellent agreement with the recorded data (Figure 3.15). The fitting was done by assuming each ND had a distribution of domain sizes, i.e. the number of spins acting cooperatively in each domain. This distribution was assumed gaussian, and the most likely number was taken to be $N_{\text{coop.}}$. This indicative size, $N_{\text{coop.}}$, was taken to be the primary fitting parameter, with other parameters such as the local dephasing, local density of states, and spin polarisation varying but remaining broadly consistent across all NDs. $N_{\text{coop.}}$ was extracted for each ND, and was found to be $N_{\text{coop.}} = 2$, $N_{\text{coop.}} = 7$, $N_{\text{coop.}} = 10$, and $N_{\text{coop.}} = 50$ respectively for ND#1, ND#17, ND#29, and ND#56.

Fluorescence from emitters acting cooperatively should also result in photon-bunching (in this case at the $\sim$ ns time scale) in the second order autocorrelation measurement. The degree of bunching depends on the number of cooperative centres per diamond, $N_{\text{coop.}}$, and the initial state of the system. We thus performed autocorrelation measurements in the next stage of our experiment (§ 3.5).

3.2.5 Systematic Decay Rate Analysis

Through the analysis of the complete dataset of 100 NDs we were able to extract some systematic results. When analysing the decay rate of each ND as a function of ND size, we found that smaller NDs (size < $\sim$80 nm) never displayed superradiant behaviour (Figure 3.9). This is likely explained by these NDs not hosting a high enough number of indistinguishable NV centres. Note that the number of NV scales rapidly with the volume of the ND host, and of all the hosted NVs only a subset will have the requirements of indistinguishability needed

Table 3.2: Defect concentrations. Estimated number of nitrogen atoms and NV defects for NDs of a given size. The diamond unitary cell volume is 45.12×10^{-3} nm^3 and the NV density 5.32×10^6 #/μm^3.

Diameter (nm)	Volume (nm^3)	No. Atoms	Nitrogen @300ppm	No. NVs (1 in 10 Nitrogens)
5	65.42	11.60×10^3	3	0
10	523.33	92.80×10^3	28	3
15	1.77×10^3	313.18×10^3	94	9
20	4.19×10^3	742.35×10^3	223	22
25	8.18×10^3	1.45×10^6	435	43
35	22.44×10^3	3.98×10^6	1.19×10^3	119
50	65.42×10^3	11.60×10^6	3.48×10^3	348
70	179.51×10^3	31.83×10^6	9.55×10^3	955
80	267.95×10^3	47.51×10^6	14.25×10^3	1.43×10^3
100	523.33×10^3	92.79×10^6	27.84×10^3	2.78×10^3
150	1.77×10^6	313.18×10^6	93.95×10^3	9.40×10^3
200	4.19×10^6	742.35×10^6	222.71×10^3	22.27×10^3
1000	523.33×10^6	92.79×10^9	27.84×10^6	2.78×10^6
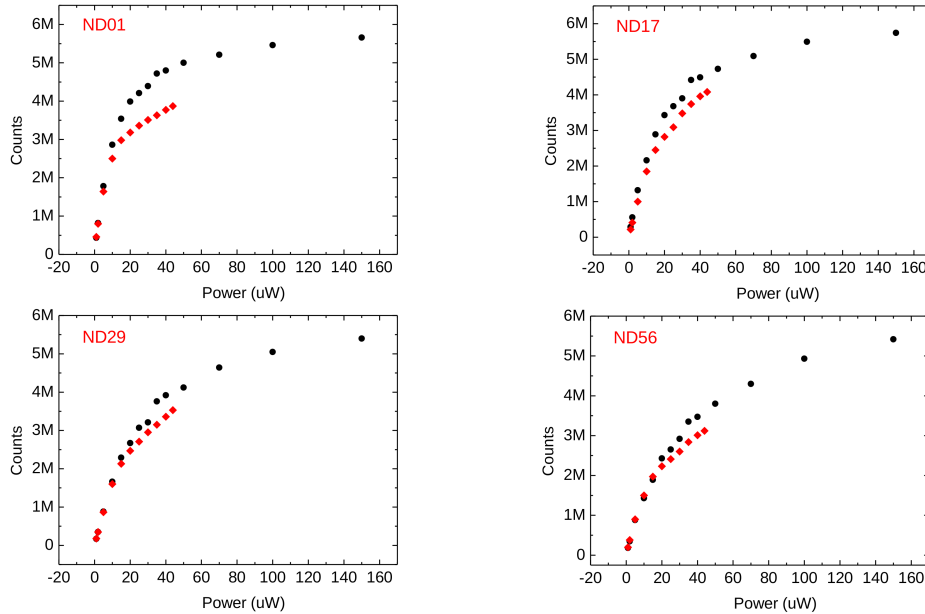
Figure 3.6: Representative saturation curves. Saturation curves of four representative NDs. Red data-points refer to excitation with the pulsed laser, whereas black data-points refer to excitation with the CW laser. The laser power was selected such that measurements were conducted in the linear regime of the NV saturation curve.
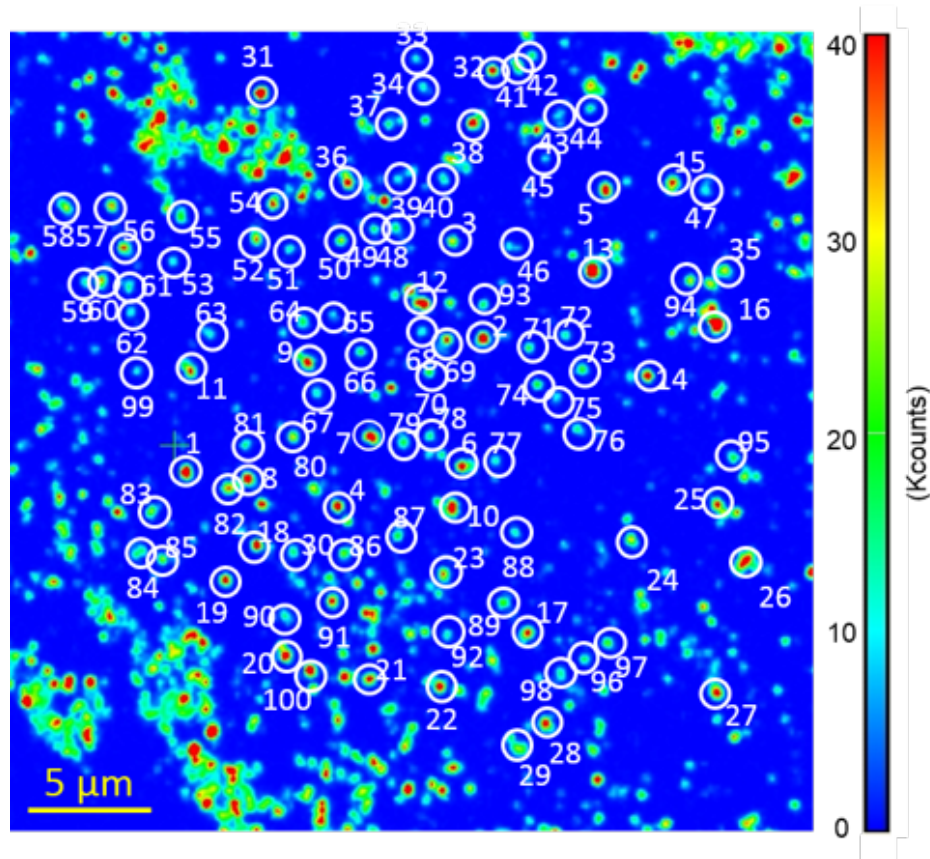
Figure 3.7: Confocal map. A $40\,\mu m \times 40\,\mu m$ confocal map with each of the investigated 100 NDs annotated. The sample was prepared as outlined in §3.2.2.

to act cooperatively. It is also possible that in this size domain (increased surface to volume ratio) surface effects, such as stray charges, could contribute to preventing superradiant behaviour.

The measured decay rates are however consistent with the superradiance model we developed for diamond NV centres (§ 3.3). It should be noted that previous studies reported a decrease in the NV lifetime for centres produced via low-energy He-ion irradiation [146, 147]. This effect has been attributed to increased damage in the crystal lattice which provides non-radiative ('dark') decay paths with faster dynamics. However, we rule out this possibility as we find a direct correlation between short lifetimes and high brightness of the ND (Figure 3.10), which is inconsistent with the shortening of the lifetime be due to 'dark' decay channels (such a model would be independent of the ND size), see § 3.4. To further rule out this possibility we fitted our lifetime measurements with both bi-exponential and deformed exponential curves (which would suit the non-radiative decay path model), but found that these fits were worse than those produced by our model of superradiant emitters.

In detail, we analysed the decay rate of each ND as a function of its peak brightness (Figure 3.10). The peak brightness of each ND was normalised the volume of the ND (Table 3.3) to account for the fact that larger NDs contain on average a greater number of NV centres, thus making them intrinsically brighter. We see that NDs displaying shorter lifetimes are indeed brighter — again consistent with superradiant behaviour rather than with the model predicting dark decay channels [146, 147], see § 3.4.
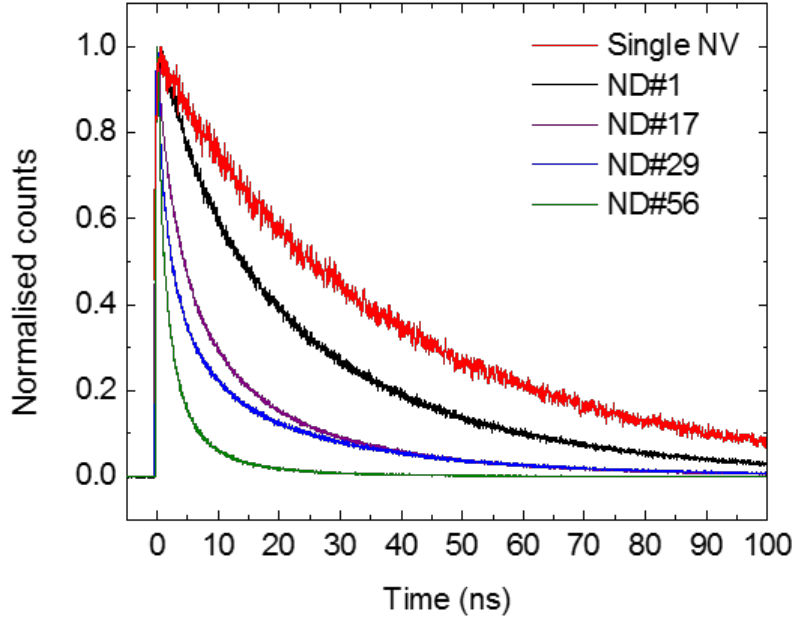
Figure 3.8: Representative lifetimes. Measured lifetimes of a single NV centre (red trace) and four representative NDs from the investigated sample. The four representative NDs have lifetimes consistent with superradiant behaviour. The recorded lifetimes shown are 25 ns, 3.6 ns, 2.2 ns, and 1.1 ns for ND#1, ND#17, ND#29, and ND#56 respectively.

Interestingly we also find, through analysis of the density of NVs for each ND (Figure 3.11), absence of fast-decaying NDs containing very high densities of NV. This is somewhat counter-intuitive, however, it is not completely unexpected. An in-depth study conducted in our group has shown that a too-high concentration of NVs can lead to local dephasing (breaking of indistinguishability) due to dipole-dipole interactions which destroy the collective effects [148].

3.3   Model

In order to understand superradiance theoretically, we first consider a heuristic model for a small system of three atoms (this can be generalised to more complex systems of emitters with a discrete dipole-allowed transition). In the model factors such as decoherence are initially neglected. The model is then expanded to included the effects of dephasing.

3.3.1   Heuristic Model

Consider three atoms

We describe the behaviour of a 2-level system as a pseudo spin-1/2 system, with the notation $|\downarrow\rangle$ describing it as being in the ground state, and $|\uparrow\rangle$ as it being in the excited state. For the purpose of this exercise we now consider three atoms, each initially in their ground state. The system can then be described by the notation

Table 3.3: Normalised ND brightness. Normalised ND brightness for the first 24 NDs in the sample of 100 NDs.

ND #	Diameter (nm)	Intensity (kCounts/s)	Volume (nm^3)	Intensity to Volume (a.u.)
1	32	38	17.15×10^3	2.22
2	42	75	38.77×10^3	1.93
3	70	83	179.50×10^3	0.46
4	45	38	47.69×10^3	0.80
5	40	175	33.49×10^3	5.23
6	30	53	14.13×10^3	3.75
7	10	17	523	32.48
8	20	30	4.18×10^3	7.17
9	17	27	2.57×10^3	10.50
10	30	100	14.13×10^3	7.08
11	95	705	448.69×10^3	1.57
12	22	80	5.57×10^3	14.36
13	53	460	77.91×10^3	5.90
14	31	72	15.59×10^3	4.62
15	81	52	278.12×10^3	0.19
16	50	46	65.42×10^3	0.70
17	100	1460	523.33×10^3	2.79
18	26	55	9.20×10^3	5.98
19	90	43	381.51×10^3	0.11
20	75	193	220.78×10^3	0.87
21	80	690	267.95×10^3	2.58
22	108	550	659.25×10^3	0.83
23	150	1400	1.77×10^6	0.79
24	60	17	113.04×10^3	0.15

$$|\psi\rangle = |\downarrow\downarrow\downarrow\rangle \tag{3.1}$$

Now, let the system absorb a single photon. If the three atoms are confined to a volume smaller than that of the wavelength of the incoming photon ($V \ll \lambda^3$), then it is impossible to assign which atom has absorbed the photon (indistinguishability). The system state is then described by the following:

$$|\psi\rangle = \frac{1}{\sqrt{3}} \left(|\uparrow\downarrow\downarrow\rangle + |\downarrow\uparrow\downarrow\rangle + |\downarrow\downarrow\uparrow\rangle \right) \tag{3.2}$$

Note that this state is symmetric, and in fact it is the only state where you can rearrange or swap any pair of atoms and always have the same state. The state is permutation-symmetric: every atom is indistinguishable from any other atom (for the case of a single excitation in the system).
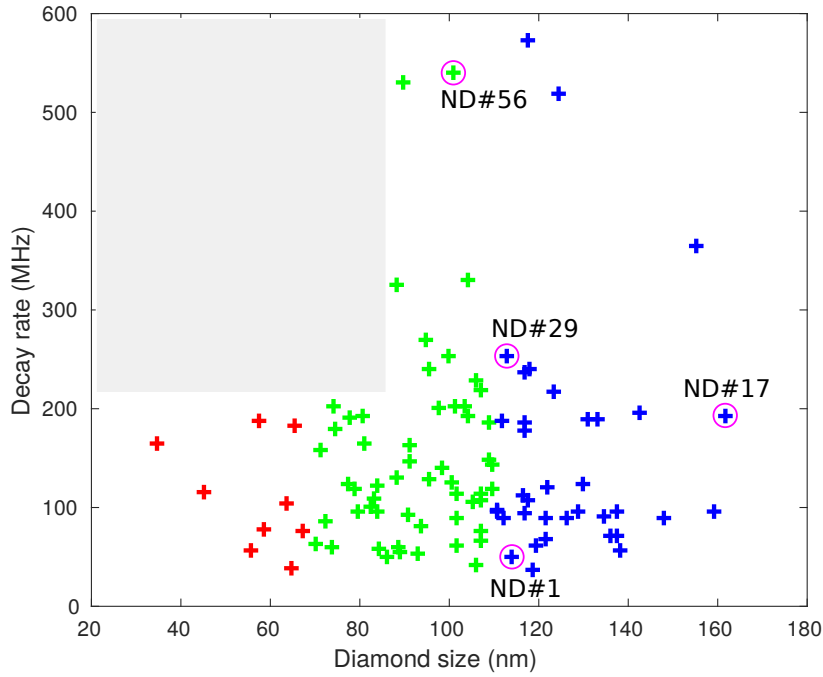
Figure 3.9: Size systematics of the 100 NDs. We can observe that smaller NDs do not show superradiant behaviour, likely because they do not contain enough NV centres to be superradiant. This 'forbidden region' is shaded in the plot above, and is consistent with our model of collective decays. Data-point colour coding represents ND diameter: red < 70 nm, 70 nm ≤ green ≤ 100 nm, and blue > 110 nm.

Generalisation

It can be seen that as the number of atoms and photons in the system grow, so does the complexity of our notation (in fact it grows with exponential rate). Therefore, we generalise. In our model we consider the NV centre to be a two-level system with a ground and an excited state. We can thus describe it as a "spin-1/2" system and use the mathematics of spin operators, but with a caveat. To preserve the condition of indistinguishability for a system of N emitters we need to define a collective spin operator. Let us first start by defining the spin operator $\hat{S}_i$, for each of the N atoms, where i refers to the index of the corresponding atom, i.e. $\hat{S}_1, \hat{S}_2, \ldots, \hat{S}_N$.

The $\hat{S}_1$ operator acts on the z component of the first atom and measures if the atom is in the ground or excited state. For example, if we apply $\hat{S}_1$ to the ground state $|\downarrow\downarrow\downarrow\rangle$, we have:

$$\hat{S}_1 \, |\downarrow\downarrow\downarrow\rangle = -\frac{1}{2} \, |\downarrow\downarrow\downarrow\rangle \tag{3.3}$$

Let us now apply the spin operator to the symmetric state of our three-atom system for the case of one of the three atoms being in the excited state and the other two in the ground state. We obtain:

$$\hat{S}_1 \frac{1}{\sqrt{3}} \left(|\uparrow\downarrow\downarrow\rangle + |\downarrow\uparrow\downarrow\rangle + |\downarrow\downarrow\uparrow\rangle \right) = \frac{1}{\sqrt{3}} \left(\frac{1}{2} \, |\uparrow\downarrow\downarrow\rangle - \frac{1}{2} \, |\downarrow\uparrow\downarrow\rangle - \frac{1}{2} \, |\downarrow\downarrow\uparrow\rangle \right) \tag{3.4}$$

$$= \frac{1}{2\sqrt{3}} \left(|\uparrow\downarrow\downarrow\rangle - |\downarrow\uparrow\downarrow\rangle - |\downarrow\downarrow\uparrow\rangle \right) \tag{3.5}$$
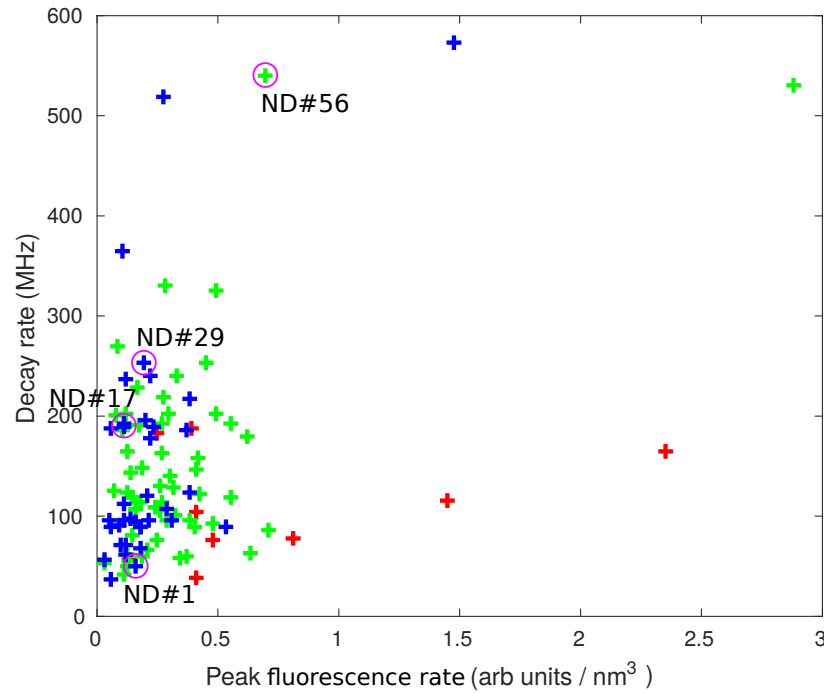
Figure 3.10: Brightness systematics of the 100 NDs. We observed some NDs that are both bright and superradiant, indicating that the decrease in the lifetime is not due to dark decays. To extract the indicative lifetime of each fluorescence decay curve a standard exponential was fitted to the first 3 ns of each dataset. Data-point colour coding represents ND diameter: red < 70 nm, 70 nm ≤ green ≤ 100 nm, and blue > 110 nm. Note the fact that bright centres with short lifetimes are present indicates that in specific cases superradiance is observed. It is indeed possible to find bright NDs with long lifetimes. These refer to the 'standard case' of many NV centres (bright signals) which are not superradiating (i.e. have long lifetimes).

This result shows that the spin operator $\hat{\boldsymbol{S}}_i$ is not a useful operator if we wish to retain a permutation symmetric state. That is, the state obtained after applying $\hat{\boldsymbol{S}}_1$ no longer has the property that exchanging any two atoms leaves the state unchanged.

We thus introduce the collective spin operator $\hat{\boldsymbol{S}}$ such that $\hat{\boldsymbol{S}} = \hat{\boldsymbol{S}}_1 + \hat{\boldsymbol{S}}_2 + \cdots + \hat{\boldsymbol{S}}_N$. If we now take the same example as before and use the collective spin operator $\hat{\boldsymbol{S}}$ instead of the single spin operator $\hat{\boldsymbol{S}}_1$ we get:

$$\hat{\boldsymbol{S}} \ket{\psi} = \frac{1}{\sqrt{3}} (\hat{\boldsymbol{S}}_1 (\ket{\uparrow\downarrow\downarrow} + \ket{\downarrow\uparrow\downarrow} + \ket{\downarrow\downarrow\uparrow})) + \hat{\boldsymbol{S}}_2 (\ket{\uparrow\downarrow\downarrow} + \ket{\downarrow\uparrow\downarrow} + \ket{\downarrow\downarrow\uparrow})$$
$$+ \hat{\boldsymbol{S}}_3 (\ket{\uparrow\downarrow\downarrow} + \ket{\downarrow\uparrow\downarrow} + \ket{\downarrow\downarrow\uparrow})) \tag{3.6}$$

$$= \frac{1}{\sqrt{3}} ((+ \frac{1}{2} \ket{\uparrow\downarrow\downarrow} - \frac{1}{2} \ket{\downarrow\uparrow\downarrow} - \frac{1}{2} \ket{\downarrow\downarrow\uparrow}) + (- \frac{1}{2} \ket{\uparrow\downarrow\downarrow} + \frac{1}{2} \ket{\downarrow\uparrow\downarrow} - \frac{1}{2} \ket{\downarrow\downarrow\uparrow})$$
$$+ (- \frac{1}{2} \ket{\uparrow\downarrow\downarrow} - \frac{1}{2} \ket{\downarrow\uparrow\downarrow} + \frac{1}{2} \ket{\downarrow\downarrow\uparrow})) \tag{3.7}$$

$$= \frac{1}{\sqrt{3}} (- \frac{1}{2} \ket{\uparrow\downarrow\downarrow} - \frac{1}{2} \ket{\downarrow\uparrow\downarrow} - \frac{1}{2} \ket{\downarrow\downarrow\uparrow}) \tag{3.8}$$

$$= \frac{1}{\sqrt{3}} (- \frac{1}{2} (\ket{\uparrow\downarrow\downarrow} + \ket{\downarrow\uparrow\downarrow} + \ket{\downarrow\downarrow\uparrow})) \tag{3.9}$$

which is a symmetric state and thus an eigenstate of the collective spin operator $\hat{\boldsymbol{S}}$. The spin
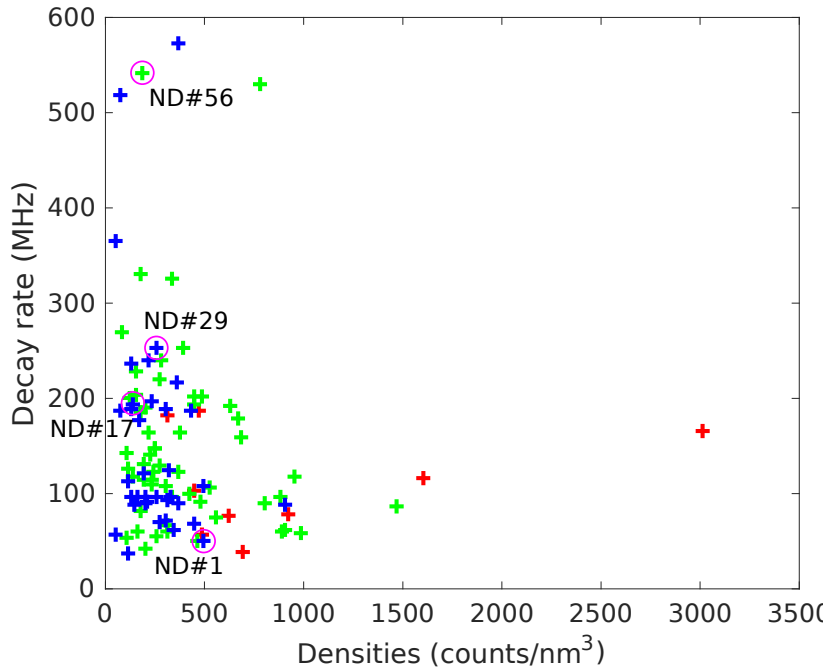
Figure 3.11: NV density systematics of the 100 NDs. The density of NV centres for each ND was determined by fluorescence measurements with a CW 532 nm laser source (via extrapolation from Table 3.2 and Table 3.3). The NV densities are shown in arbitrary units as the quantum efficiencies of the system are unknown, however, their relative values are accurate. The lack of fast-decaying NDs with high NV densities is consistent with our prediction of local dephasing arising from dipole-dipole interactions destroying collective effects. To extract the indicative lifetime of each fluorescence decay curve a standard exponential was fitted to the first 3 ns of each dataset. Data-point colour coding represents ND diameter: red < 70 nm, 70 nm ≤ green ≤ 100 nm, and blue > 110 nm.

projection quantum number is $-1/2$ for this case. Similarly, if two photons were absorbed we would find the spin projection quantum number is $1/2$, and for the excited state (three photons absorbed) it would be $3/2$.

The Dicke Ladder

Having defined the collective spin operator for a many-atom quantum system, we can represent the states, for instance, in the angular momentum basis $|J, M\rangle$ where J is the maximal spin of the collective ensemble (for N atoms $J = N \times 1/2$) and M is the spin projection quantum number such that $-J \leq M \leq J$.

In this notation the ground state would be described by $|\frac{3}{2}, -\frac{3}{2}\rangle$, the state with a single photon absorbed by $|\frac{3}{2}, -\frac{1}{2}\rangle$, and so on. These states constitute what is known as the Dicke ladder, shown in Figure 3.12 for the case of three atoms.

The composite spin operator $\hat{S}$ has associated raising and lowering operators ($\hat{S}^{\pm} = \hat{S}_x \pm i\hat{S}_y$) to move either up or down the Dicke ladder — the raising operator $\hat{S}^{+}$ adding an 'excitation' to the system (the absorption of a photon), and conversely the lowering operator $\hat{S}^{-}$ removing an 'excitation' from the system (the emission of a photon). When applied to our
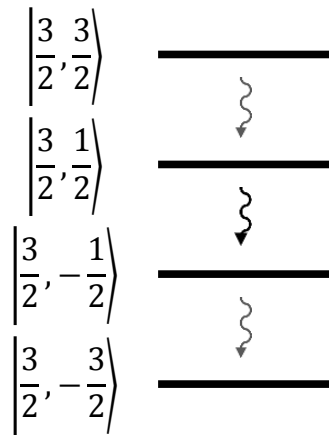
Figure 3.12: Dicke ladder with N = 3. The above provides a representation of the Dicke ladder for $N = 3$, with the states $|J, M\rangle$ appended, and where arrows indicate photon emission.

$|J, M\rangle$ notation, each operator has the following effect:

$$\hat{S}^+ |J, M\rangle = \hbar \sqrt{(J - M)(J + M + 1)} \, |J, M + 1\rangle \tag{3.10}$$

$$\hat{S}^- |J, M\rangle = \hbar \sqrt{(J + M)(J - M + 1)} \, |J, M - 1\rangle \tag{3.11}$$

Let us now specifically discuss the lowering operator $\hat{S}^-$, as we are investigating the 'descent' down the Dicke ladder. The resultant eigenvalue of the state that is produced by applying the lowering operator, $\hbar \sqrt{(J + M)(J - M + 1)}$, is proportional to the rate at which photons will radiate from that particular state. The basis of this proportionality lies in its relation to the number of radiation pathways available to the photons. The flux, F, of photons exiting the system (the system decay rate) is described by the expectation value

$$F = \gamma \langle J, M| \hat{S}^+ \hat{S}^- |J, M\rangle \tag{3.12}$$
$$= \gamma (J + M)(J - M + 1) \tag{3.13}$$

where γ is the decay rate of a single atom.

Superradiance

Within this framework, let us now consider the photon flux at different 'rungs' of the Dicke ladder. The ladder is represented in Figure 3.13a (for $N = 10$, but this will scale for any N).

At the top of the Dicke ladder we have $M = J$, so the photon flux is

$$F = 2\gamma J \tag{3.14}$$
$$= \gamma N \tag{3.15}$$
$$\propto N \tag{3.16}$$

i.e. same rate as N independent emitters.
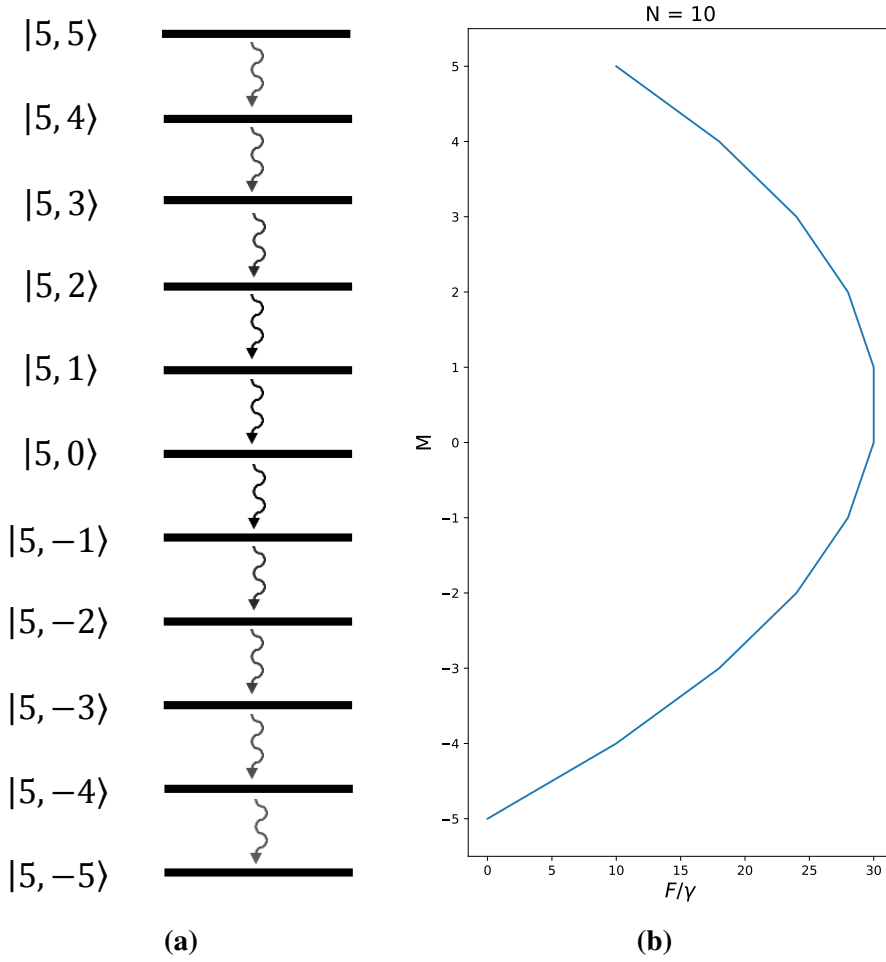
Figure 3.13: Dicke ladder with N = 10. **(a)** A representation of the Dicke ladder for $N = 10$, with the states $|J, M\rangle$ appended. **(b)** First note that this plot is transposed for readability. The photon flux rate, F, (with the individual atom decay rate, γ, factored out) is plotted for each descending step down the Dicke ladder. The flux scales with the square of the number of atoms in the system (§ 3.3), and as can be seen the maximum flux is occurs when the system is maximally mixed in the $|5, 0\rangle$ state (for this example).

At the centre rung, when the system is in the state where it has the most decay paths accessible to it, $M = 0$ and the photon flux is then

$$F = \gamma J (J + 1) \tag{3.17}$$

$$= \gamma \frac{N}{2} \left(\frac{N}{2} + 1 \right) \tag{3.18}$$

$$\propto N^2 \tag{3.19}$$

And it is here that we find the crux of superradiant behaviour — that the photon flux scales as N^2, compared to the factor N we expect from independent emitters.

3.3.2 Applied to the NV Centre

Due to its spin-conserving optical transitions, this means that the $m_S = 0$ and $m_S = \pm 1$ manifolds of the NV centre do not mix in the optical excitation and optical decay process.
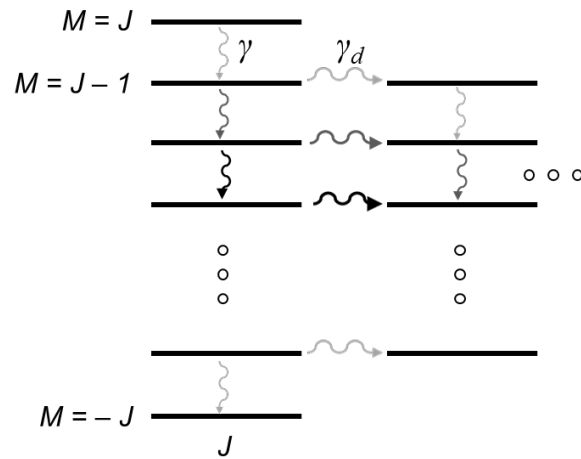
Figure 3.14: Representation of the Dicke ladder. Local dephasing of the system was modelled through the removal of an atom from the collective subspace at a rate γ_d. This removes atoms from the collective subspace (lowering its dimension), essentially 'shortening' the Dicke ladder.

This means we are justified in considering the NV centre as a pair of two-level, pseudo spin-1/2 system, with the $m_S = 0$ and the $m_S = \pm 1$ manifolds remaining separate. Further, we make the assumption that we can treat the overall system as a collection of different spectral domains, each containing some NV centres acting cooperatively (and likely grouped in a corresponding spatial domain within the ND).

Inter-System Crossing Rate

The $m_S = 0$ and $m_S = \pm 1$ population are treated as two separate collections of domains. In addition to the optical decay, there is a non-radiative decay path, the intersystem crossing (ISC) rate. This decay treats the centres collectively, and does not break indistinguishability, but it does reduce the number of centres in the excited state that can undergo superradiance. This has the effect of shortening the Dicke ladder at a rate γ_{ISC}. The dark decay rates from the ISC are not well known, but from the literature [100] we use $\gamma_{ISC}^0/2\pi = 1.8\,\text{MHz}$ and $\gamma_{ISC}^{\pm 1}/2\pi = 9.4\,\text{MHz}$ for the $m_S = 0$ and $m_S = \pm 1$ rates respectively.

Local Dephasing

An additional mechanism that breaks down the collective behaviour of the system is local dephasing rate γ_d. Local dephasing removes atoms from the collective subspace (lowering its dimension), essentially 'shortening' the Dicke ladder, Figure 3.14. Once an atom is 'off the ladder' into the non-collective subspace it decays with the 'classic' lifetime characteristic of an individual emitter.

Lattice Environment (Local Vs Global Phonons)

As discussed in §3.1.1, for cooperative effects to take place the rules of spectral and spatial indistinguishability must be upheld. One of the main issues for superradiance in solid-state systems is the fact that the inhomogeneity of the local environment (e.g. due to stress and strain within the lattice, local fields, intrinsic or extrinsic lattice defects, etc. (§ 1.3.1) destroys the indistinguishability required by the emitters to act cooperatively.

Given these premises, it would seem very unlikely for NV centres in nanodiamond to display superradiant behaviour, especially considering how its radiative decay is heavily affected by local phonons (up to 97% of the NV emission occurs into the phononic side band [149]). Local phonons generated from the excitation of each individual NV centre may be enough to reduce the centres spectral indistinguishability. The spectral information gained from local phonons, however, may be erased since the local phonons rapidly decay (at a ps time scale) into global phonons [150, 151], potentially removing this knowledge. In other words, the local vibrations (local phonons) of individual NV centres are transferred to long-wavelength vibrations (global phonons) extended to the nanodiamond crystal as a whole, thus restoring the indistinguishability of the system and allowing for superradiance to occur.

3.4   Fit to Data

The model we developed to fit the lifetime of superradiant NV centres has four independent parameters: the local dephasing rates (from both the $m_S = 0$ and $m_S = \pm 1$ states), the average number of centres in each cooperative domain N_{coop}, the initial state of the collective space, and the underlying decay rate (different for each ND, a result of the density of states scaling with volume — we this find through fitting to the tail of the decay curve). Across all NDs, the local dephasing rates were broadly similar, and the same initial state was used for all the fits. The distribution of the number of NV centres across the collective domain is characterised by a single free fitting parameter N_{coop}, corresponding to the average domain size. We also assume that each 'rung' on the Dicke ladder (each 'M-level') is equally populated. We found that this assumption is non-critical though, as different distributions across the M-levels provide equally good fits if slightly different dephasing rates are chosen.

With these assumptions and those described above § 3.3.2, our model is in excellent agreement with the collected data for all 100 NDs analysed. Figure 3.15 shows the model fit to our four representative NDs, which when fitted return the number of cooperative NV centres across the collective domain (N_{coop}) spanning from 2 through to 50. For the majority of NDs we find a cooperative domain size of $N_{\mathrm{coop}} \sim 1$–2 centres — indicating the absence of (or very little) cooperative behaviour, and is somewhat expected due to how 'fragile' the indistinguishability condition is for solid-state emitters.

Similarly, we find that the local dephasing rates vary for each ND, with the following values extracted from the fits: $\gamma_{\mathrm{d}}^0/2\pi \sim 20$–40 MHz and $\gamma_{\mathrm{d}}^{\pm 1}/2\pi \sim 300$–450 MHz for the $m_S = 0$ and $m_S = \pm 1$ domains respectively. From the fits we can also extract the initial polarisation of the system (the fraction of spins initially in the $m_S = 0$ state). Across the 100 ND sample we extract this value to be ~ 50–60%. These values are consistent with those shown in the literature for high density NV samples [152, 153].

3.5   Experiment: Photon Correlations

The initial state of the system predicted by the model shows that photon bunching at very short time scales should occur for cooperative NV centres. We thus conducted second-order
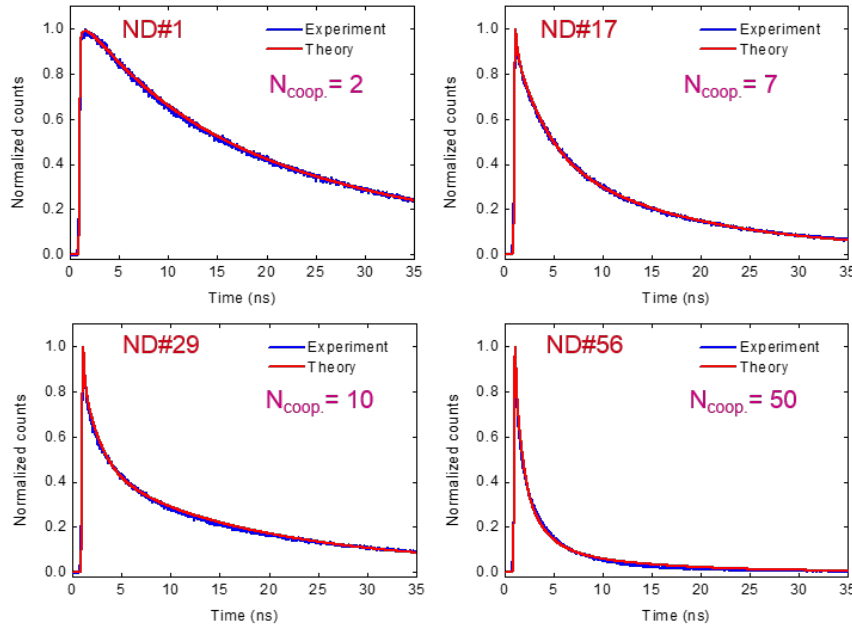
Figure 3.15: Representative lifetimes fitted with the model. Fluorescence decay curves of four representative NDs (blue) and their corresponding lifetime fits (red). The model (§ 3.3), convolved with the system response, shows agreement with the experimental data. Each decay curve is normalised to its own respective maximum count value. Each ND exhibits a different degree of superradiant behaviour, with lifetimes of 25 ns, 3.6 ns, 2.2 ns, and 1.1 ns for ND#1, ND#17, ND#29, and ND#56 respectively. These decays rates have been found by fitting an exponential to the decay rate of the first 3 ns of the data. As such, these lifetimes are purely indicative of speed and are not a rigorous fit. The respective collective domain sizes (average number of cooperative centres per diamond) were found to be $N_{coop.} = 2$, $N_{coop.} = 7$, $N_{coop.} = 10$, and $N_{coop.} = 50$ for ND#1, ND#17, ND#29, and ND#56 respectively.

autocorrelation measurements to verify this. Indeed the degree of photon bunching matched the trend predicted by the model (see below).

3.5.1 Theoretical Realisation

Here I present a short note on the autocorrelation measurement from a theoretical perspective. Detailed calculations written by colleagues can be found in the supplementary material of the paper [122].

In the spin notation utilised in § 3.3, the autocorrelation function $g^{(2)}(\tau)$ can be written as

$$g^{(2)}(\tau) = \frac{\langle \hat{S}^{+}(0)\hat{S}^{+}(\tau)\hat{S}^{-}(\tau)\hat{S}^{-}(0)\rangle}{\langle \hat{S}^{+}(0)\hat{S}^{-}(0)\rangle\langle \hat{S}^{+}(\tau)\hat{S}^{-}(\tau)\rangle} \tag{3.20}$$

For $\tau = 0$ it can be shown that this value is dependent on the initial state of the system. In the case where all eigenstates of the system (rungs on the Dicke ladder) are equally populated, then we would measure

$$g^{(2)}(0) = \frac{6(N-1)(N+3)}{5N(N+2)} \tag{3.21}$$

which approaches $g^{(2)}(0) = 1.2$ as $N \to \infty$.

3.5.2 Experimental Realisation

We performed experimental time-integrated autocorrelation measurements $\overline{g^{(2)}(\tau)}$ for the photons emitted by the four NDs we characterised. Specifically, we measured photon coincidences on a set two APDs arranged in the Hanbury-Brown and Twiss configuration, § 3.2.1. The measurement was conducted with a pulsed laser to increase the signal to noise ratio.

The function is:

$$\overline{g^{(2)}(\tau)} \equiv \frac{\int_{-\tau}^{\tau} dt \, \langle : I(0)I(t) : \rangle}{\int_{-\tau}^{\tau} dt \, \langle I(0) \rangle \langle I(t) \rangle} \tag{3.22}$$

where $\langle I(t) \rangle$ is the expectation value of the luminescence signal intensity. The time-integrated function $\overline{g^{(2)}(\tau)}$ is determined as the ratio between the area (which is proportional to the photon coincidences) under the peak at $\tau = 0$ peak and the average value of the area calculated over all the other peaks for which $\tau \neq 0$ (a ratio > 1 would be a signature of photon bunching). This analysis was repeated by selecting different time slices, see Figure 3.16b — i.e. increasing the basis (time axis) over which the area is evaluated. This is because the fast superradiance dynamics is captured by the coincidences that are the closest to $\tau = 0$. As a result, we expect that the ratio giving $\overline{g^{(2)}(\tau)}$ would approach the standard second order autocorrelation function $g^{(2)}(0)$ for the time slice approaching 0 (and reveal photon bunching for a superradiant ND, i.e. $\overline{g^{(2)}(\tau=0)} > 1$), while increasing the time slice would result in $\overline{g^{(2)}(\tau=0)} \to 1$ (the superradiant coincidences are 'lost' as the value of the area is now dominated by the non-superradiant coincidences away from $\tau = 0$), see Figure 3.16b. Note that as $\tau \to 0$, $\overline{g^{(2)}(\tau)}$ approaches the standard autocorrelation function $g^{(2)}(0)$.

3.5.3 Autocorrelation Results

For these measurements the NV emission was filtered through a spectrometer, Figure 3.3, to ensure spectral indistinguishability of the photons. The data reveals that for fast-decaying NV ensembles we observe $\overline{g^{(2)}(\tau=0)} > 1$, indicating indeed super-Poissonian statistics. For the system with the shortest lifetime, ND#56, we measure a value of $\overline{g^{(2)}(\tau)} = 1.14 \pm 0.02$.

Beyond simply observing super-Poissonian statistics for the photons, what matters is that the value we measured for $\overline{g^{(2)}(\tau)}$ is indeed consistent with the scaling in Equation 3.21, predicted by our model where we assumed an initial collective state where all M eigenstates are equally populated. (Note that in the extreme case where the initial state consists of all spins up — corresponding to all atoms in the collective subspace being excited — we would have $g^{(2)}(0) = 2$ as $N \to \infty$ [122].) The value of $\overline{g^{(2)}(\tau)}$ for ND#56, and that of those collected for ND#1, ND#17, and ND#29, are plotted alongside the values from Equation 3.21 in Figure 3.17.

3.6 Conclusions

The observation of ultra-fast radiative decay and the supporting evidence provided by the time-integrated autocorrelation measurements confirm our hypothesis that cooperative emission does take place in NDs containing ensembles of NV centres. Notably, an accurate model was developed in conjunction with colleagues to capture the superradiance dynamics
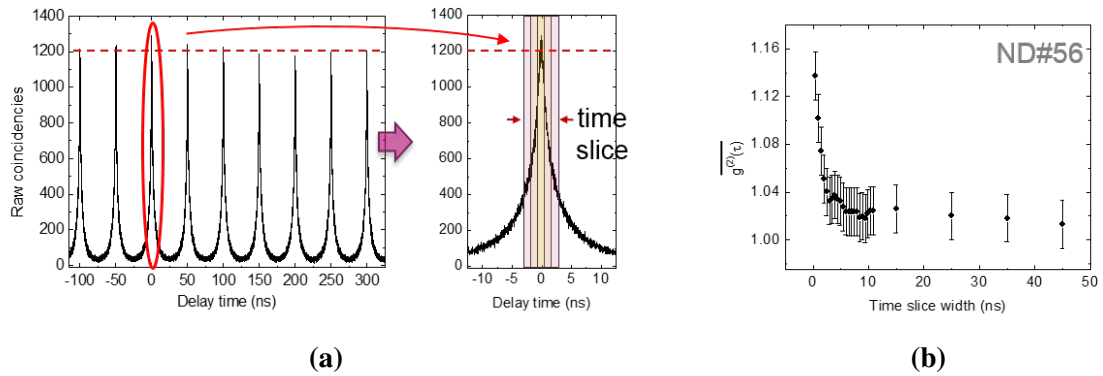
Figure 3.16: Second-order autocorrelation function measurement for ND#56. (a) Normalised coincidence counts for ND#56. **(b)** Time-integrated autocorrelation function $\overline{g^{(2)}(\tau)}$ for ND#56, which approaches $g^{(2)}(\tau=0)$ as $\tau \to 0$. We find that $\overline{g^{(2)}(\tau=0)} = 1.14 \pm 0.02$ for ND#56, with a 0.5 ns time-slice width, indication photon bunching, and then proceeds to drop considerably as the time-slice width is increased above 2-3 ns (after which the superradiant burst is exhausted). After the burst $\overline{g^{(2)}(\tau)}$ then converges to $\sim$1 as expected. Error bars have been determined from the standard error of the peak areas, for each of the time slices, excluding the '0' peak.
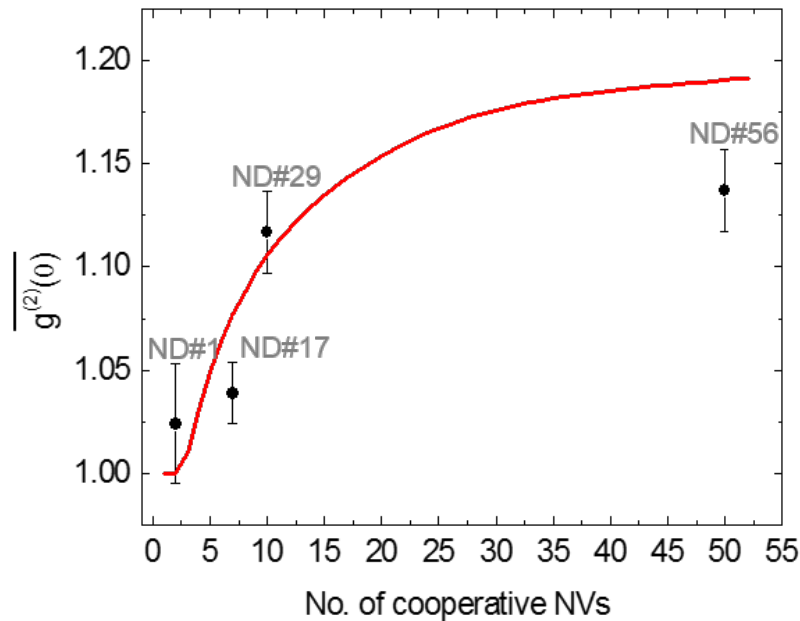
Figure 3.17: Second-order autocorrelation function trend with number of cooperative centres in each diamond. Maximum value of $\overline{g^{(2)}(\tau=0)}$, of each of the representative NDs, plotted against the number of cooperative centres per diamond, $N_{coop.}$. The upper limit of the theoretical model is overlaid (red), which indicates the value of $N_{coop.}$ required to produce the corresponding value of $\overline{g^{(2)}(\tau=0)}$ resulting from the initial conditions of the model. Note that due to the imposed finite time width for averaging ($\sim$0.5 ns), $\overline{g^{(2)}(\tau=0)}$ is an underestimation $g^{(2)}(\tau=0)$. The curve assumes an initial state of the system given by Equation 3.21 (weighted appropriately and summed over the distribution of cooperative domains).

in nanodiamond NV centres. Our observation of superradiance in a true nanoscale, room-temperature solid-state system ignites a wealth of novel research directions, some of which are presented below.

We note that decreases in the lifetime of NV centres have previously been observed in samples that have been produced by low-energy He-ion irradiation (with the reduction in lifetime proportional to the increase of irradiation dose) [147]. This observation can be attributed to damage within the crystal lattice providing additional non-radiative dark decay pathways, with faster system dynamics [146]. However, our investigations show that we observe the opposite trend — that NDs with a higher peak fluorescence (brightness) correlate with faster decay rates (shorter lifetimes), see Figure 3.10. To quantitatively check against this explanation we fitted our lifetime measurements with both bi-exponential and deformed exponential curves, however, both gave worse fits than our model. To conclude, the observation of superradiance in diamond nanoparticles is an intriguing finding, with applications that can range from energy harvesting to enhanced optical trapping, as discussed at the beginning of the chapter.

3.6.1   Future Work

Temperature Dependence

The most immediate follow-up to my work would be an investigation into the dependence of superradiance in diamond NV centres with temperature. Predicting what would be the effect of, for instance, reducing the temperature is non-trivial. Lowering the temperature will reduce the populations of both local and global phonons which, as discussed, act oppositely for the occurrence of superradiance in NV centres, § 3.3.2. On one side, having fewer local phonons may improve the indistinguishability of the different NVs (by removing one channel by which each NV centre is locally different, i.e. distinguishable, from any other), meaning the majority of the optical decay is on the ZPL, and hence spectrally indistinguishable. On the other hand, having fewer global phonons might reduce the probability for the still existing local phonons to decay into long-wavelength lattice vibrations, which we have seen may play a role in 'inducing' indistinguishability amongst NV centres, § 3.3.2.

Dipole-Dipole Interactions

If the NV centres are packed with too high a density, dipole-dipole interactions are expected to partially destroy the cooperativity between NV centres [148, 154]. However, at the same time, such interaction may be a contributing factor to superabsorbing systems [155].

Superabsorption

The main focus of my work has been superradiance in diamond NV centres which, in the Dicke model, is described by the lowering collective spin operator acting on the collective symmetric state. A natural extension would be to consider the opposite raising spin operator and the associated phenomenon of superabsorption — i.e. the converse effect to superradiance which should be present in systems that are superradiant. Although superabsorption is not favourable for systems such as nanodiamond NV centres, it has been proposed that arranging atoms in particular geometries may enable this effect [155].

Deterministic Surperradiance

The consideration that the way the emitters are organised relative to one another might contribute to the creation of Dicke states leads potential interest in engineering specific geometries to enhance superradiant emission. For instance, a combination of deterministic colour centre creation [156] and material engineering [157, 158] could be utilised to create spatial arrangements of colour centres in supporting environments.

The Silicon-Vacancy Colour Centre

Another avenue of research is to look for other analogous solid-state systems. For instance, the silicon-vacancy colour centre (SiV) in diamond has a much narrower ZPL and a much lower Debye-Waller factor with $\sim 80\%$ of photon emission into the ZPL [3], which could be favourable for the observation of superradiance. The recent report of superradiant behaviour from 2 SiV centres by Lukin's group [142] constitutes a first step in this direction.

4

Upgrading Laboratory Capabilities

"In a properly automated and educated world, then, machines may prove to be the true humanizing influence. It may be that machines will do the work that makes life possible and that human beings will do all the other things that make life pleasant and worthwhile."

Isaac Asimov

Over the course of conducting our measurements on NV superradiance we observed degradation in the performance of our NT-MDT piezoelectric scanning stage. The NT-MDT stage performed as an integral component of our primary confocal system, and was the essential work-horse instrument for our lab measurements. With the reliability of the stage decreasing daily a replacement NT-MDT system was ordered.

With our primary piece of lab equipment off-line it was decided to undertake a significant process of modernisation and automation of our lab systems — with the desire to build an integrated setup with the capability of conducting semi-autonomous measurements. In all previously-conducted experiments, each instrument in the lab functioned in isolation, requiring each parameter to be manually adjusted for each measurement on each sample. In experiments requiring a large sample size of NDs, such as the NV superradiance measurement (see Chapter 3, with a 100 ND sample size), manual acquisition of the data became a taxing exercise. It was also realised that a high dependence on human-manned operations was hindering the progress of some of our projects. With a semi-autonomous lab control system in place, experiments could be run 'around the clock' without the human requirement to sleep.

The installation of a lab control system would then enable a shift in how we carry out our experiments — with data collection and real-time analysis directly influencing the direction of our on-going research on a faster time-scale. Our mode of operation transitioned from being task focused; spending human time to conduct measurements, to being outcome focused; using machines to conduct measurements, and humans for interpreting data and deciding on the next course of action.

4.1   Requirements

To undertake such an endeavour from first principles would require a significant time commitment. Should pre-existing solutions be available to be implemented, an adoption of a platform would enable the process of modernisation and automation to be accelerated. Prior to seeking out such solutions a set of requirements for the adopted platform was composed.

Nil loss of capabilities

Our primary method for ND characterisation is confocal microscopy. The chosen solution must be capable of coordinating the synchronised control of an excitation laser, movement of the scanning piezo-electric stage, collection of photon counts from an avalanche photo-diode (APD), control of a spectrometer, and acquisition of second-order auto-correlation measurements for identifying single-photon sources.

Open-source solution

The motto of the Royal Society is "Nullius in verba", or "on the word of no one" [159]. The phrase is "an expression of the determination of Fellows to withstand the domination of authority and to verify all statements by an appeal to facts determined by experiment", generally conveying that all theories must be open to being questioned and all results should be repeatable. To embody this ethos and keep the methods of our science 'open', it is desirable for our team to utilise and contribute to an open-source project.

Existing instrument support

In order to avoid re-developing pre-existing hardware communication code, consideration would be given to platforms already supporting our lab instruments. As many other researchers around the world conduct similar research on diamond colour centres with dedicated lab control systems, this was a known possibility.

Version control system integration

The maintenance of version control through a purpose-built platform has been common place in the field of computer science for some time, but has been slow to be adopted in the broader science community. Incorporating this functionality into our system would allow for flexibility in future upgrades and developments. With the above features in consideration for a lab control system solution, our team converged on one suitable option: Qudi [160].

4.2   Reviewing Qudi and its Design Principles

Qudi (quantum diamond) is a lab control system specifically created for labs researching diamond colour centres [160]. The project origins stem from the University of Ulm in Germany, where in 2015 its creators realised a similar desire to conduct automated measurements.

4.2.1   Programming Language

Qudi is written in the Python scientific programming language, popular in science because of its high-level of abstraction which makes the code human-readable and concise [161,
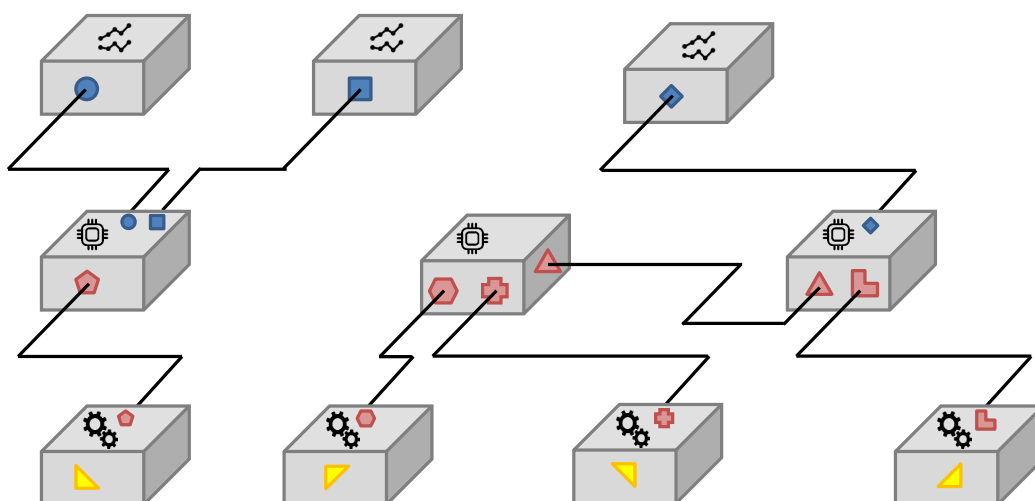
Figure 4.1: Qudi modular and hierarchical system architecture. The modular design principles of Qudi provide complete hardware abstraction and allows for the parallel configuration of numerous instruments. Graphical user interface modules are at the top level of the design hierarchy, here marked with blue input ports. These communicate with logic modules, marked with red input ports, which can be thought of as the 'brain' layer in the hierarchy. At the lowest level are the hardware modules, marked with yellow input ports, which take commands from the logic and convert them into signals that communicate then directly to physical hardware. In the case demonstrated, the central logic module behaves as an 'interfuse' — it appears as though it is a hardware module but itself communicates with two independent hardware modules.

162]. Its availability (freely usable and distributable) and modular structure have fostered a large amount of community support built over the last decade, reducing the steepness of the learning curve required to start using the language. Moreover, many lab instruments now ship with a Python accessible application programming interface (API), which would accelerate their integration into the lab control system.

4.2.2 System Architecture

The design of Qudi is segmented into modules, with each connected to either parent or child (or both) modules by a centralised manager. The manager handles the arrangement of the modules as the user has specified in a configuration file. These modules are compartmentalised into three functions; hardware/software interfacing, experiment 'logic', and graphical user interface (GUI). These 'layers' of the system are hierarchical (see Figure 4.1) — a GUI module cannot directly take input from a hardware interface module without first being passed through a logic module. This compartmentalisation brings with it a great advantage: the abstraction of the specific communication protocols required to communicate with each individual lab instrument. It is ultimately the modularisation and abstraction of code that forges Qudi into an adaptable lab control system.

Graphical User Interface

The GUI operates at the highest level in the architecture hierarchy (excluding the manager), providing the user with a portal to interface with and control the experiment. GUIs present the data to the user (in the form of live plots or simply instrument status) and also allow the user to control instruments (i.e. change the position of a stage or adjust laser power).

A user may also choose to interact with the Qudi lab control system without the GUI — e.g. via a pre-programmed script listing a set of automated tasks. Interactions with the logic modules can be made directly with an integrated console, or, via a Jupyter notebook. This scripted interacting is a powerful tool for easily creating long measurement sequences to explore large parameter spaces through the use of nested for loops.

Logic

Logic modules exist to control and synchronise experiments, taking inputs from either the GUI or a scripted input and subsequently issuing commands to and receiving signals from the abstracted hardware modules. These modules can connect to single or multiple lab instruments. For example, a 'confocal logic module' is required to communicate with, at a minimum, a scanning stage and a photon counting device. They handle all computations and conversions, such as the conversion of raw signal arrivals from a photon counting device and presenting that simply as photon counts per second.

Hardware/Software Interface

Most lab instruments have the ability of be controlled remotely via a computer. Unfortunately, due to the proliferation of hardware and software 'standards'[i], the specific methods of communication (command structure, syntax, measurement units, physical connections, and signal voltages) can differ greatly between devices from different manufactures.

To make the control system hardware agnostic (a piezo-electric stage from manufacturer A must be capable of fulfilling the same basic tasks as a piezo-electric stage from manufacturer B), hardware/software interface modules are where the specifics of communications with each instrument are handled. Each interface module must meet the minimum requirements for the 'type' of hardware it is interfacing with; stages must be able to move to positions, powermeters must be able to report power measurements, lasers must be able to change powers, etc. But the specifics of how these commands are sent and data received are all handled here, and the logic module (the next level up in the hierarchical system architecture) is indifferent to the method — so long as the hardware/software interface module translates its commands appropriately.

This direct device communication excludes devices which can be considered as 'dumb'. For example, an APD to count photons has the sole task of outputting a TTL signal upon the detection of a photon. This is its only function, to 'click', and it passes this signal to a 'smart' instrument which can interpret the significance of those 'clicks'. In the case of 'dumb' hardware, data acquisition (DAQ) devices are used to gather and report these signals.

This hardware level is where I personally focused the majority of my efforts for this project — integrating our specific hardware with the lab control system. See § 4.3 for a demonstration of the hardware/software integration process.

4.2.3   Version Control

The Qudi project is managed by the Git distributed version control system. Managing the development of code with a version control system enables the tracking of code changes over a vast set of files. This is several benefits:

---

[i]If there are 14 competing standards, a 15th standard will be created to unify them [163].

Distributed Development

Each developer stores a complete copy of the code repository locally on their computer. The local repository contains all history of the project (each *commit*) and can function completely offline. The code can then be further developed, or deployed for control machines to operate lab instrument, with no need to have the latest copy of the code or an internet connection.

Non-Linear Development

Perhaps the most innovative feature of the Git version control system is its strong support for non-linear code development. Developers can *branch* code repositories, allowing for development of new features to be conducted in parallel by multiple developers, then each branch can be *merged* back into a functioning *master* branch once the feature has been completed and tested (*stable*). The ease of non-linear development fosters seamless integration of new code and code changes into a centralised repository, where every user can benefit from the work of others.

Scalability

Git is able to handle large code repositories, containing millions of lines of code, without loss of efficiency or speed. Unlimited branches of the code repository can be created and subsequently merged with one-another with no disadvantages to operating at scale.

Community Support

Git was created in 2005 by Linus Torvalds, the creator of the Linux kernel. It has since been widely adopted by software developers, particularly in the open-source community.

Cryptographic Authentication of History

Each *commit* that is made to the code repository is assigned a unique identifying string that is generated using the SHA-1[ii] hashing algorithm. The information used to generate the new commit hash includes the changes that have been made to the code repository and the hash of the previous commit. This feature renders previous commits to the code repository immutable[iii].

Integration with GitHub

GitHub is a web service created to host code that is managed by the Git version control system. The site fosters global collaboration by providing coding projects with a centralised repository for developers to *merge* their work and provides other tools to enhance collaboration.

4.3   NT-MDT Stage Hardware Control

It has already been shown that confocal microscopy is one of the main methods implemented to undertake experiments in the field of diamond nanosicence. An integral component of any

---

[ii]Secure Hashing Algorithm

[iii]Methods do exist to 'change history' inside Git repositories, but there is often little reason to do so.

Figure 4.2: Flow of instrument commands. Control commands, themselves generated by Qudi, for the NT-MDT piezoelectric stage, written in Nova Power Script, were required first to be passed through to the Nova Px software in C.

confocal microscope is a scanning stage capable of raster-scanning the focus across a sample to produce images. Piezo-electric stages are typically used due to their high spatial stability and nanoscale precision. After completing the superradiance measurements reported in Chapter 3, the piezo-electric stage in the AFM-confocal setup was upgraded in an attempt to open the way for expanded investigations of superradiance. This stage was supplied by NT-MDT Spectrum Instruments, who specialise in the manufacture of hardware for nanoscale analysis. With the new hardware arriving in the lab, and shipping with an updated control software, it was decided that this piece of hardware should be integrated with the Qudi lab control software. This undertaking proved challenging but ultimately successful, with full control of the stage now enabled via Qudi. The primary source of difficulty during this integration project stemmed from the sending of commands and the receiving of data from the instrument itself.

In this specific instance, communication with the stage was required to be sent via the instrument's own control software, Nova Px, using the C programming language. Then, once a command sequence had been received, that sequence (or 'command packet') would be executed in NT-MDTs own proprietary programming language Nova Power Script. This process is represented in Figure 4.2, and the specific driving code is located in Appendix B.

4.4 Scanner Motor Interfuse for Stage Integration

When conducting a confocal scan Qudis confocal logic modules expects the photon counts to be returned line-by-line, and for these counts to be correlated with the position of the scanning stage — building the two-dimensional confocal image we are familiar with. This is a result of the influence on the original designers by a traditionally used piece of lab infrastructure — a National Instruments (NI) card. NI cards are able to communicate with both piezo-electric stages that can take voltage inputs (which then drive the position of the stage) and, at the same time, collect a TTL signal from a photon detector (such as an APD). Moreover, NI cards are built with their own hardware clock — enabling hardware level time synchronisation. This feature allows the NI card to easily return the requested list of position-correlated count values to the confocal logic module.

In order to sidestep this hurdle we design a Qudi 'interfuse' module to emulate the previous hardware . The new 'scanner motor interfuse' that emulates the previous method by itself communication with the stage and the photon counting hardware separately, correlating position the stage position with the counts values, and then returning the 'confocal line' to the confocal logic module — negating the need to hardware-level time synchronisation. Programmatically, this is achieved by iterating over positions on the requested line, then collecting photon counts at that position for some present duration of time. The functional code that achieves this can be found in Appendix C.

This method has the advantage of simplicity in experiment construction — hardware selection is no longer intertwined with the need for a NI card with on-board time synchronisation. However, the downside of this method is the waiting time required for hardware communication, typically over USB. The USB communication protocol is significantly slower than setting stage positions with / collecting analogue signals, and with the 'scan line' action requiring movement to each individual pixel along the path, and ultimately the entire two-dimensional scan range, the time required to complete a scan is increased by at least one order of magnitude. There does however exist the potential for the speed of this process to be improved by methods such as moving directly from the first pixel in the line to the last and interpolating the string of received photon counts over the path into the individual pixel bins.

Through this implementation we are now able to perform fluorescence microscopy with this new stage utilising Qudi. The NT-MDT stage provides a slow, but ultra-stable, platform for fluorescence confocal microscopy, which we have since demonstrated, see Figure 4.3.

4.5 RHEA Spectrograph

The Replicable High-resolution Exoplanet and Astroseismology (RHEA) spectrograph is an ultra-compact fibre-fed échelle spectrograph designed both to locate extra-solar planets, and to simultaneously gather information about those planets host stars [164]. The instrument has been integral in enabling our experiments on Raman-based nanodiamond thermometry — soon described in Chapter 5. It is appropriate that we record here the details of the non-trivial data extraction process implemented.

4.5.1 Instrument Description

The optical design of the spectrograph is only briefly described below, as its construction was undertaken by a separate research team. The instrument features a unique double-pass configuration with a custom made cross-disperser prism to disperse the input light over 42 orders (échelles) and onto a CCD camera. A comprehensive overview of the instrument and its original goals can be found in the literature [164–167]. The physical dimensions of the instrument are $41 \times 30 \times 27$ cm, proving compact in comparison with a traditional spectrometer.

4.5.2 Instrument Calibration

Calibration of this instrument was required prior to its use and integration with our lab systems. This process is now streamlined, however, when the instrument was received we did not have access to any previous methods of calibration or operation.

(a)

(b)

(c)
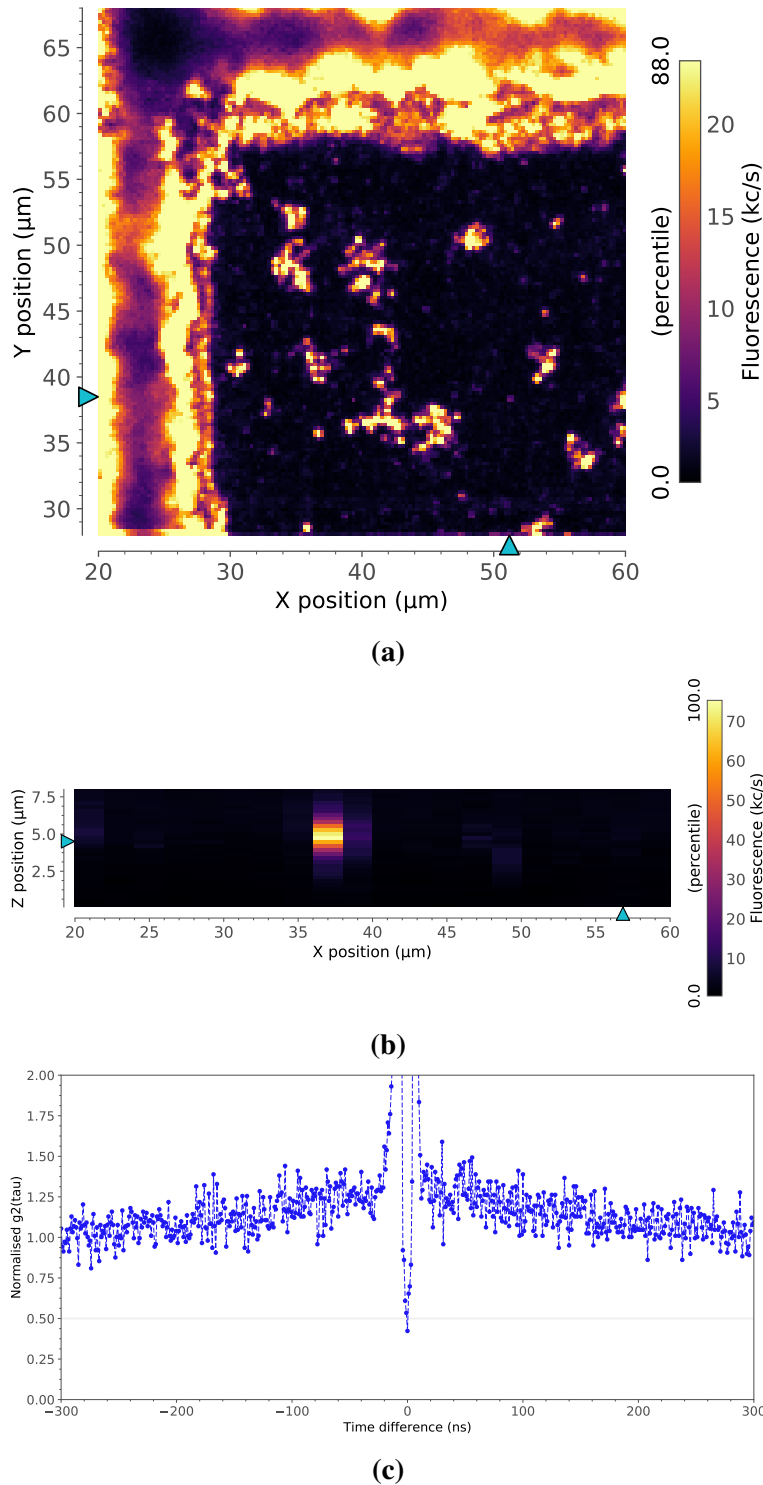
Figure 4.3: Confocal scan undertaken with the integrated NT-MDT piezoelectric stage via the scanner motor interfuse. **(a)** The above scan demonstrates the capability of this confocal platform — a $40 \times 40\,\mu m$ area has been scanned of a ND sample. The coverslip used for this scan contains etched grids, the trench of one of which can be observed in the confocal image. **(b)** An xz confocal scan of the sample, used to precisely locate the confocal xy plane where the ND material rests on the coverslip. **(c)** Detection efficiency has been optimised to the threshold where NDs containing single NV centres can be imaged, as confirmed by a $g^{(2)}(\tau)$ correlation measurement. The extreme levels of photon bunching to each side of the dip can be attributed to crosstalk between the APDs.

4.6   Version Control Branches for Experiment Coordination

Previously we have introduced the concept of version control as one of the aspects that enables wider adoption of the Qudi software package. On one level Git provides a tool to facilitate the distributed open-source development of this project. However, it also provides a means for coordinating experiment implementations locally within a research group — which is not within the scope of the broader Qudi project. In the process of developing and integrating the novel hardware covered above, we have established a set of operating procedures to use git for this enhancement of local experiments. Here we construct a demonstration of how good version control practices can improve the efficiency of code development in the context of a research lab.

Let us begin our demonstration with a fully working copy of the Qudi lab control code. This code is complete and tested, and is located on what is typically referred to as the *master* branch, Figure 4.4a. All code that is on the master branch should always be stable and ready for a new user to install and to run their experiments. For the purpose of this demonstration let us say that the lab received a new laser which we wish to integrate with the lab-control software. Because we do not want to place incomplete code onto the master branch, we would then start to develop this code on what is known as a 'feature' branch, Figure 4.4b. On feature branches we can build and test code happily without fear of breaking old code that is essential for other users.

Now with our laser only partially integrated with the main code let us pretend that we would like to start using the laser on an experiment immediately. In this case, we would now create a new 'experiment' branch of the code, Figure 4.4c. The origin of this branch should be the master branch, and then we merge the incomplete laser code into this branch.

After some time lets say that while running our new experiment we find that some feature of the laser is not functioning as expected — likely due to our rushed attempt at its integration. In such a circumstance we should develop the fix for this code on the laser feature branch — to maintain all development for this piece of hardware on its own branch. The feature would then be re-merged into the experiment branch, Figure 4.4d, and this process can be repeated as required, Figure 4.4e.

We maintain this separation because it is possible, and likely, that we have multiple new pieces of hardware which we are developing integration for in parallel — each on their own feature branches. To develop these on top of one another, on a single branch, would quickly grow out of control — which is not a scalable solution.

With all development of the hardware/software interfacing code complete, this feature can then be sent back into the master branch, ready for any user to utilise for their own experiments, Figure 4.4f.
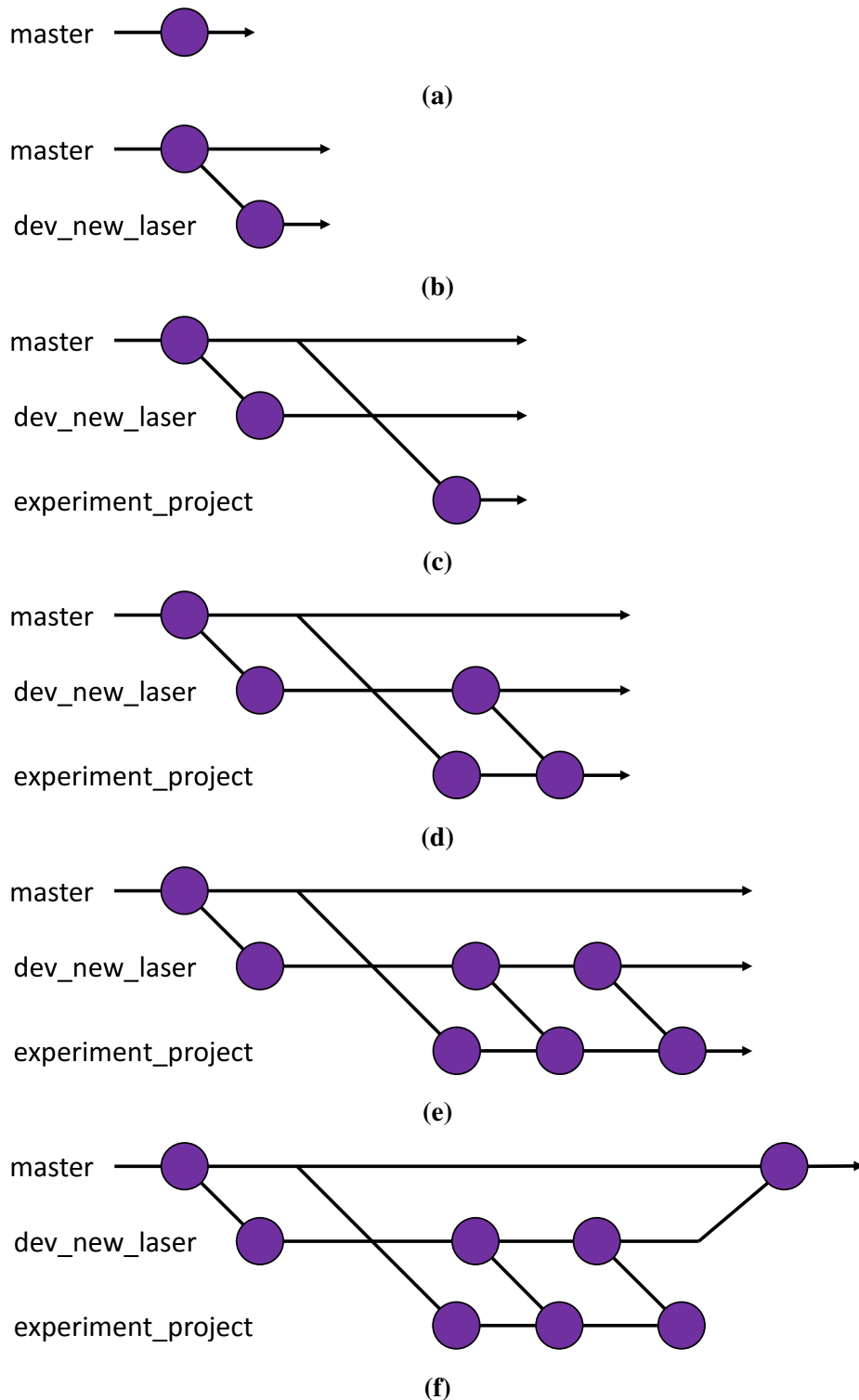
Figure 4.4: Demonstration of the use of a version control system. Purple nodes represent code commits along the three example branches; *master*, *dev_new_laser*, and *experiment_project*. Integration of new hardware is maintained on its own feature branch, can be merged into experiment branches for use, and when development is complete can be merged back into the master branch for implementation by other users.

5

Nanodiamond Thermometry

"To achieve great things, two things are needed; a plan, and not quite enough time."

Leonard Bernstein

To investigate the effects of temperature on nanodiamonds exhibiting superradiant behaviour we need to develop a reliable method for measuring the local temperature of nanoscale systems. Raman spectroscopy is proposed as a technique to measure the temperature of each individual ND, and which is independent of the colour centres it hosts. This allows us to determine the temperature of individual nanodiamond particles at a spatial scale smaller than visible or infrared wavelengths. Some promising work in this area was realised in our group through a Masters project focused on utilising NDs as nanoscale thermometers for integrated transistor circuits [14]. We build on these results and extend them through the process of a highly-systematic exploration of the parameter space, and by employing the novel ultra-high resolution spectrometer that has been presented in Chapter 4.

5.1 Background

Raman spectroscopy is a well-established method for material characterisation. Enhanced by the invention of the laser, it has found application in a large range of disciplines spanning from biology to geology, chemistry and, of-course, physics [168–171]. The Raman[i] scattering process was first observed in 1928 whereby sunlight was seen to be red-shifted upon passing through organic liquids [172]. We now know that this effect originates from the interaction of the light-field (photons) with atomic vibrations (phonons) in the material. Scattered photons that are red-shifted with respect to the excitation source are referred to as Stokes scattered photons, where the difference in energy equates to that of the phonon(s) created, as shown in Figure 5.1. Conversely, photons can be blue-shifted through the absorption of energy from phonons. This effect is much less efficient, and these photons are know as

anti-Stokes scattered photons.

5.1.1   A Classical Approach

To present a formal understanding of this effect we discuss a simple example adapted from the literature [173]. Consider a diatomic molecule isolated from its surroundings and with negligible rotation. Initially, we consider the diatomic molecule as being at rest. In the presence of a light field of frequency v_0, a dipole moment $\vec{p}$ is induced. The dipole moment is proportional to both the electric field, $\vec{E}$, and the polarisability of the molecule, α:

$$\vec{p} = \alpha \vec{E} \tag{5.1}$$

The dipole moment oscillates at the same frequency v_0 of the electric field:

$$p(t) = \alpha E_0 \cos\left(2\pi v_0 t\right) \tag{5.2}$$

If the atoms of the diatomic molecule are also vibrating at some frequency ω_p, then the polarisability of the molecule is also oscillating as a function of the internuclear distance r. To incorporate this into the model we expand the polarisability as a power series of the internuclear distance:

$$\alpha\left(r\right) = \alpha\left(r_0\right) + \frac{d\alpha}{dr}\left(r - r_0\right) + \text{higher order terms} \tag{5.3}$$

We can then write the internuclear distance $r - r_0$ in its time-dependent form:

$$r - r_0 = \cos\left(2\pi\omega_p t\right) \tag{5.4}$$

The expression for the time-dependent polarisability becomes:

$$p(t) = \left[\alpha\left(r_0\right) + \frac{d\alpha}{dr}\cos\left(2\pi\omega_p t\right)\right]\alpha E_0 \cos\left(2\pi v_0 t\right) \tag{5.5}$$

which can be re-written through the application of a trigonometric identity to become:

$$p(t) = \alpha\left(R_0\right) E_0 \cos\left(2\pi v_0 t\right) + \frac{1}{2}\frac{d\alpha}{dr}E_0 \left(\cos\left[2\pi\left(v_0 + \omega_p\right)t\right] + \cos\left[2\pi\left(v_0 - \omega_p\right)t\right]\right) \tag{5.6}$$

This is where we find the signature indication of the Stokes and anti-Stokes photons, at $v_0 - \omega_p$ and $v_0 + \omega_p$ respectively. This is the first order Raman effect, and it follows that, with decreasing intensity, Raman lines can also be observed at $\left(v_0 \pm 2\omega_p\right)$, $\left(v_0 \pm 3\omega_p\right)$, etc. from the higher order terms of the power expansion.

In the context of solid-state materials these vibrations of the lattice are known as phonons — the quantised version of vibrational modes. To enhance clarity, we adopt the terminology here where photon frequencies will be denoted as v's, and phonon frequencies as ω's. Also in solids the atoms are constrained within the matrix of the lattice and so we do not need to consider the rotations of the "molecules" (just as we did not consider them in the example above).

This classical model is simple and intuitive, however, it cannot provide us with a complete understanding of the Raman scattering method. For instance, in this classical picture we would expect the intensities of the Stokes and anti-Stokes scattered photons to be matching, but this is not the case. To further comprehend the process, let us now take a quantum approach.

---

[i]Nobel Prize in Physics 1930 "for his work on the scattering of light and for the discovery of the effect named after him."

5.1.2   A Quantum Approach

This description of Raman scattering arises from an intuitive model. We picture some system with a combination of vibrational and optical transitions, such as the ones depicted in Figure 5.1. In the case of Stokes scattering a photon of energy $h\nu_0$ excites an electron from the ground to the "virtual" excited state. The electron relaxes, but it does so into a vibrational energy level of the ground state, itself at some energy $h\omega_p$. Therefore, the photon(s) released by the system must be of energy $h\left(\nu_0 - \omega_p\right)$ — now red-shifted from the original pump frequency. Conversely, the process whereby a photon (of energy $h\nu_0$) excites an electron out of some vibrational energy level (with energy $h\omega_p$) and the system relaxes into its ground state via the emission of a photon with energy $h\left(\nu_0 + \omega_p\right)$ is known as anti-Stokes scattering.

It follows that we can use the Boltzmann factor (the phonon occupation probabilities) to calculate the intensity ratio between the Stokes and anti-Stokes shifted photons. It is also important to include a factor to account for the ratio of the density of optical modes (the optical density of states). This gives rise to the relation

$$\frac{I_{\text{anti-Stokes}}}{I_{\text{Stokes}}} = \left(\frac{\nu_{\text{AS}}}{\nu_{\text{S}}}\right)^3 e^{\frac{-h\omega_p}{k_B T}} \tag{5.7}$$

where ν_{AS} and ν_{S} are the energies of anti-Stokes- and Stokes-shifted photons respectively. Often in the literature this optical density of states factor is raised to the power of 4. However, as we are counting photons and not measuring energies (recall $E = \hbar\omega$) our factor is appropriately only raised to the power of 3 (as per [174]).

In diamond material it is known that $\omega_p = 1332\,\text{cm}^{-1} = 165\,\text{meV}$ [175] which is quite large due to a higher lattice oscillation frequency (phonons) than other crystals. This property contributed to diamond being one of the first materials to have its Raman spectra investigated, as early as 1930 [176]. At room-temperature $T = 298.15\,\text{K}$ (25 °C) the intensity ratio would be $I_{\text{anti-Stokes}}/I_{\text{Stokes}} = 2.47 \times 10^{-3}$.

This ratio changes with temperature and thus becomes a key metric for our measurements.

5.1.3   Raman Shift as a Function of Temperature

We can also look at the frequency shift of the Stokes and anti-Stokes lines with temperature and adopt this as a secondary metric for our investigation. The expected shift of the Raman line as a function of temperature in solid-state materials was first described as a 3-phonon decay process known as the Klemens model after the author who established it [177]. In this model, the optical phonon created by the Raman scattering (with energy $\hbar\omega_p$) is considered to decay into two acoustic phonons of energy $\hbar\omega_p/2$ and opposite momentum. Klemens used perturbation theory to describe the Raman shift as a function of temperature with the form

$$\Omega\left(T\right) = \omega_0 + A\left(\frac{2}{e^{\frac{\hbar\omega_0}{2k_B T}} - 1}\right) \tag{5.8}$$

where ω_0 is the Raman shift at $0\,\text{K}$ ($\omega_0 = \omega_p|_{T=0}$). The A coefficient characterises this Klemens channel and depends on the solid material.

Later, the temperature dependence of the Raman line in silicon was measured and at high temperatures, where $T \sim k_B/\Delta E$, the data were found to deviate from the Klemens model [174]. The author, Balkanski, showed that higher-order terms are required to fit to the
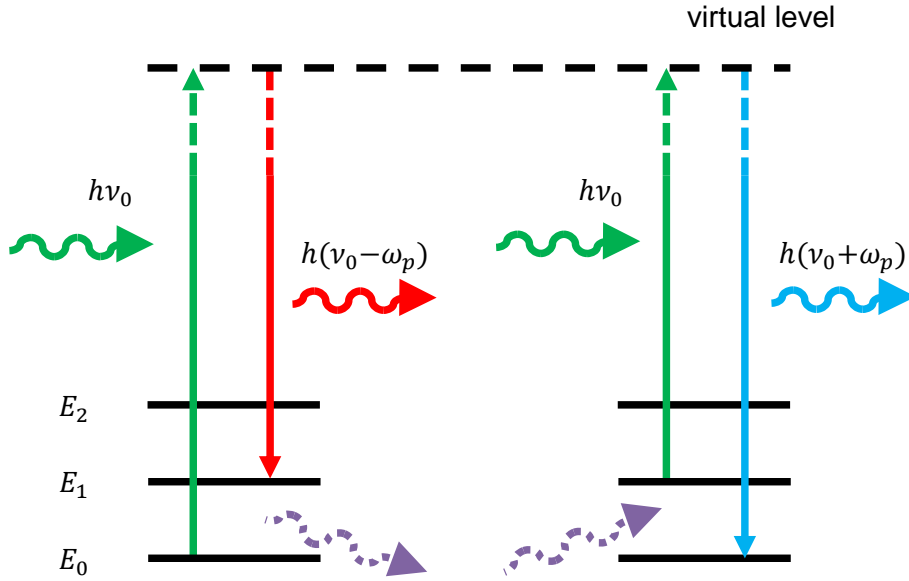
Figure 5.1: Diagrammatic representation of Stokes and anti-Stokes scattered photons. In the case of Stokes scattering (left), a photon of energy $h\nu_0$ excites an electron from the ground to excited state. Then, the electron relaxes, but into a vibrational energy level of the ground state, itself of some energy $h\omega_p$. Therefore, the photon released by the system must be of energy $h\left(\nu_0 - \omega_p\right)$ — now red-shifted from the original pump frequency. Conversely, the process whereby a photon (of energy $h\nu_0$) excites an electron out of some vibrational energy level (with energy $h\omega_p$), followed by the system relaxing into its ground state via the emission of a photon with energy $h\left(\nu_0 + \omega_p\right)$ is known as anti-Stokes scattering (right).

recorded data. The Klemens model was thus modified to include a 4-phonon decay process, in which the optical phonon may decay into three acoustic phonons each of energy $\hbar\omega_p/3$. This leads to an additional term in the temperature dependence of the Raman shift, which takes the form

$$\Omega\left(T\right) = \omega_0 + A\left(\frac{2}{e^{\frac{\hbar\omega_0}{2k_B T}} - 1}\right) + B\left(\frac{3}{\left(e^{\left(\frac{\hbar\omega_0}{3k_B T}\right)}\right)^2 - 1} + \frac{3}{e^{\frac{\hbar\omega_0}{3k_B T}} - 1}\right) \quad (5.9)$$

where the A coefficient describes the Klemens decay channel and the B coefficient describes the higher order contribution.

Data on the Raman line position as a function of temperature has been collected from bulk samples in many studies [178–182]. Data from Liu et al [182] is considered as the most accurate data set due to the authors collection methods. Furthermore, in this paper data appears accurately fitted with the 3-phonon decay Klemens model, Equation 5.8. Not including the higher-order terms in the fitting function seems justified in Liu et al's study, as the temperatures at which the Raman shift is measured falls below the Debye temperature for diamond, $T_D \sim 2200\,\text{K}$ [183]. Above the Debye temperature factors contributing to both the Raman line position and linewidth vary at different rates, and fitting of the higher-order corrected model, Equation 5.9, is necessary [174].

In summary, this method of fitting the Klemens model, without higher-order terms, appears consistent throughout the literature for group IV semiconductors (carbon, silicon, and germanium). For silicon at more elevated temperatures Balkanski's addition of the higher-order terms is required. As yet, this higher order correction has not been required when fitting

to experiments in diamond, as conducted measurements have not reached the $T \sim k_B/\Delta E$ threshold (which for diamond lies higher than that of the other group IV semiconductor elements due to the high phonon energy in diamond).

In this thesis, we focus solely on the position of the Stokes scattered photons as opposed to their linewidth. Previous studies [184] primarily focus on the linewidth of the Stokes scattered photons, however, in nanodiamond materials we know that the linewidth can be altered as a result of numerous factors including defects within the lattice [184–186] and phonon confinement effects [187–190], either of which can generate inhomogeneous linewidth broadening of the Raman signal. It is for these reasons that we choose to investigate the line position, as it is easier to measure shifts rather than changes in linewidths. Furthermore, the advantage of using Raman measurements over measurements on the properties of the NV centre is that whilst spatial resolution is lost (possibly), measurement sensitivity is gained. The body of work previously conducted in our lab was ultimately unsuccessful due to the spectral instability of the laser utilised and the presence of results that did not follow the expected trend [14].

5.2 Measurements

A key factor contributing to our renewed interest in this project was the recent acquisition of an ultra-high resolution spectrograph able to monitor wavelengths continuously from ~ 490–770 nm. The unique abilities of the RHEA spectrograph, described previously in § 4.5, has been integral in enabling us to continue our investigations into nanodiamond Raman thermometry. With the powerful capability of being able to image the Stokes and anti-Stokes scattered photons and the laser line simultaneously, without either loss of resolution or narrowing of the range of wavelengths imaged, we commence our investigations.

5.2.1 Experiment Architecture

To conduct this experiment we utilise a lab-built confocal microscope as our primary platform. A schematic representation of the experimental setup is presented in Figure 5.2. As we will be heating the sample mount we select an air objective (UMPlanFl 100x/0.90 BD; Olympus) — sacrificing collection efficiency for a physical air-gap between to sample and the objective to avoid potential damage via radiative heat transfer.

For our excitation source we employ a $\lambda = 532$ nm CW laser (OBIS 532-150 LS; Coherent), operating within the power range of 1–160 mW. To separate the excitation and collection paths we do not use a dichroic mirror but rather place an uncoated 90:10 beamsplitter in the configuration such that we sacrifice 90% of our excitation power to gain 90% transmission of our collection path. We then install 533 nm notch filter (17 nm FWHM, NF533-17; Thorlabs) at the entry to the collection fibre to reduce the throughput of the excitation laser. For photon detection we employ a single avalanche photodiode (APD) (SPCM-AQR-14; Perkin Elmer), with its signal subsequently passed to a correlator (Time Tagger 20; Swabian Instruments) for photon counting.

To control the temperature of the sample we assembled a lab-built substrate heater made from an aluminium frame, an electrical resistor, and a power supply unit (EA-PS 2342-10 B; Elektro-Automatik). The power supply drives current through the resistor, subsequently heating the aluminium frame which the substrate thermalises with. Using the aluminium frame as a heat mediator allows the thermal load to be evenly distributed across the substrate.
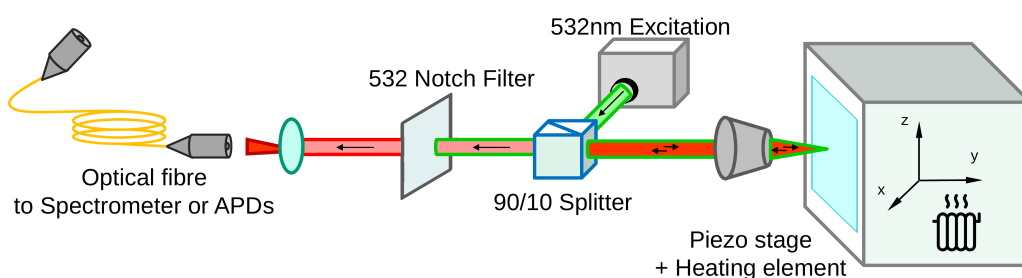
Figure 5.2: Experiment architecture for the investigation of the effects of temperature an Raman scattering from individual nanodiamond particles. A λ = 532 nm CW laser is incident upon a 90:10 beamsplitter such that we sacrifice 90% of our excitation power to gain 90% transmission of our collection path. A notch filter then removes the excitation light from the collection path, and the emission is coupled into a single-mode fibre. An electronically-triggerable flip-mirror placed after the notch filter directs the collection path into separate fibres which are subsequently coupled to either the APD or the spectrograph.

5.2.2   Sample Preparation

Measurements have been conducted on (250 ± 20) nm nanodiamond sample (ND-250; LuciGem), which arrives from the manufacturer suspended in water (1 mg/mL concentration). The sample was prepared on a 170 μm think BK7 glass coverslip (BB022022A1; Menzel-Glaser), which was itself prepared by rinsing with acetone (C_3H_6O, purity $\geq$ 99.5; Sigma-Aldrich). The nanodiamond sample was sonicated for 30 minutes to de-aggregate the individual NDs in the solution. A droplet of solution ($\sim$ 10 μL) was then placed on the coverslip and left to evaporate naturally. As the solution evaporates the meniscus deposits the NDs on the coverslip with decreasing density as the droplet shrinks while drying. This can simply be thought of as leaving behind a stain from a coffee mug on a piece of paper — it deposits a ring of coffee particles. The difference here being that the 'coffee cup' is the droplet, and it shrinks continuously as the droplet evaporates. This method is less sophisticated than other sample deposition methods such as spin coating or the use of a nebulizer, but it has the advantage of creating regions of decreasing ND density — allowing the user to move to either less dense or more dense regions without changing the prepared coverslips.

5.2.3   Experimental Methods

The premise of the experiment is now simple: record the spectrum of a set of NDs at various substrate temperatures. We also recorded multiple spectrums of each ND at each temperature setting while increasing the intensity of the excitation laser power in order to assess the speed at which data could be acquired. The largest challenge in data acquisition was obtaining clear signal-to-noise for the weak anti-Stokes line.

With all lab instruments required for this experiment integrated with a common lab control system (see Chapter 4) we programmatically structured these tasks. In the control code we used nested *for* loops that iterate over the parameter space, and included delays to ensure the entire sample reached thermal equilibrium at each temperature increment before data acquisition. This can be observed below where a snippet of the control code has been presented. Lines 1–9 and 47–49 control the initialisation and de-initialisation respectively of the required hardware In the former instance, the laser and power supply are set to 'on' and the detection path set 'to the APD.' In the latter, the laser and power supply are simply set to

'off.' The list of currents and laser powers over which to iterate are defined in lines 7 and 20 respectively, and the command to expose the spectrograph CCD is found on line 28. Commands on lines 36 and 44 push notifications to the lab users phones upon completion of the measurement, or upon a failure whereby the experiment ceases to run. The measurements presented in this thesis alone represent over 100 hours of unsupervised, semi-autonomous data collection.

```python
time_then = time.time()

obis.set_power(10e-3)
obis.on()
set_detector_apd(True)
powersupply.set_output_on(on=True, node=0)
currents = np.linspace(0, 0.4, 11)

push = True

try:
    for current in currents:
        powersupply.set_current(current, node=0)

        if current != 0:
            for j in range(20):
                reop_crosshair(10e-3)
                time.sleep(30)

        for spec_power in np.linspace(35, 165, 11):
            reop_crosshair(10e-3)

            obis.set_power(spec_power*1e-3)
            time.sleep(10)

            exposure = 150 * 150 / spec_power

            for i in [exposure]:
                init_camera_get_spectrum(i, poiname='ND_X', power=spec_power, current=
                    current)

    time_now = time.time()

    run_duration = time_now - time_then

    if push == True:
        push_clients('Measurement completed in {:.2f} hours'.format(run_duration/3600))

except:
    time_now = time.time()
    run_duration = time_now - time_then
    e = traceback.format_exc()
    print(e)
    if push == True:
        push_clients('Measurement failed after {:.2f} hours. {}'.format(run_duration/3600,
            e))


obis.off()
powersupply.set_current(0, node=0)
powersupply.set_output_off(off=True, node=0)
```

5.2.4   Data Processing

We first use our methods for extracting spectral data from the RHEA spectrograph (§ 4.5), then fit Lorentzians to the Stokes peak, the anti-Stokes peak, and the laser line (which is weak due to our filters, § 5.2.1). Diamond Raman lines have previously been fit with Voigt functions to account for the instrument resolution being broad relative to the Raman linewidth [182], however, here the instrument resolution is much finer than the measured linewidth and

a Lorentzian was found to be a good fit to our data. In the immediate wavelength range of the anti-Stokes line the RHEA spectrograph resolution is ~ 374 pixels/nm, around the laser line ~ 349 pixels/nm, and around the Stokes line ~ 322 pixels/nm (with 532 nm excitation), and therefore we find no need to deconvolve the Lorentzian signals with what would be the Gaussian response of a spectrograph unable to sample with such a resolution.

When conducting these fits we use conventional least-squares minimisation for optimisation on the Stokes and anti-Stokes peaks, and in the case of fitting to the laser peak we use the Powell fitting method [191] which we have found to produce more consistent identification of the laser peak position for weak signals. The parameters of the fitted peaks (location and amplitude) are then used to analyse our data. The Raman shift (and the 'anti-Raman' shift) are determined from these parameters with the below basic calculation:

$$\text{Raman shift} \, [\text{cm}^{-1}] = 10^7 \left(\frac{1}{\lambda_{\text{laser}} \, [\text{nm}]} - \frac{1}{\lambda_{\text{Raman line}} \, [\text{nm}]} \right) \tag{5.10}$$

When conducting any analysis of the intensity ratio of the Stokes and anti-Stokes lines we define the peak intensities to be the area under the Lorentzian curve. This has the form

$$I = \int_a^b \frac{2A}{\pi} \frac{\sigma}{4 \left(x - \mu \right)^2 + \sigma^2} dx \tag{5.11}$$

$$= \frac{A}{\pi} \left[\tan^{-1} \left(\frac{2 \left(b - \mu \right)}{\sigma} \right) - \tan^{-1} \left(\frac{2 \left(a - \mu \right)}{\sigma} \right) \right] \tag{5.12}$$

where μ is the peak position, $2 \sqrt{2 \ln 2} \sigma$ is the FWHM, and a and b are the integration limits chosen to be $\mu - 0.5$ and $\mu + 0.5$ respectively.

Corrected Anti-Stokes / Stokes Ratio

We have seen in Equation 5.7 that the intensity ratio between the anti-Stokes and Stokes lines is strongly correlated with temperature. As such, this serves as a good measurement for extraction of temperature information from the data. However, the accuracy of this metric is strongly dependent upon the amplitude calibration of our spectrometer, outlined in § 4.5.2.

Before analysing any data we first perform a slight alteration of the anti-Stokes / Stokes ratio description (Equation 5.7) to account for a finer amplitude correction factor of the RHEA spectrograph (see § 4.5.2). We modify the equation by the inclusion of such a factor, α:

$$\frac{I_{\text{anti-Stokes}}}{I_{\text{Stokes}}} = \alpha \left(\frac{\nu_{\text{AS}}}{\nu_{\text{S}}} \right)^3 e^{\frac{-\hbar \omega_p}{k_B T}} \tag{5.13}$$

To determine the instrument calibration factor α we measure the anti-Stokes / Stokes ratio generated by bulk diamond (Element 6) at room-temperature (25 °C). The use of a bulk sample was decided to negate any unexpected effects arising from the use of nanodiamond material, such as stress and strain within the crystal lattice. To gather a clean anti-Stokes signal (recall from § 5.1.2 that the efficiency of the Stokes scattering process is dominant over the anti-Stokes scattering process) a total of 650, 2 minute exposures were conducted with the aid of our heavily automated lab control systems. At this temperature, from the Boltzmann distribution we expect the anti-Stokes / Stokes ratio to be 2.47×10^{-3} (from § 5.1.2). Our observed ratio on the instrument was 3.13×0^{-4}, and therefore our α multiplicative factor is
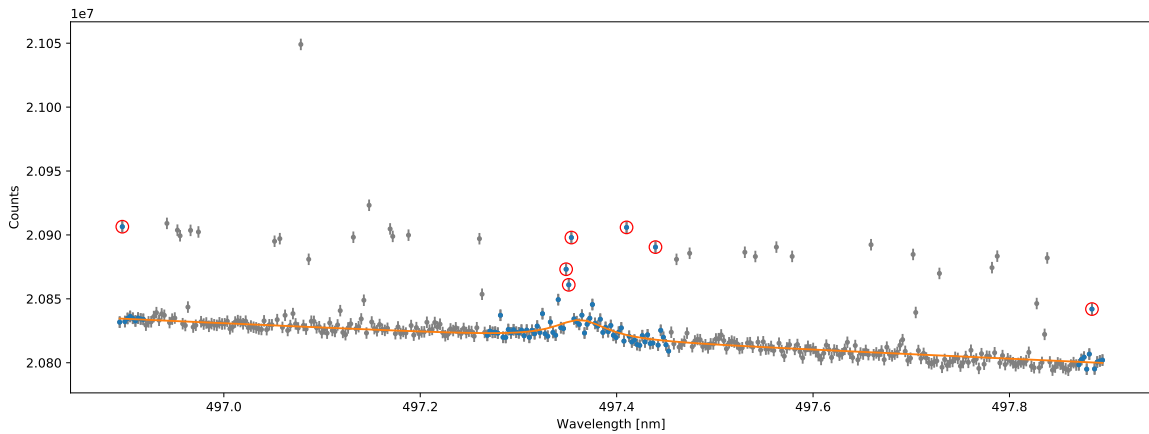
Figure 5.3: Maximum likelihood fit of the anti-Stokes signal by Bayesian marginalisation.
We use a Bayesian fitting algorithm, described briefly in Appendix D, to compute the maximum
likelihood fit and extract the Lorentzian fit parameters (position μ, width σ, and amplitude A)
of the anti-Stokes peak. The maximum likelihood fit is shown in orange. Blue data points are
included in the fitting algorithm whereas grey data points have been excluded due to computa-
tional intensity. Data points circled in red are been computed by the algorithm to more probably
be noise than to be genuine data. Error bars are chosen to be a constant that is $\sim \sqrt{N}$, where N
is the number of counts.

$2.47 \times 10^{-3}/3.13 \times 0^{-4} = 7.96$. Here we note for future reference that the Raman shift in this
bulk diamond sample is $1333.007\,\mathrm{cm}^{-1}$. To ensure the highest level of fitting accuracy, as
this determination of α influences all anti-Stokes / Stokes ratios, we implemented a Bayesian
fitting algorithm inspired by [192, 193]. The technique is briefly described in Appendix D.

5.2.5   Stokes Signal Raman Shifts

Spectra were recorded for NDs at various hotplate temperatures and laser powers (note
that each data set has been collected from different ND samples). The observed behaviour
broadly fall into three categories; NDs showing effects from heating the substrate, NDs af-
fected by increasing the incident laser power, and NDs with apparent effects from a combi-
nation of these factors. These are outlined hereafter.

Substrate Induced Heating

The fitted peaks are presented in Figure 5.4a. In these subplots two subsets of data can
be visualised, which originate from separate échelles recorded on the RHEA spectrograph
CCD. Upon systematic analysis of the measurement results we perceive the following:

- **Raman line shift proportional to substrate heating.** We observe a shift of the Stokes
  line of $\sim -0.4\,\mathrm{cm}^{-1}$ when the heater current is increased, corresponding to a tempera-
  ture increase from room-temperature to $70\,^{\circ}\mathrm{C}$. This data is presented along the x-axis
  in Figure 5.4b.

- **Absence of Raman line shifting with laser power.** No discernible shift of the Raman
  line can be observed when the laser power is increased. This data presented along the
  y-axis in Figure 5.4b.

(a)

(b)
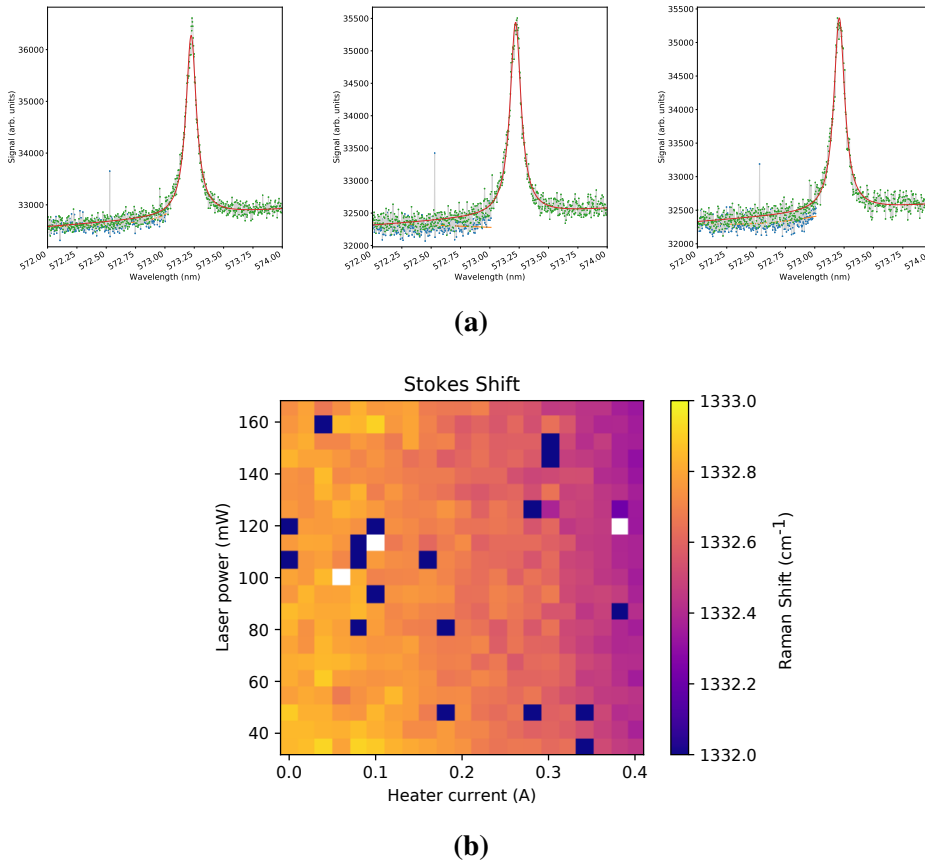
Figure 5.4: Data extraction and fitting when heating the sample substrate. (a) The recorded Raman line, where data subsets originate from separate échelles recorded on the RHEA spectrograph CCD, extracted via the implementation of our own data processing methods previously presented in § 4.5.2. **(b)** The Stokes shift as a function of both heater current and laser power. We only see a trend across the x-axis ($\sim -0.4\,\mathrm{cm}^{-1}$), corresponding to increasing heater current (temperature shift over the range $T = 25\,°\mathrm{C}$ ($298.15\,\mathrm{K}$) to $70\,°\mathrm{C}$ ($343.15\,\mathrm{K}$)). We observe no noticeable shift with the laser power along the y-axis.

- **Inability to determine the anti-Stokes/Stokes ratio.** Over this temperature range we are unable to distinguish the anti-Stokes signal from the noise of the measurement. This is a combination of the expected small anti-Stokes / Stokes ratio in this temperature range and the shot noise of the instrument.

Optically Induced Heating

In some nanodiamonds the effect of substrate heating is negligible compared to the optically-induced heating. This occurs for those nanodiamonds which have poor thermal contact with the substrate, and are therefore heated by the laser beam. A strong shift — up to $\sim -3\,\mathrm{cm}^{-1}$ — of the Raman line can be triggered by increasing the laser power. The fitted peaks are presented again in Figure 5.5a where the much more prominent shift can be seen unaided. From this data set we make the following observations:

- **No distinguishable Raman line shift with substrate heating.** As evident along the x-axis in Figure 5.5b we do not observe any change in the position of the Raman line

(a)

(b)
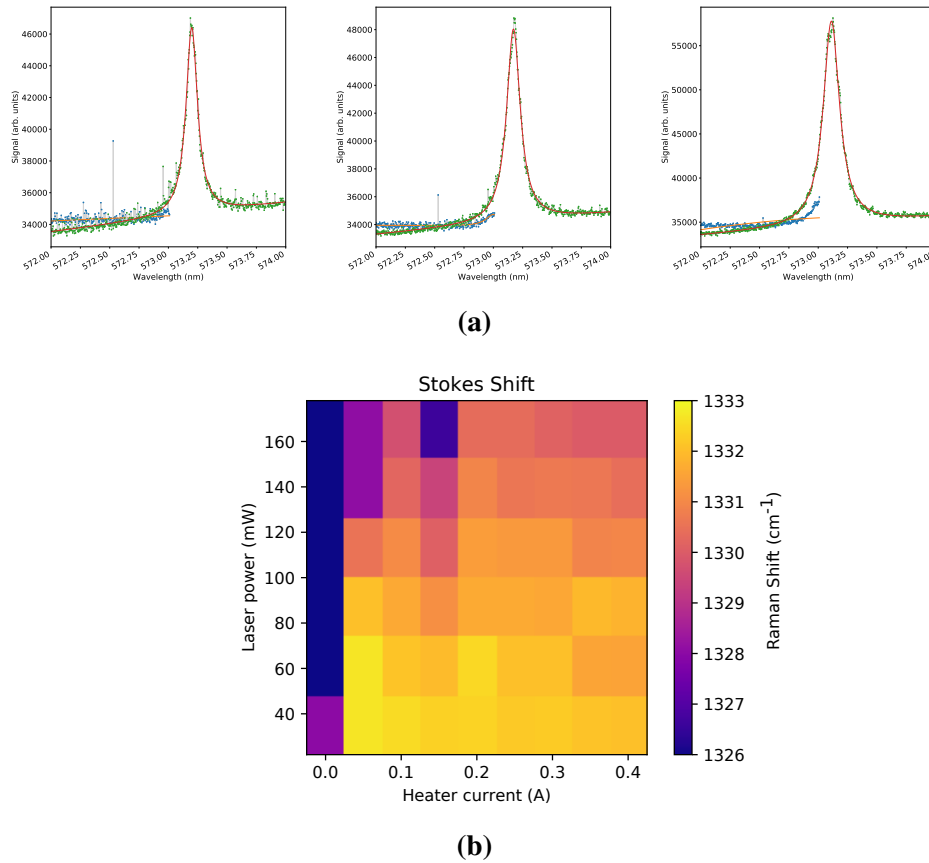
Figure 5.5: Data extraction and fitting showing strong evidence of heating as a result of increasing the laser power. (a) The Stokes scattered photons (Raman line), where data subsets originate from separate échelles recorded on the RHEA spectrograph CCD. **(b)** The Stokes shift as a function of both heater current and laser power. We observe no noticeable shift along the x-axis (a function of heater current), but see evidence of a strong trend across the y-axis ($\sim -3\,\mathrm{cm}^{-1}$), corresponding to increasing laser power.

as the heater current is increased — corresponding to a change from room-temperature $T = 25\,°\mathrm{C}$ (298.15 K) to $70\,°\mathrm{C}$ (343.15 K).

- **Strong Raman line shift with increasing laser power.** In this instance we see a strong ($\sim -3\,\mathrm{cm}^{-1}$) shift of the Raman line as the laser power is increased from 40–160 mW, presented along the y-axis in Figure 5.5b. That we would observe a shift of this magnitude was unexpected upon the commencement of this experiment.

- **Ability to determine the anti-Stokes/Stokes ratio.** In this data set we regained our ability to distinguish the anti-Stokes line. We attribute the re-acquisition of this ability to the anti-Stokes / Stokes ratio increasing with temperature, as per Equation 5.13.

Combinational Heating

In the previous two examples we see only evidence of either substrate heating (originating from us driving current through the attached heating element), or of optical heating (originating from the intensity of the incident laser). It is however possible that we observe a combination of these two effects, as is evident in the dataset that is next presented.

(a)

(b)
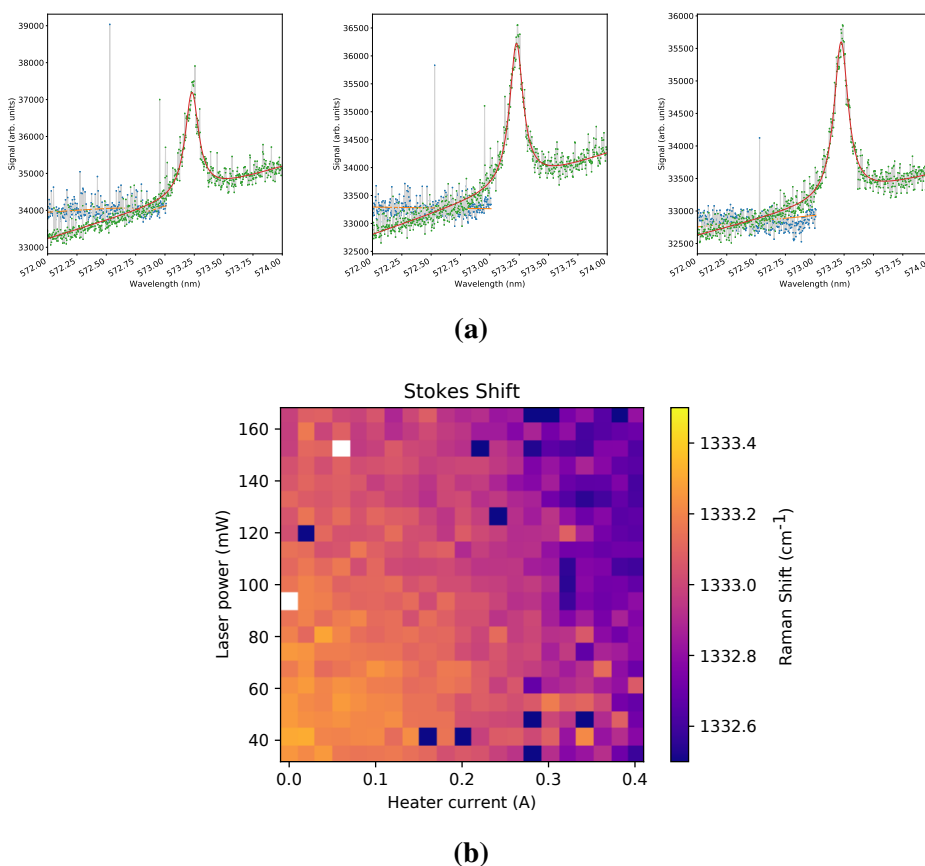
Figure 5.6: Data extraction and fitting showing combinational heating effects. **(a)** The recorded Raman line, where data subsets originate from separate échelles recorded on the RHEA spectrograph CCD. **(b)** The Stokes shift as a function of both heater current and laser power. We can observe trends in both the x- and y-axes, as both the heater current and laser power are increased.

- **Raman line shift proportional to substrate heating.** We again observe a shift of the Raman line as a result of heating the substrate, Figure 5.6b along the x-axis. This shift of $\sim -0.5\,\mathrm{cm}^{-1}$ is comparable with that of the first discussed ND (§ 5.2.5).

- **Less extreme shift of the Raman line with laser power.** Upon analysis of the data, Figure 5.6b along the y-axis, we observe a less extreme shift (than that of the previous ND discussed in § 5.2.5) of $\sim -0.1\,\mathrm{cm}^{-1}$.

- **Inability to distinguishing the anti-Stokes line from the noise.** Again, as in the case of the first discussed ND (§ 5.2.5), we are unable to distinguish the anti-Stokes line from the noise and subsequently cannot fit and extract data from this feature. With a comparably small Raman shift inducted by optical heating, as compared to § 5.2.5 above, we theorise that this level of heating is not sufficient to increase the anti-Stokes / Stokes ratio to a sufficient, detectable level.

Upon analysis of the data we find an interesting result with broad implications. It is apparent that there are two independent effects that contribute to the heating of our individual NDs: substrate induced heating from the 'hotplate' fused to the sample mount (expected), and optically, laser-induced heating. The presence of either of these is not particularly surprising, but it is the magnitude of the optically induced heating which is our most remarkable

observation as it shows a large variability of possible scenarios ranging from very good to very poor thermal contact with the substrate.

When we observe NDs that show no apparent heating from substrate temperature increases, but do show heating from the incident laser, we conclude that the NDs are in poor thermal contact with the substrate. Note that if a particular ND has highly graphitic surface that this would also induce thermal heating. These NDs weakly absorb heat from the substrate, and when they are illuminated by the laser they cannot disperse heat into the substrate at a sufficiently-fast rate. It is also in this case that we are able to distinguish the anti-Stokes lines from the noise and determine the anti-Stokes / Stokes ratio. It is important to note, again, that this analysis is dependent on how good or bad the thermal contact is between the ND and the substrate.

This finding has significant impact for all measurements conducted on ND systems whereby temperature could potentially influence the observed behaviour. Laser-induced heating of ND particles has been considered previously [194], however has not been characterised thoroughly. The investigated NDs contain NV colour centres, and off-resonant excitation of colour centres will lead to the excitation of many phonons in the crystal lattice and therefore to optical heating. It is plausible that NDs that are in poor thermal contact with the substrate and with off-resonant excitation of colour centres will experience the significant optical heating that we observe, § 5.2.5.

The effects of heating can also influence the spectra of colour centres in diamond [195–197]. For example, one recent paper observes an anomalously large linewidth in one of the twenty three NDs studied [193]. The authors of the paper speculate that the ND is in poor thermal contact with the cold-finger of their cryostat — resulting in the particular ND having a higher temperature than those which are in good thermal contact. We postulate that, because of its poor thermal contact, the ND in question would have experienced effects arising from laser-induced heating. In fact, all of the linewidths observed in the studied NDs are larger by greater-than-a-factor of five to those observed in bulk diamond material.

Conversely, in the case whereby a ND exhibits a temperature change (inferred by a shift in the Raman line position) only from increasing the substrate temperature, then we deem that ND is in good thermal contact with the substrate, §5.2.5. When this ND is exposed to 'high' laser powers ($\sim 100\,\mathrm{mW}$), any heating that would be induced is immediately distributed into the substrate which has a much greater thermal mass.

Some NDs showed heating under the combined influence of the hotplate and the incident laser, § 5.2.5. This condition requires the laser-induced heating to be coincidentally balanced with the substrate heating, which we found to be uncommon across the NDs surveyed. To gain a broad overview of our results, we next continue our analysis through interpretation of the collective dataset.

5.2.6   Anti-Stokes / Stokes Intensities

Hereafter we separate each individual measurement into three categories: measurements with the anti-Stokes peak distinguishable (and hence the temperature determinable from the anti-Stokes / Stokes ratio), measurements where the temperature is determinable by correlation with the heater current, and measurements where we cannot determine the temperature by either method. Binning the measurements by their Raman Shift into histograms, Figure 5.7, reveals that measurements in which the anti-Stokes peak is distinguishable also undergo a much more significant Raman shift when heated (shifting of the Stokes scattered

photons with increased temperature), Figure 5.7a. In the case of measurements where we can infer the temperature from the heater current we do not see extreme Raman shifts (Figure 5.7b), and a similar observation for those measurements where we cannot infer the temperature from either method (Figure 5.7c). This leads us to conclude that higher temperatures account for both the larger Raman shift and the increased anti-Stokes intensity.

This observation is to be expected. In the case of the NDs where the anti-Stokes signal can be observed, these are also the cases where we are observing laser-induced heating. The anti-Stokes / Stokes ratio is seen to change with laser power and the Raman line also shifts significantly (multiple wavenumbers). In the second case where NDs that undergo substrate heating, the temperature of the NDs is known from our calibration of the heating element. The hotplate temperature is insufficient to drive such a large shift of the Raman line and to generate an observable anti-Stokes signal for our system sensitivity. For those NDs in the final data subset, that where we cannot distinguish the anti-Stokes signal and where no current was driven through the heater, we observe a small range of Raman shifts. However, none of the shifts are as extreme as in the cases of laser-induced heading. We note that in this dataset some data points have a Raman shift less than our bulk diamond, room-temperature reference measurement — we attribute this to strain variations present within NDs.

For measurements showing laser-induced heating — where the anti-Stokes / Stokes ratio can be determined (those in Figure 5.7a) — we plot the ratio as a function of the Raman shift, Figure 5.8a. A strong correlation between the intensity ratios and the Raman shift is apparent. This strengthens the hypothesis that temperature can be determined from the observed Raman shift, which is our ultimate vision for this project. It is evident however that the relationship between the intensity ratio and the Raman shift differs slightly for each ND. We can map these instrument-corrected anti-Stokes / Stokes ratio values to temperature via Equation 5.13. The differences between NDs are noticeable, but it is still possible to use the shift for thermometry.

Included in Figure 5.8b are the substrate-heated NDs, which we assign temperature values via the heater current and a standard PT100 temperature sensor (RS PRO PT100; RS Components) clamped on the front of the sample holder. Error bars have been generated by computing the largest and smallest anti-Stokes / Stokes ratios by either adding or subtracting the least squared fit errors for amplitude and width to maximise or minimise the area under the curve (Equation 5.11) accordingly. In the case that the computed errors reduce the amplitude of the anti-Stokes peak to zero, and subsequently the corresponding temperature to zero, the lower-bound error has been capped at room-temperature.

Our data appears in general agreement with Equation 5.8 (the Klemens model), however, our inferred temperatures appear too high for the corresponding Raman shift by a factor of $\sim 1.5\times$ in comparison with Liu et al's bulk diamond data [182], see Figure 5.10. There is clearly more work to do to resolve this discrepancy.

The analysis performed up to this point was built on the assumption that Equation 5.13 completely describes the relationship between temperature and ratio. This line of reasoning is summarised in Figure 5.9a, which visualises the logic of this analysis process. The discrepancy observed between the shift-vs-temp in Figure 5.10 raises the question of whether Equation 5.13 is truly appropriate to make this link. Since these measurements were conducted on nanodiamond materials, we recall that NDs have unique spatial geometries which
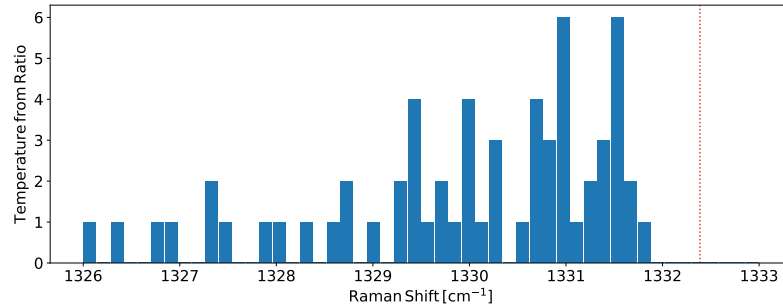
(a)
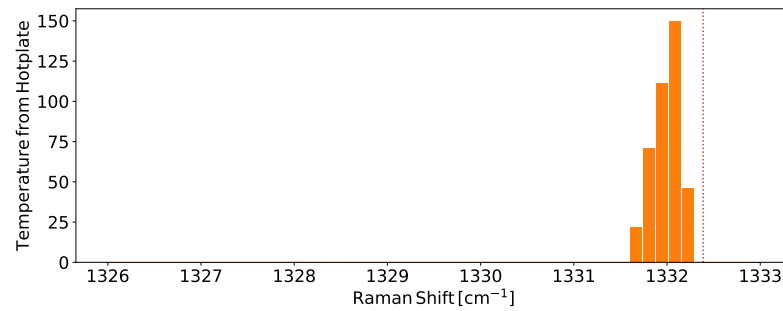
(b)
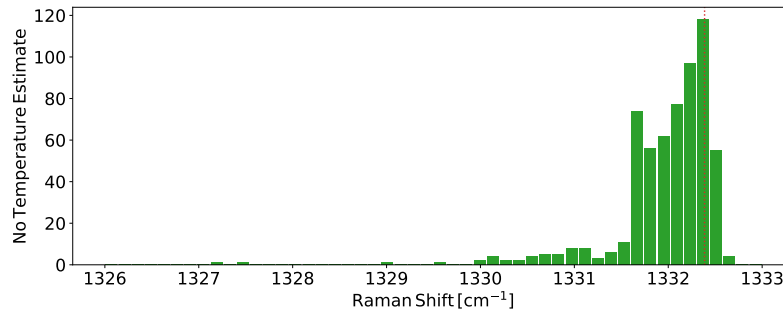
(c)

Figure 5.7: Histograms of Raman shifts with temperature. All measurement data has been placed into three histograms, with the bulk diamond, room-temperature reference indicated by the dashed red line. **(a)** Data where the anti-Stokes signal was able to be distinguished from the noise. For each of these data points the anti-Stokes / Stokes ratio can be determined, and hence the temperature of each ND inferred by that method. **(b)** Data where the temperature can be inferred by the current driven through the heating element. It is clear that NDs in this dataset never undergo as strong a Raman shift as those where the anti-Stokes signal can be observed. **(c)** Data where we cannot infer temperature information. Some data points have a Raman shift less than our bulk diamond, room-temperature reference measurement — we attribute this to high stress and strain present within NDs.
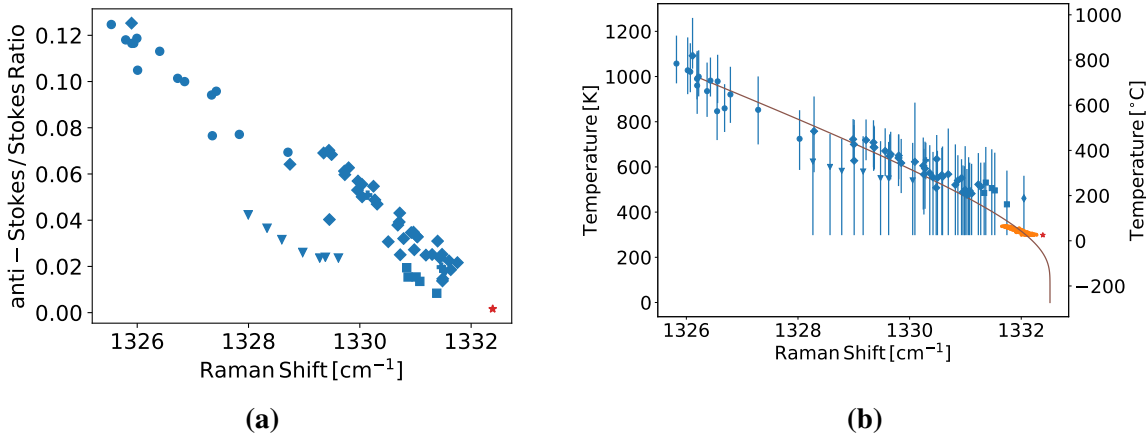
Figure 5.8: Preliminary Raman shift analysis of the collected data. (a) Instrument corrected anti-Stokes / Stokes intensity ratios for each ND, represented in the figure by different marker types, as a function of their measured Raman shift. We observe a strong correlation between the intensity ratios and the Raman shift. Our bulk diamond reference measurement is also included on the plot (red). **(b)** The same data but the anti-Stokes / Stokes ratio has been translated to temperature via Equation 5.13, and fit with the Klemens model, Equation 5.8. It is apparent that each individual ND dataset deviates by separate amounts from the fitted model. Also included on this plot are the substrate-heated NDs (orange).

can generate Mie resonances [198]. We now change the logic flow to that illustrated in Figure 5.9b in order to examine the plausibility of this effect.

The Mie resonances arising from ND geometry will modify the optical density of states. This will scale the ratio of the energies in Equation 5.7 by a factor β unique to each ND. To further generalise the fitting procedure that extracts temperature from our shifts via Liu et al, we also introduce a free offset parameter that accounts for the unique strain which each ND experiences. These modifications cause Equation 5.7 to take the new form

$$\frac{I_{\text{anti-Stokes}}}{I_{\text{Stokes}}} = \alpha\beta \left(\frac{\nu_{\text{AS}}}{\nu_{\text{S}}}\right)^3 e^{\frac{-\hbar\omega_p}{k_B T}} + \text{offset} \tag{5.14}$$

To conduct this fit we require a temperature reference for our data points. We choose to use the temperature as a function of Raman shift data in recorded bulk diamond from Liu et al [182]. Upon digitisation of this data we attempted to refit the Klemens 3-phonon decay model as conducted in the paper. Unfortunately, we were unable to reproduce the fit of Equation 5.8 to Liu et al's data, Figure 5.11a.

In fact, discrepancies with the fit to the data presented in the Liu et al paper have already been raised by other studies. Surovtsev and Kupriyanov [184] draw attention to several aspects that raise concern about the correctness of the results and the validity of Liu et al's conclusions, in particular with respect to the Raman linewidth data and its temperature dependence. These authors conclude that the higher-order (4-phonon) term is unambiguously required to explain the diamond Raman linewidth as a function of temperature. Curiously, this was required to fit data well below the diamond Debye temperature, whereas the silicon data Balkanski presented only required the 4-phonon term above the Debye temperature.

As Liu et al neglected to include the resulting fit parameters in their paper (the *A* coefficient in the Klemens model, Equation 5.8), we attempted to first reproduce the fit undertaken. This was conducted on data digitised from the papers fit curve. We were unable to match

(a)   **(b)**
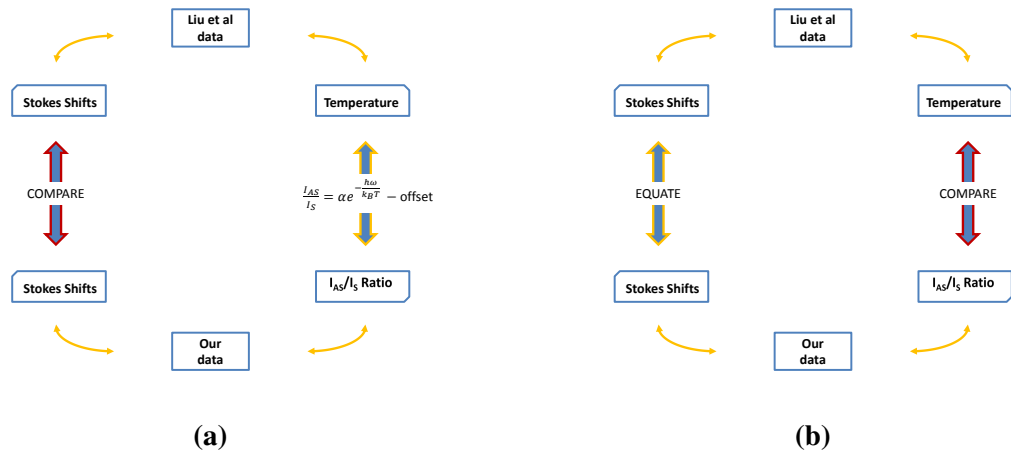
Figure 5.9: Data analysis logic methods. **(a)** The first approach taken was to connect our recorded data with Liu et al's bulk diamond data via Equation 5.13. When comparing the temperatures inferred from Raman shifts in Figure 5.10 our temperature value appear too high for the corresponding Raman shift by a factor of $\sim 1.5\times$. **(b)** We then change our approach and use Liu et al's bulk diamond data as our reference to determine temperature, and include the free parameter β in our fitting algorithm to account for Mie resonances on the nanoparticles which we believe to be the cause for the slight discrepancy between individual NDs that we see in our data.
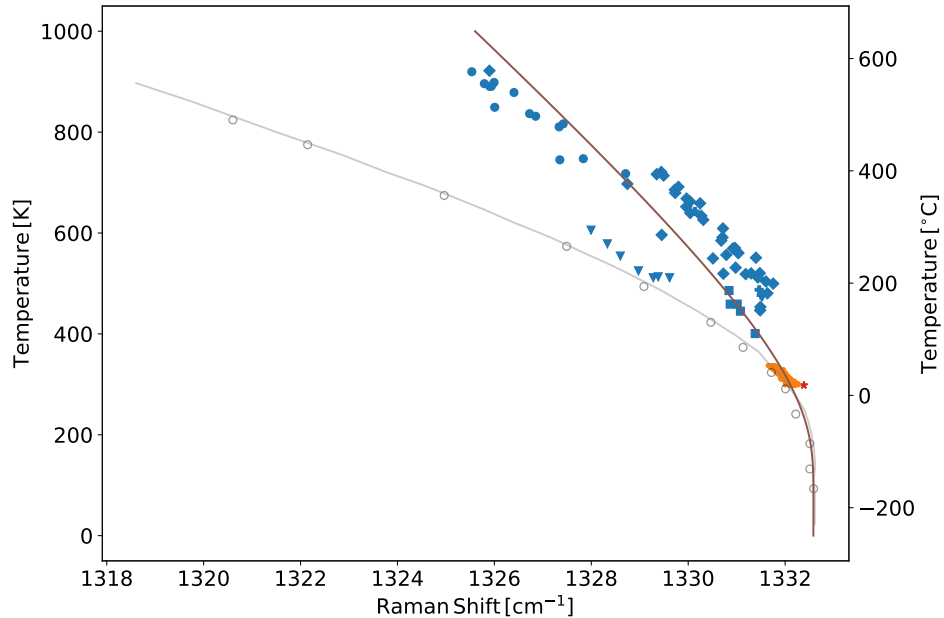
Figure 5.10: Comparison of collected data with data from the literature. We plot our collected data alongside data collected in bulk diamond in Liu et al's paper [182] (gray data and fit). Our temperature value appear too high for the corresponding Raman shift by a factor of $\sim 1.5\times$ in comparison with Liu et al's bulk diamond data.
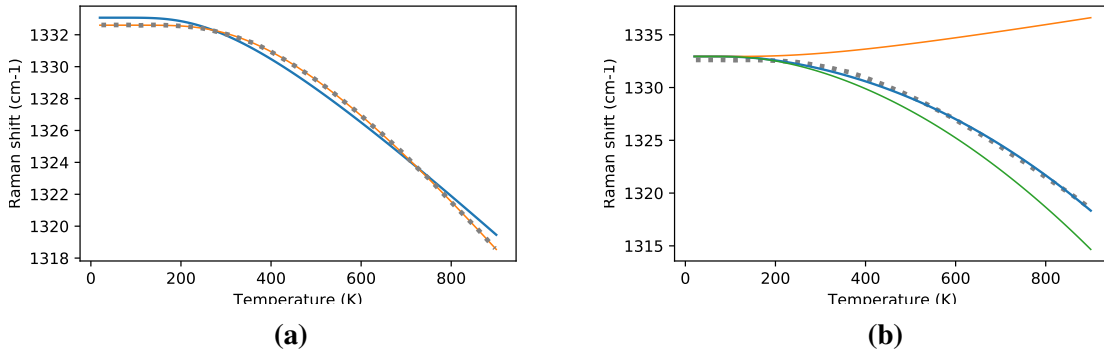
Figure 5.11: Phonon decay model fits to the Raman shift as a function of temperature in bulk diamond data recorded by Liu et al [182]. **(a)** We are unable to fit the Klemens 3-phonon decay model, Equation 5.8, to the Liu et al data set. Visually we can see the fits deviation from the data, and we extract the values $A = -12.91$, $\omega_0 = 1333.07\,\text{cm}^{-1}$, which do not match what we expect physically. Gray dots: The digitised Liu et al fit. Blue line: Our Klemens model fit to the digitised Liu et al fit. Orange line: Unphysical Klemens model fit with the value $\Delta E = 0.239\,\text{eV}$, and $A = -2.580$, $\omega_0 = 1332.6\,\text{cm}^{-1}$. **(b)** Our attempt to fit the Balkanski model, Equation 5.9, yields similarly unphysical result. Upon fitting the model to the data we extract $A = 3.484$, $B = -3.195$, $\omega_0 = 1332.94\,\text{cm}^{-1}$. The negativity of the coefficient weighting the Klemens decay channel, A, implies that Balkanski's higher-order correction is also strongly influencing the model at lower temperatures, which is an unphysical conclusion to draw. Gray dots: The digitised Liu et al fit. Blue line: Our Balkanski model fit to the digitised Liu et al fit. Orange line: The A coefficient (3-phonon term) only. Green line: The B coefficient (4-phonon term) only.

the curvature of the model to Liu et al's fit, see Figure 5.11a. We suspect that when fitting the Klemens model to their data Liu et al included a free-parameter in the argument of their exponent, as we find that the fit is optimised for the unphysical value $\Delta E = 0.239\,\text{eV}$ (in the case of diamond $\Delta E = 0.165\,\text{eV}$, which corresponds to $1332\,\text{cm}^{-1}$). In fact, the parameters $\Delta E = 0.239\,\text{eV}$, and $A = -2.580$, $\omega_0 = 1332.6\,\text{cm}^{-1}$ give exact overlap with Liu et al's plotted fit curve, within the digitisation precision.

In the light of works reported for silicon [174], one explanation for the poor fit of the Klemens model to Liu et al data might be that higher order corrections are required. Therefore, we fit Balkanski's modified Klemens model[ii] to Liu et al's data, Figure 5.11b. While initially one might consider the fit to be adequate, upon closer examination the leading fit coefficient, A, that describes the Klemens decay channels produces a positive curvature, Figure 5.11b. This inflexion implies that Balkanski's higher-order correction is also strongly influencing the model at lower temperatures, which is an unphysical conclusion to draw.

Clearly a thorough and detailed theoretical investigation into the mechanism of the phonon decay channels is required. Such an investigation is beyond the scope of this thesis. To continue our exploration we still need a function to map Stokes shift to temperature. In order to progress we interpolate Liu et al's data using a one-dimensional piecewise linear interpolant to produce a lookup table with adequate resolution. We acknowledge the assumption that

---

[ii] For ease of reference Balkanski's 4-phonon model, Equation 5.9, is reproduced here:

$$\Omega\left(T\right) = \omega_0 + A\left(\frac{2}{e^{\frac{\hbar\omega_0}{2k_BT}} - 1}\right) + B\left(\frac{3}{\left(e^{\left(\frac{\hbar\omega_0}{3k_BT}\right)}\right)^2 - 1} + \frac{3}{e^{\frac{\hbar\omega_0}{3k_BT}} - 1}\right)$$

Table 5.1: Optimised fit parameters. Listed are the optical density of states modification factor β, as per Equation 5.14, to account for Mie resonances on each individual ND. The value has been included as a free fitting parameter in the model.

β	offset
0.690	−0.108
0.848	0.152
0.725	−0.072
0.663	−0.437
0.693	−0.738

Raman shifts in nanodiamond material are identical to that in bulk diamond material. While the Raman line appears shifted in ultrasmall NDs (size $\leq$ 10 nm) because of phonon confinement effects [187, 199, 200], our NDs are ~ 250 nm in size, so we judge this to be a fair assumption.

Using this interpolation of Liu et al's bulk diamond data as our reference to determine temperature, we take β as a fit parameter in Equation 5.14 and optimise to match our data for each individual ND. The resulting fits are shown in Figure 5.12. We find that by optimising β, and therefore adjusting the optical density of states, our data converges with the bulk diamond reference dataset. The closeness of this fit suggests that our assumption whereby our sample NDs experience the same temperature dependent Raman shifts in comparison with bulk diamond seems valid. The optimised fit parameters are listed in Table 5.1.

This result demonstrates that Mie resonances can affect optical emission from ND particles. This has particular implication to thermometry techniques, or any other measurement procedure, through which the relative intensities of spectrally separated bands are used as a criterion, such as those presented in [201, 202]. Furthermore this also highlights the advantages of utilising the Raman shift as a temperature metric as opposed to the Raman lineshape or linewidth, as the method is still valid in the case of inhomogeneities across the sample.

5.3   Conclusions and Implications

In the collected data, § 5.2.4, the occurrence of optical heating induced by an excitation laser is more prevalent and more capable of temperature alterations in ND systems than previously thought. Subsequent analysis, § 5.2.6, reveals that these NDs could be heated up to ~ 900 K with ~ 160 mW of off-resonant laser power. We suspect that these NDs are in poor thermal contact with the substrate. Furthermore, we note that such high-temperature can lead to air-oxidation of diamond, however, this will occur on a longer time scale (~ hours) than the measurement time [203].

These also appear to be the measurements where the anti-Stokes signal can be distinguished, and therefore the anti-Stokes / Stokes signal intensity ratio determined. This is due to the fact that the higher temperature of the ND corresponds to a higher phonon spectral density, leading to a more efficient anti-stokes signal. In § 5.2.6 we have investigated the dependence of the anti-Stokes / Stokes ratio which we map to temperature via Equation 5.7. We find complications with fitting both the Klemens 3-phonon decay model, Equation 5.8, and Balkanski's 4-phonon decay model, Equation 5.9 to our data set and to a reference bulk diamond data set recorded by Liu et al.

By introducing a scaling factor, β, to the optical density of states, Equation 5.14, our data converges with Liu et al's bulk data measurements. This factor can account for Mie resonances on the nanoparticles which we believe to be the cause for the slight discrepancy between individual NDs that we see in our data.

These new implications raise an interesting question in the context of our previously conducted superradiance investigation, Chapter 3. The reader should recall that the temperature dependence of superradiant emission, originating from ensembles of NV centres in ND systems, may be a fruitful investigation. We theorise that increasing the temperature of these systems might increase the spectral indistinguishability of the NV emitters, through both inhomogeneous and homogeneous broadening effects. The influence of this indistinguishability increase may in fact promote a higher degree of superradiant behaviour. This new evidence raises the question of the effects of optical heating and subsequently the temperature of the each individual ND in our superradiance investigation. A further investigation into the influence of this effect is now a future research project planned for the lab.
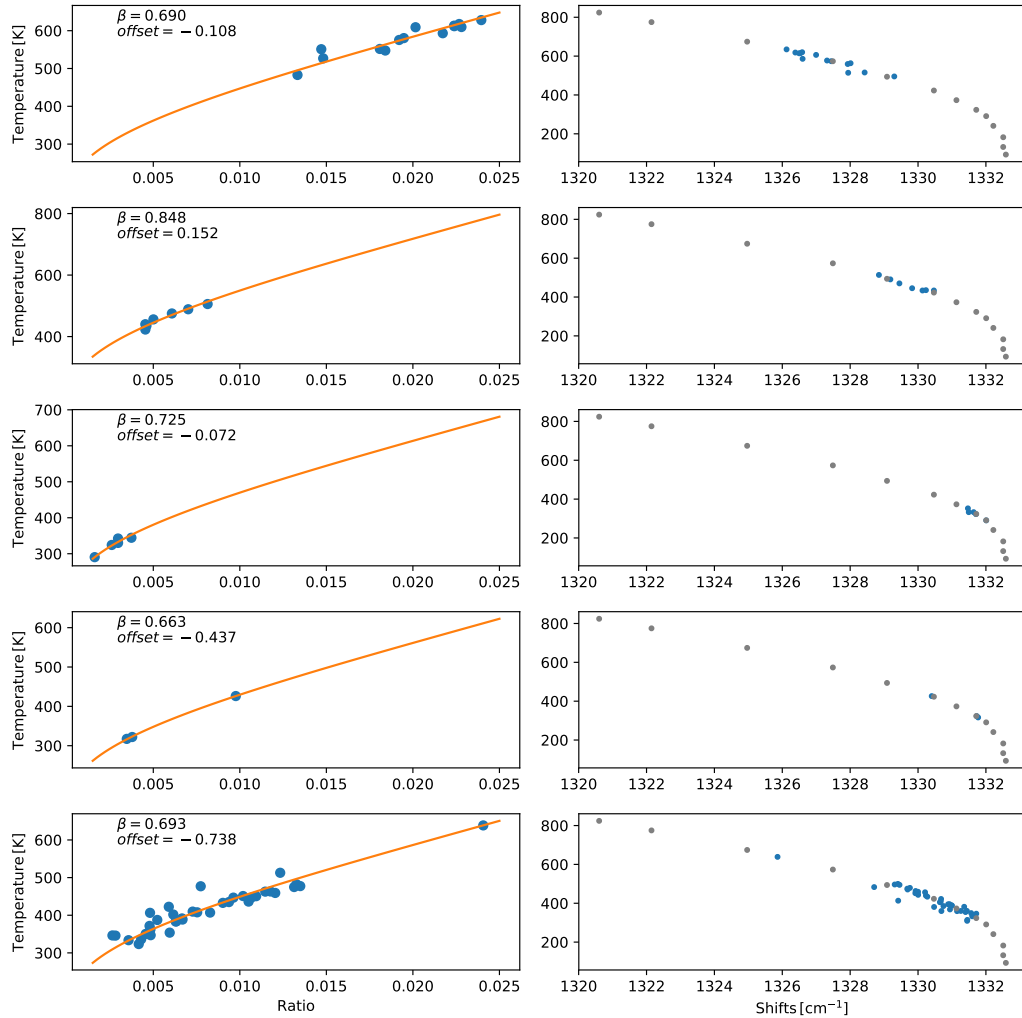
Figure 5.12: Individual ND datasets with optimisation of an energy scaling parameter. In order to account for Mie resonances we have introduced a fit parameter, β (as per Equation 5.14), to alter the optical density of states. An offset parameter has also been included to account for the unique strain experiences by each ND, as outlines in the text. By including these fit parameters we are able to converge our individual ND datasets to Liu et al's bulk diamond reference data. Each subplot represents measurements conducted on individual NDs. Left column: temperature vs ratio from Equation 5.14 (orange) which the fitted data points plotted (blue). Right column: demonstration plotting our *beta* and offset corrected temperature values with the values observed in bulk diamond by Liu et al. The good overlap of this data demonstrates the effectiveness of our fit.

6

Conclusions

"Poets say science takes away from the beauty of the stars — mere globs of gas atoms. I, too, can see the stars on a desert night, and feel them. But do I see less or more?"

Richard Feynman

In introducing the background and scope of this thesis, § 1.1, I discussed our goal of enabling diamond-based nanotechnology applications by enhancing our underpinning knowledge of the nitrogen-vacancy (NV) centre in nanodiamond materials. In this regard, the outcome of this thesis has been threefold. Firstly, we coupled a dielectric loaded resonator (DLR) microwave cavity to a single NV spin hosted in a nanodiamond (ND), trialling a new method for interacting, contactless and over centimetre-size scales. Next, we investigated NDs containing dense ensembles of NV centres and observed a new phenomena — room-temperature spontaneous superradiance [122]. Finally, we explored colour centre independent nanoscale thermometry with individual NDs. Additionally, content was included on the overhaul of our lab control systems, whereby significant work was undertaken to construct and integrate lab hardware for the purpose of conducting semi-autonomous measurements.

Coupling of a Single NV Centre to a Microwave Cavity

In Chapter 2 I presented my work on coupling the microwave field generated by a macroscopic microwave cavity to a single NV centre hosted within a ND. The cavity was suspended ~ 1 cm above the sample — avoiding issues related to sample heating which occur when a typical stripline antenna is used for generating the microwave field addressing the NV spin. We confirmed our alignment with a single NV centre via $g^{(2)}$ correlation measurements. Then, with both the cavity and a stripline antenna, used for reference, we conducted an optically detected magnetic resonance (ODMR) measurement to determine the energy level separation between the NV ground triplet state, and tuned the microwave cavity mode to the corresponding resonant frequency. We conducted Rabi oscillation measurements, from which the Rabi frequency and the duration of a π-pulse were extracted. Next, we implemented a Hahn spin-echo pulse sequence to measure the coherence time of the NV spin.

This was successfully measured in our stripline antenna reference sample, however, in the case of the microwave cavity sample the measurement was ultimately unsuccessful. We speculate that the high Q-factor of the DLR cavity alters the shape of the microwave pulses and is particularly critical at short time scales.

For future work, we postulated design criteria for a second-generation DLR cavity for addressing NV spins, which included greater power throughput, vertical optical access for alignment, and a mechanical plunger to dynamically tune the cavity mode. This technology should find future application in contactless measurements addressing NV spin systems with a homogeneous microwave field over large areas ($\sim$ centimetres) in comparison with traditional stripline antenna schemes. With an additional prototype iteration the cavity could be employed for the coherent control of NV spin systems.

NV Superradiance in Nanodiamond

In Chapter 3 we explored the dynamics of many-NV systems contained within individual diamond nanocrystals. These results represent the most substantial and novel component of this thesis. When packed at a sufficiently high density, the many-NV centres can exhibit cooperative effects, which we interrogate through the observation of superradiant emission — observing NV lifetimes as short as 1.1 ns. Our measurements show significant speed-up in the photon emission rate, and we confirmed the state of the system by observing super-Poissonian photons statistics that scale as predicted by our model. This observation of cooperative effects in ND NV systems is the first for a solid-state, room-temperature system analogous to what was originally proposed by Dicke in his pioneering paper in 1954 [123].

Alongside our results, we also discussed how our findings are relevant, ultimately, for developing diamond-based quantum engineered superradiant systems at room-temperature — which might lead to applications including efficient photon detection, energy harvesting and quantum sensing. For future experiments, we consider exploring the dependence of NV superradiant emission on temperature (predicting reduced superradiant behaviour if the system is cooled to low-temperature due to reduced photon indistinguishably), as well as on the density of NVs owing to dipole-dipole interactions possibly destroying cooperativity between NV centres. Also, we plan on engineering specific geometries for deterministic superradiance and superabsorption, and implementing these experiments in other diamond-based systems such as the silicon-vacancy colour centre.

Lab Control Systems Upgrade

Over the course of the measurements conducted in this thesis a significant process of modernisation and automation of lab systems was undertaken. An overview of this endeavour has been outlined in Chapter 4, where I discussed the developments we undertook to enable semi-autonomous measurements. The upgraded lab systems were employed for our thermometry measurements, allowing large and systematic data sets to be collected while real time feedback from data analysis was used to drive an educated exploration of the parameters space. Our control systems requirements were outlined, and a description of the architecture of the open-source software on which we integrated our hardware was condensed and presented, accompanied with examples. Furthermore, our adopted version control workflow which enabled scalable and non-linear development was discussed. This lab control system has now been implemented throughout our research labs. The hardware interfacing code as well as the numerous software packages we developed have been uploaded for free and for

global use for the Qudi project [160], which a worldwide community of programmers and physicists constantly use and upgrade.

I included in the thesis the process we developed for calibration of the spectrograph, as this was a significant part of the project. A translational research grant has since been awarded to facilitate development of a second-generation prototype and ultimately work towards commercialisation of this instrument.

Nanodiamond Thermometry

In Chapter 5 I presented our work on the development of a technique for measuring temperature at the nanoscale independently of colour centres. The method relies on Raman spectroscopy of individual NDs, and is enabled by the acquisition of an ultra-high resolution échelle spectrograph designed for both the search for extra-solar planets and for extra-solar spectroscopy. The spectrograph design allows for single-shot readout from ~ 490–$770\,\mathrm{nm}$, allowing for simultaneous detection of the Stokes and anti-Stokes scattered photons.

In this study we found that heating induced by an excitation laser can be more significant in altering the temperature of NDs than previously thought. The analysis reveals that NDs excited by a focused laser beam can be heated up to $\sim 900\,\mathrm{K}$ with $\sim 160\,\mathrm{mW}$ of off-resonant laser power. We suspect that this occurs when the NDs are in poor thermal contact with the substrate. When investigating the relationship between the ratio of the anti-Stokes and Stokes signals and the Raman shift we found discrepancies when fitting the established 4-phonon decay model with the experimental data. For each individual ND the data could be matched to that of a reference measurement in bulk diamond by altering the optical density of states, and we attribute this affect to Mie resonances on the nanoparticles. This work leads us to question the contribution of laser-induced heating in our earlier study of superradiance, where we theorised that increasing the temperature of a ND may result in increased cooperative behaviour through increasing the spectral indistinguishably of the emitters. In the thesis we commented that including Balkanski's high-order fit coefficient strongly influences the phonon decay process in diamond below the Debye temperature, unlike in the case of other group IV semiconductors. Additionally, the 3-phonon and 4-phonon model coefficients were found here to be of opposite sign. This indicates that the "higher-order correction" was far from a small adjustment, a significant deviation from Balkanski's application to the phonon decay process in silicon. Further investigations have commenced into the mechanisms of phonon decay channels in diamond to seek resolution in modelling of temperature dependence of the Raman line.

As the frontiers of diamond-based nanotechnologies evolve, so does the endeavour of harnessing and designing the properties of colour centres for ad-hoc applications and technologies. In particular, as the scientific community forges through the second quantum revolution [204], our understanding of NV spin systems lies at the crux of their adoption as a unique platform for engineering room-temperature, solid-state quantum systems with a diverse range of applications. The NV defect in diamond will continue to push the envelope of quantum nanoscience either directly or through the incredibly vast wealth of knowledge the community has built on this truly unique quantum jewel.

<div align="right">

A

</div>

Supplementary NV Spin Physics

"If quantum physics hasn't profoundly shocked you, you haven't understood it yet."

<div align="right">

Niels Bohr

</div>

This appendix contains supplementary information regarding the NV spin physics that is presented in Chapter 2.

A.1   Solving for the NV Energy Eigenvalues

Solving the Hamiltonian time-independent Schrödinger equation will produce the energy eigenvalues of the system. This can be achieved via the following process.

The time-independent Schrödinger equation is

$$\hat{\mathcal{H}}\psi = \lambda\psi \tag{A.1}$$

To find the eigenvalues we solve the characteristic equation

$$0 = \hat{\mathcal{H}}\psi - \lambda\psi \tag{A.2}$$

$$= \hat{\mathcal{H}}\psi - \lambda\mathbf{I}\psi \tag{A.3}$$

$$= (\hat{\mathcal{H}} - \lambda\mathbf{I})\psi \tag{A.4}$$

We know $\psi \neq 0$ if $\det\left|\hat{\mathcal{H}} - \lambda\mathbf{I}\right| = 0$, which we compute:

$$\hat{\mathcal{H}} - \lambda\mathbf{I} = \begin{pmatrix} \hbar D_g + g_e\mu_B B_z - \lambda & 0 & \hbar E \\ 0 & -\lambda & 0 \\ \hbar E & 0 & \hbar D_g - g_e\mu_B B_z - \lambda \end{pmatrix} \tag{A.5}$$

$$= \begin{pmatrix} 0 & -\lambda & 0 \\ \hbar D_g + g_e\mu_B B_z - \lambda & 0 & \hbar E \\ \hbar E & 0 & \hbar D_g - g_e\mu_B B_z - \lambda \end{pmatrix} \tag{A.6}$$

and therefore

$$\det \left| \hat{\mathcal{H}} - \lambda \mathbf{I} \right| = \lambda \left(\lambda^2 - \lambda \left(2\hbar D_g \right) + \left(\hbar^2 D_g^2 - g_e^2 \mu_B^2 B_z^2 - \hbar^2 E^2 \right) \right) \tag{A.7}$$

$\lambda = 0$ is the trivial solution, and the other solution

$$\lambda^2 - \lambda \left(2\hbar D_g \right) + \left(\hbar^2 D_g^2 - g_e^2 \mu_B^2 B_z^2 - \hbar^2 E^2 \right) = 0 \tag{A.8}$$

which gives the solutions

$$\lambda = \hbar D_g \pm \sqrt{(\hbar E)^2 + (g_e \mu_B B_z)^2} \tag{A.9}$$

and determines the eigenvalues of the system.

A.2   Evolving the NV Spin System in a Driving Field

Solving the Schrödinger Equation

The method of solving the time-dependent Schrödinger equation is followed here. The time-dependent Schrödinger equation is:

$$i\hbar \frac{d}{dt} |\psi\rangle = \hat{\mathcal{H}}_{int} |\psi\rangle \tag{A.10}$$

where ψ is the time-dependent state

$$|\psi(t)\rangle = \alpha(t) |\downarrow\rangle + \beta(t) |\uparrow\rangle \tag{A.11}$$

and α and β are amplitudes whose modulus squared sum to one. To solve the Schrödinger equation for our generic state and Hamiltonian

$$i\hbar \frac{d}{dt} (\alpha |\downarrow\rangle + \beta |\uparrow\rangle) = \hat{\mathcal{H}}_{int} (\alpha |\downarrow\rangle + \beta |\uparrow\rangle) \tag{A.12}$$

$$= \frac{\Omega}{2} (|\downarrow\rangle \langle\uparrow| + |\uparrow\rangle \langle\downarrow|) (\alpha |\downarrow\rangle + \beta |\uparrow\rangle) \tag{A.13}$$

$$= \frac{\Omega}{2} (((|\downarrow\rangle \langle\uparrow| + |\uparrow\rangle \langle\downarrow|) \alpha |\downarrow\rangle) + (|\downarrow\rangle \langle\uparrow| + |\uparrow\rangle \langle\downarrow|) \beta |\uparrow\rangle) \tag{A.14}$$

$$= \frac{\Omega}{2} (\alpha |\uparrow\rangle + \beta |\downarrow\rangle) \tag{A.15}$$

we create a pair of coupled ordinary differential equations (ODEs) through the application of $\langle\downarrow|$ an $\langle\uparrow|$ 'from the left'. The coupled ODEs are

$$\langle\downarrow| : \quad i\hbar \frac{d}{dt} \alpha = \frac{\Omega}{2} \beta \tag{A.16}$$

$$\langle\uparrow| : \quad i\hbar \frac{d}{dt} \beta = \frac{\Omega}{2} \alpha \tag{A.17}$$

To solve these ODE we combine the solution from applying $\langle\downarrow|$

$$i\hbar \frac{d}{dt} \beta = \frac{\Omega}{2} \alpha \tag{A.18}$$

$$\frac{d}{dt} \beta = -\frac{i\Omega}{2\hbar} \alpha \tag{A.19}$$

with the solution from applying $\langle\uparrow|$

$$i\hbar\frac{d^2}{dt^2}\alpha = \frac{\Omega}{2}\frac{d}{dt}\beta \tag{A.20}$$

$$= -\frac{\Omega}{2}\frac{i\Omega}{2\hbar}\alpha \tag{A.21}$$

$$\frac{d^2}{dt^2}\alpha = -\frac{\Omega^2}{4\hbar^2}\alpha \tag{A.22}$$

$$\alpha = \cos\left(\frac{\Omega t}{2\hbar}\right) \tag{A.23}$$

and therefore find the probability of being in the ground state[i]

$$P_\downarrow = |\alpha|^2 \tag{A.24}$$

$$= \cos^2\left(\frac{\Omega t}{2\hbar}\right) \tag{A.25}$$

and the probability of being in the excited state

$$P_\uparrow = |\beta|^2 \tag{A.26}$$

$$= \sin^2\left(\frac{\Omega t}{2\hbar}\right) \quad \because \left|\alpha^2\right| + \left|\beta^2\right| = 1 \tag{A.27}$$

Unitary Evolution of the System

We can also describe how the two-level system behaves in the presence of an external field through computing its unitary evolution, which has the form

$$\hat{U} = e^{-\frac{i}{\hbar}\mathcal{H}t} \tag{A.28}$$

Taking the interaction Hamiltonian and applying the unitary transformation to the ground state

$$|\psi(t)\rangle = \hat{U}(t)|\psi(0)\rangle \tag{A.29}$$

$$= \exp\left[\frac{it}{\hbar}\begin{pmatrix} 0 & \Omega/2 \\ \Omega/2 & 0 \end{pmatrix}\right]\begin{pmatrix} 1 \\ 0 \end{pmatrix} \tag{A.30}$$

$$= \begin{pmatrix} \cos\left(\frac{\Omega t}{2\hbar}\right) & -i\sin\left(\frac{\Omega t}{2\hbar}\right) \\ -i\sin\left(\frac{\Omega t}{2\hbar}\right) & \cos\left(\frac{\Omega t}{2\hbar}\right) \end{pmatrix}\begin{pmatrix} 1 \\ 0 \end{pmatrix} \tag{A.31}$$

$$= \begin{pmatrix} \cos\left(\frac{\Omega t}{2\hbar}\right) \\ -i\sin\left(\frac{\Omega t}{2\hbar}\right) \end{pmatrix} \tag{A.32}$$

$$= \begin{pmatrix} \alpha(t) \\ \beta(t) \end{pmatrix} \tag{A.33}$$

we find the same description for the probability of being in the ground state

$$P_\downarrow = |\alpha|^2 \tag{A.34}$$

$$= \cos^2\left(\frac{\Omega t}{2\hbar}\right) \tag{A.35}$$

---

[i]True only if at $t = 0$ the state is entirely in the spin down (i.e. ground) state $|\downarrow\rangle$, with no spin up component.

and in the excited state

$$P_\uparrow = |\beta|^2 \tag{A.36}$$

$$= \sin^2\left(\frac{\Omega t}{2\hbar}\right) \tag{A.37}$$

This is the same result as obtained from solving the Schrödinger equation above.

B

NT-MDT Programatic Control

"It is not the critic who counts; not the man who points out how the strong man stumbles, or where the doer of deeds could have done them better. The credit belongs to the man who is actually in the arena, whose face is marred by dust and sweat and blood; who strives valiantly; who errs, who comes short again and again, because there is no effort without error and shortcoming; but who does actually strive to do the deeds; who knows great enthusiasms, the great devotions; who spends himself in a worthy cause; who at the best knows in the end the triumph of high achievement, and who at the worst, if he fails, at least fails while daring greatly, so that his place shall never be with those cold and timid souls who neither know victory nor defeat."

Theodore Roosevelt

This appendix contains code referenced in § 4.3 to achieve communication between Qudi, Nova Px, and the NT-MDT stage.

B.1 Qudi ↔ Nova Px Communication

The functions below were created to pass commands/data between Qudi and Nova Px. The C programming language was required to be used for this communication process as communication must be passed through the Nova Px DLL interface.

B.1.1 Command Packet Parsing

The two functions below work to pass command packets (snippets of Nova Power Script code) to the Nova Px control software where it can be executed. These functions are designed to pass arbitrary command packets, such that they can be used by any 'parent' function. The only difference between these two functions is thread execution, with `_run_script_text_thread` able to be used to interrupt processes that are already running (helpful for functions such as `_emergency_interrupt`).

```
1    def _run_script_text(self, command):
2        """ Execute a command in Nova Px
3
4        @param string command : VBScript code to be executed
5        """
6
7        self._novadll.RunScriptText(command.encode())
8
9    def _run_script_text_thread(self, command):
10       """ Execute a command in a Nova Px in a separate thread
11
12       This function can be used to interrupt a running process. Nova Px
13       software must be revision 18659 or newer for this function.
14
15       @param string command : VBScript code to be executed
16       """
17
18       self._novadll.RunScriptTextThread(command.encode())
```

B.1.2 Float Retreival

The only data type required to be passed back from the instrument to Qudi are float variables (real numbers with significant figures to the right of the decimal point). For example, if the position of the stage were to be requested, first the x-value would be returned, then the y-value, and finally the z-value — all of type float. For our implementation of the NT-MDT stage no other data types are required to be passed back from the instrument. The function created to retrieve these variables is shown below.

```
1    def _get_shared_float(self, variable):
2        """ Retreive a shared data variable of type float from Nova Px
3
4        @param string variable : The variable must have already been created
5
6        @returns float value : The value of variable
7        """
8
9        outbuf = ctypes.c_double()
10       buflen = ctypes.c_int()
11
12       self._novadll.GetSharedData(variable.encode(), None, ctypes.byref(buflen))  # get
                the required buffer size
13       self._novadll.GetSharedData(variable.encode(), ctypes.byref(outbuf), ctypes.byref(
                buflen))  # fill the buffer
14
15       return outbuf.value
```

Upon retrieving a variable we clear the data being stored in that variable, such that we do not continue to store obsolete information.

```
1    def _reset_shared_data(self, variable):
2        """ Reset a shared data variable
3
4        @param string variable : The variable must have already been created
5        """
6
7        self._novadll.ResetSharedData(variable.encode())
```

B.1.3 GUI Update

Because we are interacting with the ND-MDT stage through its own control software, we would like the graphical user interface (GUI) of this software to reflect the current state of

the stage. To achieve this, any time that we alter that state of any of the stages properties
(such as toggling the feedback state to on/off) we update the GUI to reflect the change.

```python
def _update_gui(self):
    """ Update the Nova Px graphical user unterface

    this operation is noted to be "not threadsafe" in the original documentation
    """

    command = 'Perform tGlobal, gGUIUpdate'
    self._run_script_text(command)
```

Here we also see the first occurrence of a command packet, found on line 7 of the above code
snippet. The variable `command` is a string (a set of characters) containing Nova Power Script
code to be executed.

B.1.4   Handshake

Lastly, we use a combination of the above functions to ensure a successful handshake (soft-
ware connection) between Qudi and Nova Px at start-up. We check this through first initial-
ising a new variable of type float to a particular value (we use that of the golden ratio φ, but
any value can be chosen). Then, we simply retrieve the value of the variable that we set and
cross-check that their values are equal. Upon a successful handshake we then clear the test
variable.

```python
def _check_connection(self):
    """ Set and get a shared variable to check the connection with Nova Px

    @returns bool success : True if values match
    """

    command = 'SetSharedDataVal "test_connection", 1.61803398875, "F64", 8'
    self._run_script_text(command)
    if self._get_shared_float('test_connection') == 1.61803398875:
        self._reset_shared_data('test_connection')
        return True
    else:
        return False
```

B.2   Nova Px ↔ Stage Communication

With communication now established between Qudi and the Nova Px control software we
can now pass 'command packets' (snippet of code written in Nova Power Script) to be exe-
cuted for control of the stage. In combination with the ability to retrieve floats, we now have
all of the required base-level tools to drive the movement of the stage. Below are listed and
described higher-level 'parent' functions that have been created to operate the stage. This set
of functions fulfils the set of operations required for 'motor' classified hardware files to be
integrated and fully functioning with the Qudi control software.

B.2.1   Hardware Activation / Deactivation

The first functions which we group here are the hardware activation and deactivation func-
tions. The function `on_activate` performs a check of the operating system architecture
(assuming a Windows environment), and loads the appropriate DLL (function library) for ei-
ther 64-bit or 32-bit architecture. We then see a call to load the constraints of the instrument,

which we will comment on shortly. Utilising the handshake check presented above, the code
then ensures that the communication link between Qudi and Nova Px has been successful.
Upon a successful connection, the closed-loop feedback state of the stage is activated, see
line 29.

```python
def on_activate(self):
    """ Initialisation performed during activation of the module.

        @return: error code (0:OK, -1:error)
    """
    if platform.architecture()[0] == '64bit':
        path_dll = os.path.join(os.path.abspath(''),
                                'thirdparty',
                                'nt_mdt',
                                'NovaSDK_x64.dll'
                                )
    elif platform.architecture()[0] == '32bit':
        path_dll = os.path.join(os.path.abspath(''),
                                'thirdparty',
                                'nt_mdt',
                                'NovaSDK.dll'
                                )
    else:
        self.log.error('Unknown platform, cannot load the Nova SDK dll.')

    self._novadll = ctypes.windll.LoadLibrary(path_dll)

    time.sleep(1)

    self._configured_constraints = self.get_constraints()

    if self._check_connection():
        self.log.info('Nova Px handshake successful')
        self._set_servo_state(True)
        return 0
    else:
        self.log.error('I cannot connect to Nova Px')
        return 1
```

The deactivation call is much simpler, toggling the closed-loop feedback state to 'off.'

```python
def on_deactivate(self):
    """ Deinitialisation performed during deactivation of the module.
        @return: error code (0:OK, -1:error)
    """
    self._set_servo_state(False)
    return 0
```

B.2.2   Load Instrument Constraints

This function acts to load information stored in the device configuration file, information
such at the stage and individual axis identification numbers used to address each motor.
Within the ND-MDT hardware there are actually two separate stages present; the primary
piezo-electric stage used to move the sample, and a secondary piezo-electric stage called the
'tube' which can be utilised to move the objective itself. If the user has declared the required
information (in the configuration file) to load the 'tube' stage, then it is constraints are also
loaded.

```python
def get_constraints(self):
    """ Retrieve the hardware constrains from the motor device.

        @return dict: dict with constraints for the sequence generation and GUI

        Provides all the constraints for the xyz stage  and rot stage (like total
        movement, velocity, ...)
        Each constraint is a tuple of the form
```

```python
9                   (min_value, max_value, stepsize)
10           """
11           constraints = OrderedDict()
12
13           config = self.getConfiguration()
14
15           axis0 = {}
16           axis0['label'] = 'x'
17           axis0['scanner'] = config['x']['device_id']
18           axis0['channel'] = config['x']['channel']
19           axis0['pos_min'] = config['x']['constraints']['pos_min']
20           axis0['pos_max'] = config['x']['constraints']['pos_max']
21
22           axis1 = {}
23           axis1['label'] = 'y'
24           axis1['scanner'] = config['y']['device_id']
25           axis1['channel'] = config['y']['channel']
26           axis1['pos_min'] = config['y']['constraints']['pos_min']
27           axis1['pos_max'] = config['y']['constraints']['pos_max']
28
29           axis2 = {}
30           axis2['label'] = 'z'
31           axis2['scanner'] = config['z']['device_id']
32           axis2['channel'] = config['z']['channel']
33           axis2['pos_min'] = config['z']['constraints']['pos_min']
34           axis2['pos_max'] = config['z']['constraints']['pos_max']
35
36           # check if the user has specified they have the 'tube' scanner
37           if [s for s in config['axis_labels'] if 'tube' in s]:
38
39                   axis3 = {}
40                   axis3['label'] = 'tube_x'
41                   axis3['scanner'] = config['tube_x']['device_id']
42                   axis3['channel'] = config['tube_x']['channel']
43                   axis3['pos_min'] = config['tube_x']['constraints']['pos_min']
44                   axis3['pos_max'] = config['tube_x']['constraints']['pos_max']
45
46                   axis4 = {}
47                   axis4['label'] = 'tube_y'
48                   axis4['scanner'] = config['tube_y']['device_id']
49                   axis4['channel'] = config['tube_y']['channel']
50                   axis4['pos_min'] = config['tube_y']['constraints']['pos_min']
51                   axis4['pos_max'] = config['tube_y']['constraints']['pos_max']
52
53                   axis5 = {}
54                   axis5['label'] = 'tube_z'
55                   axis5['scanner'] = config['tube_z']['device_id']
56                   axis5['channel'] = config['tube_z']['channel']
57                   axis5['pos_min'] = config['tube_z']['constraints']['pos_min']
58                   axis5['pos_max'] = config['tube_z']['constraints']['pos_max']
59
60           # assign the parameter container for x to a name which will identify it
61           constraints[axis0['label']] = axis0
62           constraints[axis1['label']] = axis1
63           constraints[axis2['label']] = axis2
64
65           # check if the user has specified they have the 'tube' scanner
66           if [s for s in config['axis_labels'] if 'tube' in s]:
67               constraints[axis3['label']] = axis3
68               constraints[axis4['label']] = axis4
69               constraints[axis5['label']] = axis5
70
71           if axis0['scanner'] != axis1['scanner']:
72               self.log.warning('Your x and y axes are configured as different devices, is
                    this correct?')
73
74           if [s for s in config['axis_labels'] if 'tube' in s]:
75               if axis3['scanner'] != axis4['scanner']:
76                   self.log.warning('Your x and y tube axes are configured as different
                        devices, is this correct?')
77
78           return constraints
```

B.2.3   Toggling the Closed-Loop Feedback State

We have seen above that the closed-loop feedback state is toggled 'on/off' upon activation/deactivation, respectively. To achieve this, we first address each axis independently, and this call is then filtered through to the specific commands required to conduct the action.

```python
def _set_servo_state(self, to_state):
    """ Internal method enabling / disabling the stage feedback

    @param bool to_state : desired state of the feedback servos
    """

    self._set_servo_state_xy(self._configured_constraints['x']['scanner'], to_state)
    time.sleep(0.5)
    self._update_gui()

    #  not required, but will catch an odd configuration
    self._set_servo_state_xy(self._configured_constraints['y']['scanner'], to_state)
    time.sleep(0.5)
    self._update_gui()

    self._set_servo_state_z(self._configured_constraints['z']['scanner'], to_state)
    time.sleep(0.5)
    self._update_gui()

    #  check if the user has specified they have the 'tube' scanner
    if [s for s in self._configured_constraints if 'tube' in s]:

        self._set_servo_state_xy(self._configured_constraints['tube_x']['scanner'],
            to_state)
        time.sleep(0.5)
        self._update_gui()

        #  not required, but will catch an odd configuration
        self._set_servo_state_xy(self._configured_constraints['tube_y']['scanner'],
            to_state)
        time.sleep(0.5)
        self._update_gui()

        self._set_servo_state_z(self._configured_constraints['tube_z']['scanner'],
            to_state)
        time.sleep(0.5)
        self._update_gui()
```

The Nova Power Script code requires separate commands for toggling either the x- or y-axis feedback state, or to toggle the z-axis feedback state. We address this with separate functions.

```python
def _set_servo_state_xy(self, scanner, to_state):
    """ Internal method to enable/disable XY closed loop feedback

    @param int scanner    : the scanner number
           bool to_state : the desired state of the feedback loop
    """

    command =    ('SetParam tScanner, cParam, {scanner}, XYCLState, {to_state}'
                    .format(scanner=scanner, to_state=int(to_state)))  # bool to int
    self._run_script_text(command)

def _set_servo_state_z(self, scanner, to_state):
    """ Internal method to enable/disable Z closed loop feedback

    @param int scanner    : the scanner number
           bool to_state : the desired state of the feedback loop
    """

    command =    ('SetParam tScanner, cParam, {scanner}, ZCLState, {to_state}'
                    .format(scanner=scanner, to_state=int(to_state)))  # bool to int
    self._run_script_text(command)
```

B.2.4   Retreiving the Stage Position

To retrieve the position of the stage (and the tube if it is configured), we simply iterate over
the configured axes. A data object of the type 'dictionary' is populated with the requested
information, and returned at the end of the function.

```python
def get_pos(self, param_list=None):
    """ Gets current position of the stage arms

    @param list param_list: optional, if a specific position of an axis
                            is desired, then the labels of the needed
                            axis should be passed in the param_list.
                            If nothing is passed, then the positions of
                            all axes are returned.

    @return dict: with keys being the axis labels and item the current
                  position.
    """
    param_dict = {}

    for axis in ['x', 'y', 'z']:
        scanner = self._configured_constraints[axis]['scanner']
        channel = self._configured_constraints[axis]['channel']

        command = ('{axis}Pos = GetParam(tScanner, scPosition, {scanner}, {channel
            })\n\n'
                   'SetSharedDataVal "shared_{axis}Pos", {axis}Pos, "F64", 8'
                   .format(axis=axis, channel=channel, scanner=scanner))

        self._run_script_text(command)
        time.sleep(0.1)
        param_dict[axis] = self._get_shared_float('shared_{axis}Pos'.format(axis=
            axis)) *1e-6
        # NT-MDT scanner communication in microns
        time.sleep(0.1)

        # reset shared data values
        self._reset_shared_data('shared_{axis}Pos'.format(axis=axis))
        time.sleep(0.1)

    #  check if the user has specified they have the 'tube' scanner
    if [s for s in self._configured_constraints if 'tube' in s]:

        for axis in ['tube_x', 'tube_y', 'tube_z']:
            scanner = self._configured_constraints[axis]['scanner']
            channel = self._configured_constraints[axis]['channel']

            command = ('{axis}Pos = GetParam(tScanner, scPosition, {scanner}, {channel
                })\n\n'
                       'SetSharedDataVal "shared_{axis}Pos", {axis}Pos, "F64", 8'
                       .format(axis=axis, channel=channel, scanner=scanner))

            self._run_script_text(command)
            time.sleep(0.1)
            param_dict[axis] = self._get_shared_float('shared_{axis}Pos'.format(axis=
                axis)) *1e-6
            # NT-MDT scanner communication in microns
            time.sleep(0.1)
            self._reset_shared_data('shared_{axis}Pos'.format(axis=axis))
            time.sleep(0.1)

    if param_list:
        param_list = [x.lower() for x in param_list]  # make all param_list elements
            lower case
        for axis in list(set(param_dict.keys()) - set(param_list)):  # axes not in
            param_list
            del param_dict[axis]
        return param_dict
    else:
        return param_dict
```

We can see that on lines 25 and 46 a conversion is undertaken to convert between SI units, which are used universally throughout Qudi, to micrometers, which are the units that the NT-MDT stage operates in. These device-specific adjustments are planned to happen here at the hardware/software level interface by design.

B.2.5   Setting the Stage Position

This process is similar to that of retrieving the stage position, though with additional safeguards added to ensure the user does not attempt to dive the stage beyond its constraints. Internal to Qudi this method of motor movement is referred to as an 'absolute move,' in that an absolute coordinate is specified for the stage to transit to. This is in contrast to a 'relative move' command which gives dimensions for stage transit relative to its current position. The absolute move function is shown below.

```python
def move_abs(self, param_dict=None):
    """Move the stage to absolute position

    @param dict param_dict: dictionary, which passes all the relevant
                            parameters, which should be changed. Usage:
                            {'axis_label': <the-abs-pos-value>}.
                            'axis_label' must correspond to a label given
                            to one of the axis.
                            The values for the axes are in meter,
                            the value for the rotation is in degrees.

    @return dict pos: dictionary with the current axis position
    """

    invalid_axis = set(param_dict)-set(self._configured_constraints)

    if invalid_axis:
        for axis in invalid_axis:
            self.log.warning('Desired axis {axis} is undefined'
                            .format(axis=axis))

    for axis in ['x', 'y', 'z']:
        if axis in param_dict.keys():
            scanner = self._configured_constraints[axis]['scanner']
            channel = self._configured_constraints[axis]['channel']
            to_position = param_dict[axis]
            self._do_move_abs(axis, scanner, channel, to_position)
            time.sleep(0.1)

    # check if the user has specified they have the 'tube' scanner
    if [s for s in self._configured_constraints if 'tube' in s]:

        for axis in ['tube_x', 'tube_y', 'tube_z']:
            if axis in param_dict.keys():
                scanner = self._configured_constraints[axis]['scanner']
                channel = self._configured_constraints[axis]['channel']
                to_position = param_dict[axis]
                self._do_move_abs(axis, scanner, channel, to_position)
                time.sleep(0.1)

    # # Use this code to populate the returned parmeter dictionary,
    # # it has been removed to speed-up scanning.
    # self.get_pos()
    # time.sleep(0.1)
    # param_dict = self.get_pos()

    self._update_gui()
    return param_dict
```

On lines 27 and 38 of the code snippet above a call is made to the function _do_move_abs, inside which the movement is cross-checked with the instrument's constraints, i.e. the maximum and minimum travel range of the stage.

```python
def _do_move_abs(self, axis, scanner, channel, to_pos):
    """ Internal method for absolute axis move in meters

    @param string axis   : name of the axis to be moved
           int channel   : channel of the axis to be moved
           float to_pos  : desired position in meters
    """

    if not(self._configured_constraints[axis]['pos_min'] <= to_pos <= self.
           _configured_constraints[axis]['pos_max']):
        self.log.warning('Cannot make the movement of the {axis} axis'
                         'since the border [{min},{max}] would be crossed! Ignore
                             command!'
                         .format(axis=axis, min=self._configured_constraints[axis]['
                             pos_min'], max=self._configured_constraints[axis]['pos_max
                             ']))
    else:
        self._write_axis_move(axis, scanner, channel, to_pos)
```

Upon determination that the requested movement action is safe the requested position is subsequently written to the axis:

```python
def _write_axis_move(self, axis, scanner, channel, to_pos):
    """ Internal method to move a specified axis

    @param string axis   : name of the axis to be moved
           int channel   : channel of the axis to be moved
           float to_pos  : desired position in meters
    """

    to_pos = to_pos /1e-6  # NT–MDT scanner communication in microns

    command = ('SetParam tScanner, scPosition, {scanner}, {channel}, {position}\n'
               'Do\n'
               'idle\n'
               'Loop Until GetParam(tScanner, cStatus, {scanner}) = False'
               .format(channel=channel, position=to_pos, scanner=scanner))

    self._run_script_text(command)
    time.sleep(0.1)
```

B.2.6   Abort Movement

Finally, we include a command which can be executed to abort the movement of the stage. This utilises the `_emergency_interupt` function which we created earlier, in combination with an additional check of the status of the stage to ensure that the movement action has stopped.

```python
def abort(self):
    """Stops movement of the stage

    Nova Px software must be revision 18659 or newer for this feature.

    @return int: error code (0:OK, -1:error)
    """
    scanners = []

    for axis in set(self._configured_constraints):
        if self._configured_constraints[axis]['scanner'] not in scanners:
            scanners.append(self._configured_constraints[axis]['scanner'])

    for scanner in scanners:
        self._emergency_interrupt(scanner)

    status = 0

    for scanner in scanners:
```

```
20              # CInt(Abs(Value))
21          command = ('Sc{scanner}Mv = GetParam(tScanner, cStatus, {scanner})\n\n'
22                     'Sc{scanner}Mv = CInt(Abs(Sc{scanner}Mv))\n\n'   # bool to int
23                     'SetSharedDataVal "shared_Sc{scanner}Mv", Sc{scanner}Mv, "F64", 8'
24                     .format(scanner=scanner))

26          self._run_script_text(command)
27          time.sleep(0.1)
28          status += self._get_shared_float('shared_Sc{scanner}Mv'.format(scanner=scanner)
                )
29          self._reset_shared_data('shared_Sc{scanner}Mv'.format(axis=axis))
30          time.sleep(0.1)

32      self._update_gui()

34      return status
```

C

Scanner Motor Interfuse Line Scanning

"Talk is cheap. Show me the code."

Linus Torvalds

This appendix contains the code referenced in § 4.4. The iteration of positions on the requested scan line occurs on line 27 below, and the collection of photon counts in line 34.

```python
def scan_line(self, line_path=None, pixel_clock=False):
    """ Scans a line and returns the counts on that line.

    @param float[][4] line_path: array of 4-part tuples defining the voltage points

    @param bool pixel_clock: whether we need to output a pixel clock for this line

    @return float[]: the photon counts per second
    """

    #if self.getState() == 'locked':
    #    self.log.error('A scan_line is already running, close this one first.')
    #    return -1
    #
    #self.lock()

    if not isinstance(line_path, (frozenset, list, set, tuple, np.ndarray, )):
        self.log.error('The given line to scan is not the right format or array type.')
        return np.array([-1.])

    self.set_up_line(np.shape(line_path)[1])

    count_data = np.zeros(self._line_length)

    for i in range(self._line_length):
        coords = line_path[:, i]
        self.scanner_set_position(x=coords[0], y=coords[1], z=coords[2], a=coords[3])

        # dwell to accumulate count data
        time.sleep(self._dwell_delay)
        # record count data
        this_count_data = self._counter_logic.countdata[0, -self._dwell_cnt_bins:]
        count_data[i] = np.mean(this_count_data)

    return np.array([count_data]).T
```

D

Maximum Likelihood Fitting by Bayesian Marginalisation

"Do not trust any statistics you did not fake yourself."

Winston Churchill

This appendix has been created to provide a brief overview of the Bayesian fitting algorithm implemented in § 5.2.4. A thorough and rigorous description of the method is beyond the purview of this thesis. However, as the implementation of such an algorithm is not yet commonplace in the community, we present a short primer for the reader.

To extract information on the anti-Stokes signal evident in our bulk diamond room-temperature reference data presented in § 5.2.4, we fit the sum of a line (to account for the background of the signal) and a Lorentzian. Diamond Raman lines have previously been fit with Voigt functions to account for the instrument resolution being broad relative to the Raman linewidth [182], however, here the instrument resolution is much finer than the measured linewidth. The Raman line is expected to be Lorentzian, however, the presence of inhomogeneous factors could lead to an altered line shape. A Lorentzian was found to be a good fit to our data. In this case, Figure D.1, the data set contains obvious outliers generated by either cosmic rays or dead pixels on the spectrograph CCD. When a conventional least squared fitting algorithm is implemented, Figure D.1a, it is apparent that outliers disproportionately influence the fit due to the nature of the squared loss function. Inspired by recent research conducted by members of our research group [192, 193], a Bayesian estimation algorithm is implemented to fit our model (the Lorentzian and line convolution) to our data. A brief description of this technique is presented below.

First, we use our prior knowledge of the expected data to create a model, for which we select the sum of a line and a Lorentzian given by

$$y_{\text{model}}(x) = A\frac{1}{2\pi}\frac{\sigma}{(x - \mu)^2 + \frac{\sigma^2}{2}} + mx + b \qquad (\text{D.1})$$

where A is the amplitude, σ is the linewidth, μ is the line position, m is the gradient, and b is the y-intercept. Next, some probability distribution is assigned to each data point. Since the CCD counts photons, we assume the dominant noise to be Poissonian sampling noise. For large N the Poissonian distribution is well approximated by a Gaussian with width $\sqrt{N}$. We take this Gaussian as the uncertainty distribution of our data, which allows us to calculate the likelihood as

$$P\left(\vec{y}, \vec{x} \mid I\right) \propto \prod_{i=1}^{N} \exp\left[-\frac{1}{2\sqrt{y_i}^2}(y_i - y_{\text{model}}(x_i \mid I))^2\right] \tag{D.2}$$

where I represents the choice of model parameters (A, σ, μ, m, and b) and background information.

Monte Carlo 'walkers', inherited from Markov chain Monte Carlo (MCMC) methods, are algorithmically created using the Python emcee package [205] to explore the parameter space. The walkers adjust the model parameters and compute the probability of observing the data given the adjusted model, which is the likelihood (here proportional to the posterior). In our implementation of the algorithm, we summon 150 walkers, that explore the parameter space for 4.5×10^6 steps.

The distribution of the walkers, each navigating the probability landscape, gives us the probability distribution of the model parameters, which is known as the posterior distribution. We refer to the region within which 90% of the walkers for each parameter lie as the 90% credible region. This region is plotted in Figure D.2 (blue region) for each fit parameter. We attain final fit values from the median of the posterior distribution, plotted in Figure D.2 (orange line), such that we can produce a single set of maximum likelihood fit parameters from which we can calculate the anti-Stokes / Stokes ratio for this dataset.

To identify outliers in the data, we modify the above process by assigning a probability for each data point that the data is either genuine or is noise.

$$\begin{aligned}
P\left(\vec{y}, \vec{x} \mid I\right) \propto \prod_{i=1}^{N} \Bigg(& g_i \exp\left[-\frac{1}{2\sqrt{y_i}^2}(y_i - y_{\text{model}}(x_i \mid I))^2\right] \\
& + (1 - g_i) \exp\left[-\frac{1}{2\sigma_B^2}(y_i - y_{\text{model}}(x_i \mid I))^2\right]\Bigg)
\end{aligned} \tag{D.3}$$

where g_i is the probability that the point lies on the model, and σ_B is the width of a broad Gaussian that accounts for outliers. This addition adds an extra dimension to the model for each data point included in the fit — so it can be seen that the computational intensity grows quickly with the amount of data considered. For this reason, we select only data points immediately surrounding the anti-Stokes peak, in addition to a small amount of data $\sim 0.5\,\text{nm}$ to each side (to better estimate the gradient of the line), over which we run our fitting algorithm. Figure D.1b shows the data points considered for the fit in blue, whereas those in grey are included for aesthetics only. Data points that the algorithm has determined more probable to be noise than to have been generated by the model are circled in red, and are excluded from contributing to the final fit parameters.

Through comparison of the least squares fit to the data, Figure D.1a, and the Bayesian fit, Figure D.1b, we can observe a dramatic increase in the accuracy of the fit. This fitting technique allows us to continue with the analysis of our nanodiamond thermometry data, Chapter 5, with confidence in the determination of these specific fit parameters.

(a)

(b)
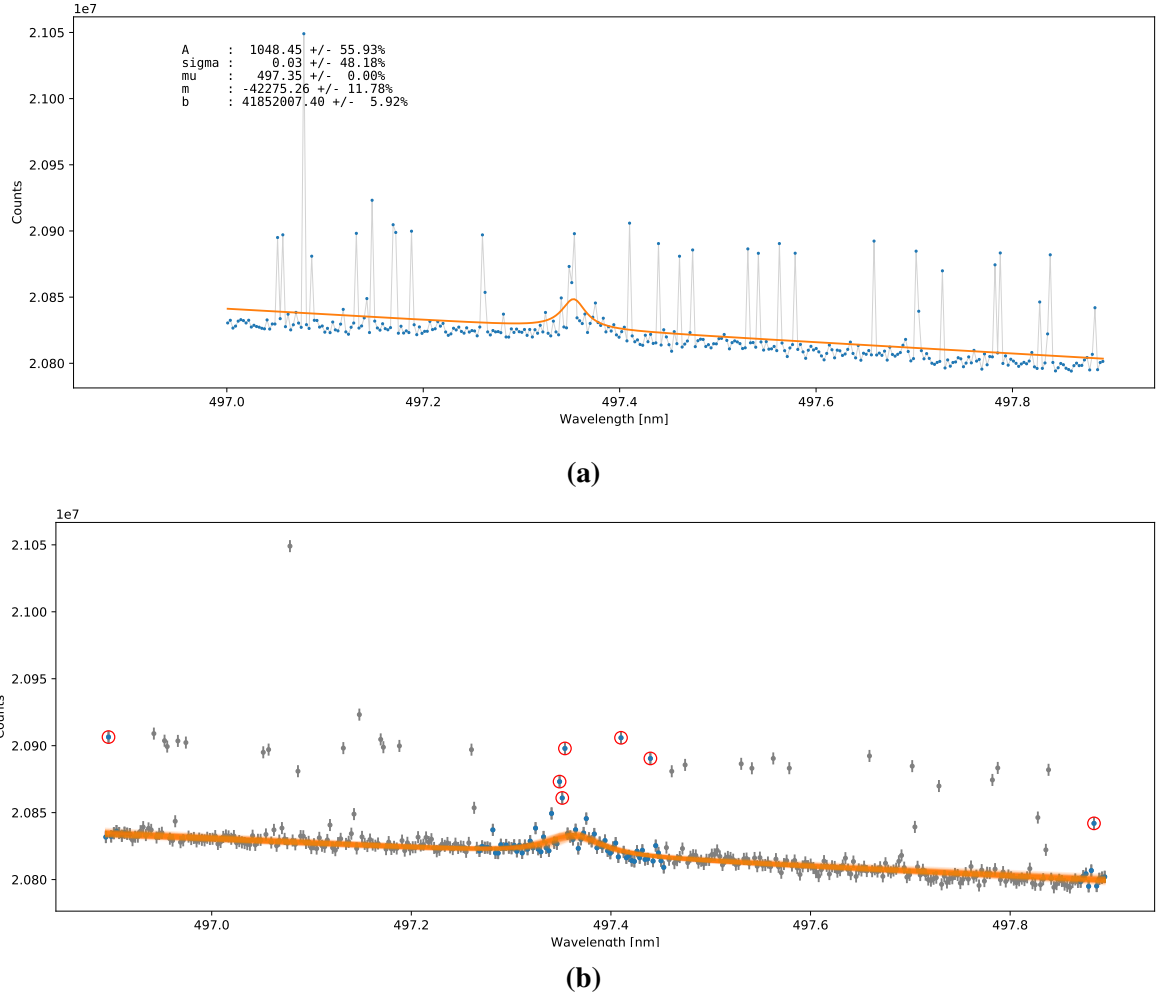
Figure D.1: Comparison of the maximum likelihood fits produced by the conventional least squares fitting algorithm and the Bayesian fitting algorithm. Integrated photon counts from $1,300$ minutes of data acquisition of the anti-Stokes signal of our bulk diamond, room-temperature reference, presented in § 5.2.4. **(a)** Least squares fit to the data. It is apparent that outliers (likely generated by cosmic rays or dead pixels on the spectrograph CCD) disproportionately influence the fit due to the nature of the squared loss function. **(b)** Credible fit region of the anti-Stokes signal by Bayesian marginalisation. The 90% credible fit region is shown in orange. Blue data points are included in the fitting algorithm whereas grey data points have been excluded due to computational intensity. Data points circled in red are been computed by the algorithm to more likely be noise than to be genuine data. Error bars are chosen to be a constant that is $\sim \sqrt{N}$, where N is the number of counts.

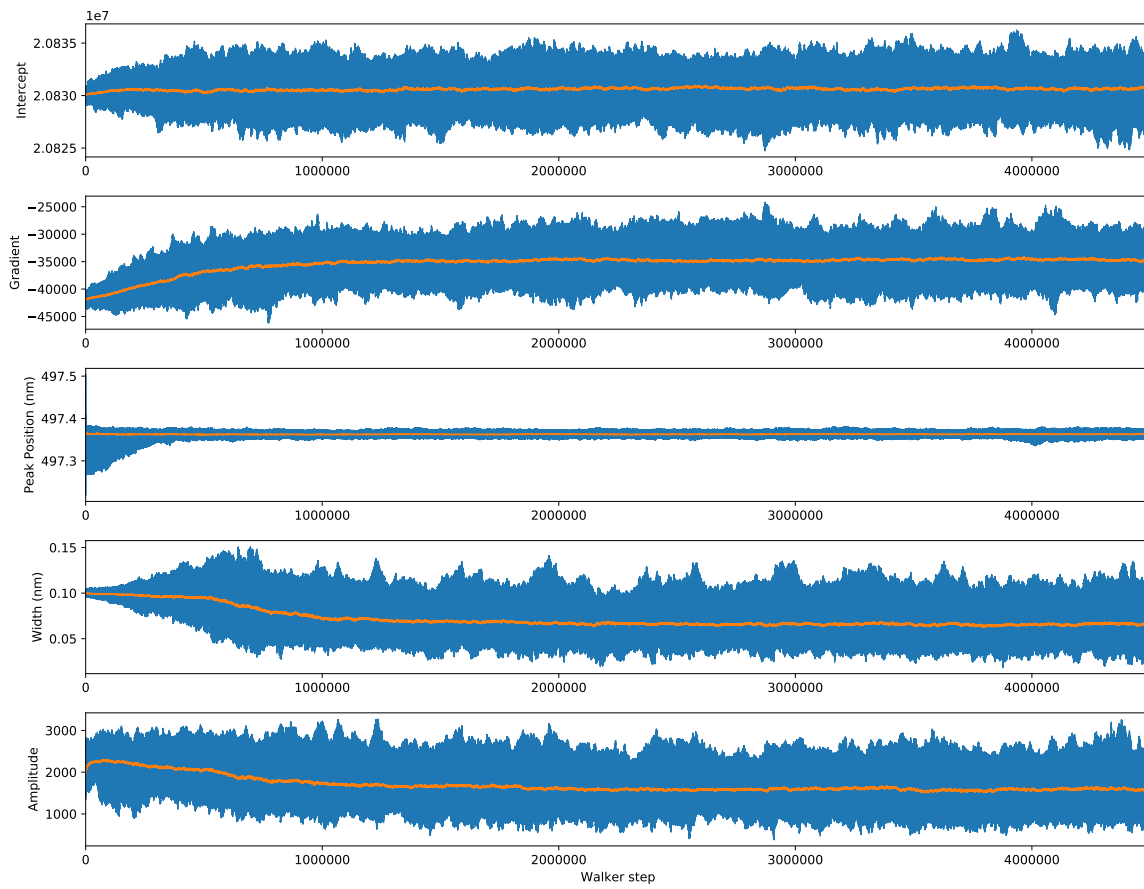**Figure D.2: Stabilisation of the maximum likelihood fit parameters.** The orange data indicated the median value of each fit parameter, and the 90% credible region is indicated in blue. The walker distribution converges to a steady state which is interpreted to represent the posterior distribution.

References

[1] A. M. Zaitsev, *Optical Properties of Diamond: A Data Handbook.* Springer, first ed., 2001.

[2] G. Balasubramanian, P. Neumann, D. Twitchen, M. Markham, R. Kolesov, N. Mizuochi, J. Isoya, J. Achard, J. Beck, J. Tissler, V. Jacques, P. R. Hemmer, F. Jelezko, and J. Wrachtrup, "Ultralong spin coherence time in isotopically engineered diamond," *Nature Materials*, vol. 8, pp. 383–387, May 2009.

[3] I. Aharonovich, S. Castelletto, D. A. Simpson, C.-H. Su, A. D. Greentree, and S. Prawer, "Diamond-based single-photon emitters," *Reports on Progress in Physics*, vol. 74, p. 076501, July 2011.

[4] V. N. Mochalin, O. Shenderova, D. Ho, and Y. Gogotsi, "The properties and applications of nanodiamonds," *Nature Nanotechnology*, vol. 7, pp. 11–23, Jan. 2012.

[5] Y.-R. Chang, H.-Y. Lee, K. Chen, C.-C. Chang, D.-S. Tsai, C.-C. Fu, T.-S. Lim, Y.-K. Tzeng, C.-Y. Fang, C.-C. Han, H.-C. Chang, and W. Fann, "Mass production and dynamic imaging of fluorescent nanodiamonds," *Nature Nanotechnology*, vol. 3, pp. 284–288, May 2008.

[6] L. P. McGuinness, Y. Yan, A. Stacey, D. A. Simpson, L. T. Hall, D. Maclaurin, S. Prawer, P. Mulvaney, J. Wrachtrup, F. Caruso, R. E. Scholten, and L. C. L. Hollenberg, "Quantum measurement and orientation tracking of fluorescent nanodiamonds inside living cells," *Nature Nanotechnology*, vol. 6, pp. 358–363, June 2011.

[7] V. R. Horowitz, B. J. Alemán, D. J. Christle, A. N. Cleland, and D. D. Awschalom, "Electron spin resonance of nitrogen-vacancy centers in optically trapped nanodiamonds," *Proceedings of the National Academy of Sciences*, vol. 109, pp. 13493–13497, Aug. 2012.

[8] E. Rej, T. Gaebel, T. Boele, D. E. J. Waddington, and D. J. Reilly, "Hyperpolarized nanodiamond with long spin-relaxation times," *Nature Communications*, vol. 6, p. 8459, Oct. 2015.

[9] R. A. Shimkunas, E. Robinson, R. Lam, S. Lu, X. Xu, X.-Q. Zhang, H. Huang, E. Osawa, and D. Ho, "Nanodiamond–insulin complexes as pH-dependent protein delivery vehicles," *Biomaterials*, vol. 30, pp. 5720–5728, Oct. 2009.

[10] K. V. Purtov, A. I. Petunin, A. E. Burov, A. P. Puzyr, and V. S. Bondar, "Nanodiamonds as Carriers for Address Delivery of Biologically Active Substances," *Nanoscale Research Letters*, vol. 5, p. 631, Mar. 2010.

[11] A. Alhaddad, M.-P. Adam, J. Botsoa, G. Dantelle, S. Perruchas, T. Gacoin, C. Mansuy, S. Lavielle, C. Malvy, F. Treussart, and J.-R. Bertrand, "Nanodiamond as a Vector for siRNA Delivery to Ewing Sarcoma Cells," *Small*, vol. 7, no. 21, pp. 3087–3095, 2011.

[12] J. R. Maze, P. L. Stanwix, J. S. Hodges, S. Hong, J. M. Taylor, P. Cappellaro, L. Jiang, M. V. G. Dutt, E. Togan, A. S. Zibrov, A. Yacoby, R. L. Walsworth, and M. D. Lukin, "Nanoscale magnetic sensing with an individual electronic spin in diamond," *Nature*, vol. 455, pp. 644–647, Oct. 2008.

[13] G. Balasubramanian, I. Y. Chan, R. Kolesov, M. Al-Hmoud, J. Tisler, C. Shin, C. Kim, A. Wojcik, P. R. Hemmer, A. Krueger, T. Hanke, A. Leitenstorfer, R. Bratschitsch, F. Jelezko, and J. Wrachtrup, "Nanoscale imaging magnetometry with diamond spins under ambient conditions," *Nature*, vol. 455, pp. 648–651, Oct. 2008.

[14] O. Conquest, "Nano-Scale Raman Thermometry of Diamond," Master's thesis, Macquarie University, 2017.

[15] M. L. Terranova, S. Orlanducci, M. Rossi, and E. Tamburri, "Nanodiamonds for field emission: state of the art," *Nanoscale*, vol. 7, pp. 5094–5114, Mar. 2015.

[16] P. Neumann, I. Jakobi, F. Dolde, C. Burk, R. Reuter, G. Waldherr, J. Honert, T. Wolf, A. Brunner, J. H. Shim, D. Suter, H. Sumiya, J. Isoya, and J. Wrachtrup, "High-Precision Nanoscale Temperature Sensing Using Single Defects in Diamond," *Nano Letters*, vol. 13, pp. 2738–2742, June 2013.

[17] X. Zhang, E. Wang, and X. Yang, "Design and simulation of Nano-diamond film pressure sensor," *Vacuum*, vol. 99, pp. 189–191, Jan. 2014.

[18] A. Afandi, A. Howkins, I. W. Boyd, and R. B. Jackman, "Nanodiamonds for device applications: An investigation of the properties of boron-doped detonation nanodiamonds," *Scientific Reports*, vol. 8, p. 3270, Feb. 2018.

[19] F. Jelezko, T. Gaebel, I. Popa, A. Gruber, and J. Wrachtrup, "Observation of Coherent Oscillations in a Single Electron Spin," *Physical Review Letters*, vol. 92, p. 076401, Feb. 2004.

[20] F. Jelezko and J. Wrachtrup, "Read-out of single spins by optical spectroscopy," *Journal of Physics: Condensed Matter*, vol. 16, p. R1089, Aug. 2004.

[21] H. Bernien, B. Hensen, W. Pfaff, G. Koolstra, M. S. Blok, L. Robledo, T. H. Taminiau, M. Markham, D. J. Twitchen, L. Childress, and R. Hanson, "Heralded entanglement between solid-state qubits separated by three metres," *Nature*, vol. 497, pp. 86–90, May 2013.

[22] B. Hensen, H. Bernien, A. E. Dréau, A. Reiserer, N. Kalb, M. S. Blok, J. Ruitenberg, R. F. L. Vermeulen, R. N. Schouten, C. Abellán, W. Amaya, V. Pruneri, M. W. Mitchell, M. Markham, D. J. Twitchen, D. Elkouss, S. Wehner, T. H. Taminiau, and R. Hanson, "Loophole-free Bell inequality violation using electron spins separated by 1.3 kilometres," *Nature*, vol. 526, pp. 682–686, Oct. 2015.

[23] M. W. Doherty, C. A. Meriles, A. Alkauskas, H. Fedder, M. J. Sellars, and N. B. Manson, "Towards a Room-Temperature Spin Quantum Bus in Diamond via Electron Photoionization, Transport, and Capture," *Physical Review X*, vol. 6, p. 041035, Nov. 2016.

[24] L. M. Oberg, E. Huang, P. M. Reddy, A. Alkauskas, A. D. Greentree, J. H. Cole, N. B. Manson, C. A. Meriles, and M. W. Doherty, "Spin coherent quantum transport of electrons between defects in diamond," *arXiv:1905.07084 [cond-mat, physics:quant-ph]*, May 2019. arXiv: 1905.07084.

[25] A. M. Tyryshkin, S. A. Lyon, A. V. Astashkin, and A. M. Raitsimring, "Electron spin relaxation times of phosphorus donors in silicon," *Physical Review B*, vol. 68, p. 193207, Nov. 2003.

[26] M. L. Juan, C. Bradac, B. Besga, M. Johnsson, G. Brennen, G. Molina-Terriza, and T. Volz, "Cooperatively enhanced dipole forces from artificial atoms in trapped nanodiamonds," *Nature Physics*, vol. advance online publication, Nov. 2016.

[27] C. Kittel, *Introduction to Solid State Physics*. Wiley, eighth ed., 2004.

[28] F. Mohs, *Treatise on Mineralogy*. Edimburgh: Caledonian Mercury Press, 1825.

[29] R. H. Telling, C. J. Pickard, M. C. Payne, and J. E. Field, "Theoretical Strength and Cleavage of Diamond," *Physical Review Letters*, vol. 84, pp. 5160–5163, May 2000.

[30] D. Roundy and M. L. Cohen, "Ideal strength of diamond, Si, and Ge," *Physical Review B*, vol. 64, p. 212103, Nov. 2001.

[31] W. R. Tyson, "Theoretical strength of perfect crystals," *Philosophical Magazine*, vol. 14, pp. 925–936, 1966.

[32] Z. L. Xiaoguang Luo, "Compressive Strength of Diamond From First-Principles Calculation," *Journal of Physical Chemistry C*, vol. 114, pp. 17851–17853, 2010.

[33] J. E. Field and C. S. J. Pickles, "Strength, fracture and friction properties of diamond," *Diamond and Related Materials*, vol. 5, pp. 625–634, May 1996.

[34] Y. Zhang, H. Sun, and C. Chen, "Strain dependent bonding in solid C3N4: High elastic moduli but low strength," *Physical Review B*, vol. 73, p. 064109, Feb. 2006.

[35] J. E. Field, *The properties of diamond*. Academic Press, 1979.

[36] C. J. H. Wort and R. S. Balmer, "Diamond as an electronic material," *Materials Today*, vol. 11, pp. 22–28, Jan. 2008.

[37] G. E. Harlow, *The Nature of Diamonds*. Cambridge University Press, 1998.

[38] D. F. Edwards and E. Ochoa, "Infrared refractive index of diamond," *Journal of the Optical Society of America*, vol. 71, pp. 607–608, May 1981.

[39] M. Seal, "Thermal and optical applications of thin film diamond," *Philosophical transactions-Royal Society of London. Physical sciences and engineering*, vol. 342, no. 1664, pp. 313–322, 1993.

[40] I. Kiflawi, A. T. Collins, K. Iakoubovskii, and D. Fisher, "Electron irradiation and the formation of vacancy-interstitial pairs in diamond," *Journal of Physics: Condensed Matter*, vol. 19, p. 046216, Jan. 2007.

[41] D. C. Hunt, D. J. Twitchen, M. E. Newton, J. M. Baker, T. R. Anthony, W. F. Banholzer, and S. S. Vagarali, "Identification of the neutral carbon <100>-split interstitial in diamond," *Physical Review B*, vol. 61, pp. 3863–3876, Feb. 2000.

[42] H. E. Smith, G. Davies, M. E. Newton, and H. Kanda, "Structure of the self-interstitial in diamond," *Physical Review B*, vol. 69, p. 045203, Jan. 2004.

[43] L. S. Hounsome, R. Jones, P. M. Martineau, D. Fisher, M. J. Shaw, P. R. Briddon, and S. Öberg, "Origin of brown coloration in diamond," *Physical Review B*, vol. 73, p. 125203, Mar. 2006.

[44] K. Iakoubovskii, S. Dannefaer, and A. Stesmans, "Evidence for vacancy-interstitial pairs in Ib-type diamond," *Physical Review B*, vol. 71, p. 233201, June 2005.

[45] P. L. Hanley, I. Kiflawi, and A. R. Lang, "On Topographically Identifiable Sources of Cathodoluminescence in Natural Diamonds," *Philosophical Transactions of the Royal Society of London. Series A, Mathematical and Physical Sciences*, vol. 284, pp. 329–368, Feb. 1977.

[46] J. Walker, "Optical absorption and luminescence in diamond," *Reports on Progress in Physics*, vol. 42, pp. 1605–1659, Oct. 1979.

[47] A. T. Collins, "The detection of colour-enhanced and synthetic gem diamonds by optical spectroscopy," *Diamond and Related Materials*, vol. 12, pp. 1976–1983, Oct. 2003.

[48] W. V. Smith, P. P. Sorokin, I. L. Gelles, and G. J. Lasher, "Electron-Spin Resonance of Nitrogen Donors in Diamond," *Physical Review*, vol. 115, pp. 1546–1552, Sept. 1959.

[49] G. Davies and M. F. Hamer, "Optical Studies of the 1.945 eV Vibronic Band in Diamond," *Proceedings of the Royal Society of London. A. Mathematical and Physical Sciences*, vol. 348, pp. 285–298, Feb. 1976.

[50] L. Du Preez, *Electron paramagnetic resonance and optical investigationsof defect centres in diamond*. PhD thesis, University of Witwaters, 1965.

[51] A. Gruber, A. Dräbenstedt, C. Tietz, L. Fleury, J. Wrachtrup, and C. v. Borczyskowski, "Scanning Confocal Optical Microscopy and Magnetic Resonance on Single Defect Centers," *Science*, vol. 276, pp. 2012–2014, June 1997.

[52] L. Robledo, H. Bernien, T. v. d. Sar, and R. Hanson, "Spin dynamics in the optical cycle of single nitrogen-vacancy centres in diamond," *New Journal of Physics*, vol. 13, p. 025013, Feb. 2011.

[53] Y. Mita, "Change of absorption spectra in type-Ib diamond with heavy neutron irradiation," *Physical Review B*, vol. 53, pp. 11360–11364, May 1996.

[54] A. Gali, M. Fyta, and E. Kaxiras, "Ab initio supercell calculations on nitrogen-vacancy center in diamond: Electronic structure and hyperfine tensors," *Physical Review B*, vol. 77, p. 155206, Apr. 2008.

[55] J. H. N. Loubser and J. A. Van Wyk, "Optical spin-polarisation in a triplet state in irradiated and annealed type 1b diamonds," 1977.

[56] J. H. N. Loubser and J. A. v. Wyk, "Electron spin resonance in the study of diamond," *Reports on Progress in Physics*, vol. 41, p. 1201, Aug. 1978.

[57] J. M. Taylor, P. Cappellaro, L. Childress, L. Jiang, D. Budker, P. R. Hemmer, A. Yacoby, R. Walsworth, and M. D. Lukin, "High-sensitivity diamond magnetometer with nanoscale resolution," *Nature Physics*, vol. 4, pp. 810–816, Oct. 2008.

[58] M. S. Grinolds, S. Hong, P. Maletinsky, L. Luan, M. D. Lukin, R. L. Walsworth, and A. Yacoby, "Nanoscale magnetic imaging of a single electron spin under ambient conditions," *Nature Physics*, vol. 9, pp. 215–219, Apr. 2013.

[59] M. S. Grinolds, M. Warner, K. De Greve, Y. Dovzhenko, L. Thiel, R. L. Walsworth, S. Hong, P. Maletinsky, and A. Yacoby, "Subnanometre resolution in three-dimensional magnetic resonance imaging of individual dark spins," *Nature Nanotechnology*, vol. 9, pp. 279–284, Apr. 2014.

[60] C. Bradac, *The Properties of Nitrogen-Vacancy Centres in Nanodiamond.* PhD thesis, Macquarie University, Sydney, Feb. 2012.

[61] E. Erlich and W. D. Hausel, *Diamond Deposits: Origin, Exploration, and History of Discovery.* SME, 2002.

[62] H. T. Hall, "Some High-Pressure, High-Temperature Apparatus Design Considerations: Equipment for Use at 100 000 Atmospheres and 3000degC," *Review of Scientific Instruments*, vol. 29, pp. 267–275, Apr. 1958.

[63] F. Rossini, "Heat and free energy of formation of carbon dioxide, and of the transition between graphite and diamond," *Journal of Research of the National Bureau of Standards*, vol. 21, pp. 491–513, 1938.

[64] R. Berman and S. F. Simon, "On the Graphite - Diamond Equilibrium," *Zeitschrift für Elektrochemie, Berichte der Bunsengesellschaft für physikalische Chemie*, vol. 59, pp. 333–338, July 1955.

[65] N. Pal'yanov and Sokol, "Fluid-bearing alkaline carbonate melts as the medium for the formation of diamonds in the Earth's mantle: an experimental study," *Lithos*, pp. 145–159, 2002.

[66] E. Ito, "Theory and Practice – Multianvil Cells and High-Pressure Experimental Methods," in *Treatise on Geophysics* (G. Schubert, ed.), pp. 197–230, Amsterdam: Elsevier, 2007.

[67] R. C. Linares and P. J. Doering, "System and method for producing synthetic diamond," Feb. 2011. U.S. Classification 117/89, 117/104, 117/929, 423/446; International Classification C30B29/06, C30B25/02, C30B25/10; Cooperative Classification C30B25/02, C30B25/105; European Classification C30B25/10B, C30B25/02.

[68] B. V. Derjaguin, D. V. Fedoseev, V. M. Lukyanovich, B. V. Spitzin, V. A. Ryabov, and A. V. Lavrentyev, "Filamentary diamond crystals," *Journal of Crystal Growth*, vol. 2, pp. 380–384, Dec. 1968.

[69] S. Matsumoto, Y. Sato, M. Kamo, and N. Setaka, "Vapor Deposition of Diamond Particles from Methane," *Japanese Journal of Applied Physics*, vol. 21, p. L183, Apr. 1982.

[70] M. Kamo, Y. Sato, S. Matsumoto, and N. Setaka, "Diamond synthesis from gas phase in microwave plasma," *Journal of Crystal Growth*, vol. 62, pp. 642–644, Aug. 1983.

[71] S. Matsumoto and Y. Matsui, "Electron microscopic observation of diamond particles grown from the vapour phase," *Journal of Materials Science*, vol. 18, pp. 1785–1793, June 1983.

[72] J. R. Rabeau, A. Stacey, A. Rabeau, S. Prawer, F. Jelezko, I. Mirza, and J. Wrachtrup, "Single Nitrogen Vacancy Centers in Chemical Vapor Deposited Diamond Nanocrystals," *Nano Letters*, vol. 7, pp. 3433–3437, Nov. 2007.

[73] S. Prawer and R. Kalish, "Ion-beam-induced transformation of diamond," *Physical Review B*, vol. 51, pp. 15711–15722, June 1995.

[74] R. Kalish, C. Uzan-Saguy, B. Philosoph, V. Richter, J. P. Lagrange, E. Gheeraert, A. Deneuville, and A. T. Collins, "Nitrogen doping of diamond by ion implantation," *Diamond and Related Materials*, vol. 6, pp. 516–520, Mar. 1997.

[75] R. Kalish, "Doping of diamond," *Carbon*, vol. 37, pp. 781–785, Apr. 1999.

[76] J. Meijer, B. Burchard, M. Domhan, C. Wittmann, T. Gaebel, I. Popa, F. Jelezko, and J. Wrachtrup, "Generation of single color centers by focused nitrogen implantation," *Applied Physics Letters*, vol. 87, p. 261909, Dec. 2005.

[77] F. C. Waldermann, P. Olivero, J. Nunn, K. Surmacz, Z. Y. Wang, D. Jaksch, R. A. Taylor, I. A. Walmsley, M. Draganski, P. Reichart, A. D. Greentree, D. N. Jamieson, and S. Prawer, "Creating diamond color centers for quantum optical applications," *Diamond and Related Materials*, vol. 16, pp. 1887–1895, Nov. 2007.

[78] J. Martin, R. Wannemacher, J. Teichert, L. Bischoff, and B. Köhler, "Generation and detection of fluorescent color centers in diamond with submicron resolution," *Applied Physics Letters*, vol. 75, pp. 3096–3098, Nov. 1999.

[79] T. Schenkel, A. Persaud, S. J. Park, J. Meijer, J. R. Kingsley, J. W. McDonald, J. P. Holder, J. Bokor, and D. H. Schneider, "Single ion implantation for solid state quantum computer development," *Journal of Vacuum Science & Technology B*, vol. 20, pp. 2819–2823, Nov. 2002.

[80] K. Iakoubovskii, I. Kiflawi, K. Johnston, A. Collins, G. Davies, and A. Stesmans, "Annealing of vacancies and interstitials in diamond," *Physica B: Condensed Matter*, vol. 340–342, pp. 67–75, Dec. 2003.

[81] J. Meijer, T. Vogel, B. Burchard, I. W. Rangelow, L. Bischoff, J. Wrachtrup, M. Domhan, F. Jelezko, W. Schnitzler, S. A. Schulz, K. Singer, and F. Schmidt-Kaler, "Concept of deterministic single ion doping with sub-nm spatial resolution," *Applied Physics A*, vol. 83, pp. 321–327, May 2006.

[82] C. Bradac, T. Gaebel, and J. R. Rabeau, "Nitrogen-Vacancy Color Centers in Diamond: Properties, Synthesis, and Applications," in *Optical Engineering of Diamond* (R. P. Mildren and J. R. Rabeau, eds.), Wiley, first ed., 2013.

[83] A. Dräbenstedt, L. Fleury, C. Tietz, F. Jelezko, S. Kilin, A. Nizovtzev, and J. Wrachtrup, "Low-temperature microscopy and spectroscopy on single defect centers in diamond," *Physical Review B*, vol. 60, pp. 11503–11508, Oct. 1999.

[84] R. Brouri, A. Beveratos, J.-P. Poizat, and P. Grangier, "Photon antibunching in the fluorescence of individual color centers in diamond," *Optics Letters*, vol. 25, pp. 1294–1296, Sept. 2000.

[85] C. Kurtsiefer, S. Mayer, P. Zarda, and H. Weinfurter, "Stable Solid-State Source of Single Photons," *Physical Review Letters*, vol. 85, pp. 290–293, July 2000.

[86] C. Bradac, T. Gaebel, N. Naidoo, M. J. Sellars, J. Twamley, L. J. Brown, A. S. Barnard, T. Plakhotnik, A. V. Zvyagin, and J. R. Rabeau, "Observation and control of blinking nitrogen-vacancy centres in discrete nanodiamonds," *Nature Nanotechnology*, vol. 5, pp. 345–349, May 2010.

[87] N. Mizuochi, T. Makino, H. Kato, D. Takeuchi, M. Ogura, H. Okushi, M. Nothaft, P. Neumann, A. Gali, F. Jelezko, J. Wrachtrup, and S. Yamasaki, "Electrically driven single-photon source at room temperature in diamond," *Nature Photonics*, vol. 6, pp. 299–303, May 2012.

[88] A. Beveratos, R. Brouri, T. Gacoin, A. Villing, J.-P. Poizat, and P. Grangier, "Single Photon Quantum Cryptography," *Physical Review Letters*, vol. 89, p. 187901, Oct. 2002.

[89] R. Alléaume, F. Treussart, G. Messin, Y. Dumeige, J.-F. Roch, A. Beveratos, R. Brouri-Tualle, J.-P. Poizat, and P. Grangier, "Experimental open-air quantum key distribution with a single-photon source," *New Journal of Physics*, vol. 6, p. 92, July 2004.

[90] E. Knill, R. Laflamme, and G. J. Milburn, "A scheme for efficient quantum computation with linear optics," *Nature*, vol. 409, pp. 46–52, Jan. 2001.

[91] F. Jelezko, T. Gaebel, I. Popa, M. Domhan, A. Gruber, and J. Wrachtrup, "Observation of Coherent Oscillation of a Single Nuclear Spin and Realization of a Two-Qubit Conditional Quantum Gate," *Physical Review Letters*, vol. 93, p. 130501, Sept. 2004.

[92] D. P. DiVincenzo and IBM, "The Physical Implementation of Quantum Computation," *arXiv:quant-ph/0002077*, Feb. 2000.

[93] G. Waldherr, P. Neumann, S. F. Huelga, F. Jelezko, and J. Wrachtrup, "Violation of a Temporal Bell Inequality for Single Spins in a Diamond Defect Center," *Physical Review Letters*, vol. 107, p. 090401, Aug. 2011.

[94] P. Neumann, R. Kolesov, B. Naydenov, J. Beck, F. Rempp, M. Steiner, V. Jacques, G. Balasubramanian, M. L. Markham, D. J. Twitchen, S. Pezzagna, J. Meijer, J. Twamley, F. Jelezko, and J. Wrachtrup, "Quantum register based on coupled electron spins in a room-temperature solid," *Nature Physics*, vol. 6, pp. 249–253, Apr. 2010.

[95] L. Robledo, L. Childress, H. Bernien, B. Hensen, P. F. A. Alkemade, and R. Hanson, "High-fidelity projective read-out of a solid-state spin quantum register," *Nature*, vol. 477, pp. 574–578, Sept. 2011.

[96] S. Steinert, F. Dolde, P. Neumann, A. Aird, B. Naydenov, G. Balasubramanian, F. Jelezko, and J. Wrachtrup, "High sensitivity magnetic imaging using an array of spins in diamond," *Review of Scientific Instruments*, vol. 81, p. 043705, Apr. 2010.

[97] A. M. Schrand, H. Huang, C. Carlson, J. J. Schlager, E. Ōsawa, S. M. Hussain, and L. Dai, "Are Diamond Nanoparticles Cytotoxic?," *The Journal of Physical Chemistry B*, vol. 111, pp. 2–7, Jan. 2007.

[98] M. Minsky, "Memoir on inventing the confocal scanning microscope," *Scanning*, vol. 10, no. 4, pp. 128–138, 1988.

[99] J.-M. L. Floch, C. Bradac, N. Nand, S. Castelletto, M. E. Tobar, and T. Volz, "Addressing a single spin in diamond with a macroscopic dielectric microwave cavity," *Applied Physics Letters*, vol. 105, p. 133101, Sept. 2014.

[100] M. W. Doherty, N. B. Manson, P. Delaney, F. Jelezko, J. Wrachtrup, and L. C. L. Hollenberg, "The nitrogen-vacancy colour centre in diamond," *Physics Reports*, vol. 528, pp. 1–45, July 2013.

[101] L. Rondin, J.-P. Tetienne, T. Hingant, J.-F. Roch, P. Maletinsky, and V. Jacques, "Magnetometry with nitrogen-vacancy defects in diamond," *Reports on Progress in Physics*, vol. 77, no. 5, p. 056503, 2014.

[102] M. Fox, *Quantum Optics: An Introduction*. OUP Oxford, Apr. 2006.

[103] E. L. Hahn, "Spin Echoes," *Physical Review*, vol. 80, pp. 580–594, Nov. 1950.

[104] W. H. Zurek, "Decoherence, einselection, and the quantum origins of the classical," *Reviews of Modern Physics*, vol. 75, pp. 715–775, May 2003.

[105] S. Takahashi, R. Hanson, J. van Tol, M. S. Sherwin, and D. D. Awschalom, "Quenching Spin Decoherence in Diamond through Spin Bath Polarization," *Physical Review Letters*, vol. 101, p. 047601, July 2008.

[106] J. R. Maze, J. M. Taylor, and M. D. Lukin, "Electron spin decoherence of single nitrogen-vacancy defects in diamond," *Physical Review B*, vol. 78, p. 094303, Sept. 2008.

[107] J. R. Petta, A. C. Johnson, J. M. Taylor, E. A. Laird, A. Yacoby, M. D. Lukin, C. M. Marcus, M. P. Hanson, and A. C. Gossard, "Coherent Manipulation of Coupled Electron Spins in Semiconductor Quantum Dots," *Science*, vol. 309, pp. 2180–2184, Sept. 2005.

[108] S. Hill, R. S. Edwards, N. Aliaga-Alcalde, and G. Christou, "Quantum Coherence in an Exchange-Coupled Dimer of Single-Molecule Magnets," *Science*, vol. 302, pp. 1015–1018, Nov. 2003.

[109] G. de Loubens, A. D. Kent, V. Krymov, G. J. Gerfen, C. C. Beedle, and D. N. Hendrickson, "High frequency EPR on dilute solutions of the single molecule magnet Ni4," *Journal of Applied Physics*, vol. 103, p. 07B910, Feb. 2008.

[110] R. H. Brown and R. Q. Twiss, "LXXIV. A new type of interferometer for use in radio astronomy," *The London, Edinburgh, and Dublin Philosophical Magazine and Journal of Science*, vol. 45, pp. 663–682, July 1954.

[111] R. H. Brown and R. Q. Twiss, "Correlation between Photons in two Coherent Beams of Light," *Nature*, vol. 177, p. 27, Jan. 1956.

[112] J.-M. Le Floch, Y. Fan, G. Humbert, Q. Shan, D. Férachou, R. Bara-Maillet, M. Aubourg, J. G. Hartnett, V. Madrangeas, D. Cros, J.-M. Blondy, J. Krupka, and M. E. Tobar, "Invited Article: Dielectric material characterization techniques and designs of high-Q resonators for applications from micro to millimeter-waves frequencies applicable at room and cryogenic temperatures," *Review of Scientific Instruments*, vol. 85, p. 031301, Mar. 2014.

[113] J.-M. le Floch, M. E. Tobar, D. Cros, and J. Krupka, "Low-loss materials for high Q-factor Bragg reflector resonators," *Applied Physics Letters*, vol. 92, p. 032901, Jan. 2008.

[114] J.-M. L. Floch, R. Bara, J. G. Hartnett, M. E. Tobar, D. Mouneyrac, D. Passerieux, D. Cros, J. Krupka, P. Goy, and S. Caroopen, "Electromagnetic properties of polycrystalline diamond from 35 K to room temperature and microwave to terahertz frequencies," *Journal of Applied Physics*, vol. 109, p. 094103, May 2011.

[115] J. G. Hartnett, D. Mouneyrac, J.-M. Le Floch, J. Krupka, M. E. Tobar, and D. Cros, "Modified permittivity observed in bulk gallium arsenide and gallium phosphide samples at 50K using the whispering gallery mode method," *Applied Physics Letters*, vol. 93, p. 062105, Aug. 2008.

[116] J. G. Hartnett, D. Mouneyrac, J.-M. Le Floch, J. Krupka, M. E. Tobar, and D. Cros, "Observation of persistent photoconductivity in bulk gallium arsenide and gallium phosphide samples at cryogenic temperatures using the whispering gallery mode method," *Journal of Applied Physics*, vol. 104, p. 113714, Dec. 2008.

[117] J.-M. L. Floch, F. Houndonougbo, V. Madrangeas, D. Cros, M. Guilloux-Viry, and W. Peng, "Thin Film Materials Characterization Using TE Modes Cavity," *Journal of Electromagnetic Waves and Applications*, vol. 23, pp. 549–559, Jan. 2009.

[118] P. Queffelec, V. Laur, A. Chevalier, J.-M. Le Floch, D. Passerieux, D. Cros, V. Madrangeas, A. Le Febvrier, S. Députier, M. Guilloux-Viry, G. Houzet, T. Lacrevaz, C. Bermond, and B. Fléchet, "Intercomparison of permittivity measurement techniques for ferroelectric thin layers," *Journal of Applied Physics*, vol. 115, p. 024103, Jan. 2014.

[119] K. Benmessai, W. G. Farr, D. L. Creedon, Y. Reshitnyk, J.-M. Le Floch, T. Duty, and M. E. Tobar, "Hybrid electron spin resonance and whispering gallery mode resonance spectroscopy of Fe^{3+} in sapphire," *Physical Review B*, vol. 87, p. 094412, Mar. 2013.

[120] J. G. Hartnett, J. L. Floch, M. E. Tobar, J. Krupka, and P. Bourgeois, "Anisotropic paramagnetic susceptibility of crystalline ruby at cryogenic temperatures," in *2007 IEEE International Frequency Control Symposium Joint with the 21st European Frequency and Time Forum*, pp. 666–671, May 2007.

[121] A. Beveratos, R. Brouri, T. Gacoin, J.-P. Poizat, and P. Grangier, "Nonclassical radiation from diamond nanocrystals," *Physical Review A*, vol. 64, p. 061802, Nov. 2001.

[122] C. Bradac, M. T. Johnsson, M. v. Breugel, B. Q. Baragiola, R. Martin, M. L. Juan, G. K. Brennen, and T. Volz, "Room-temperature spontaneous superradiance from single diamond nanocrystals," *Nature Communications*, vol. 8, p. 1205, Oct. 2017.

[123] R. H. Dicke, "Coherence in Spontaneous Radiation Processes," *Physical Review*, vol. 93, pp. 99–110, Jan. 1954.

[124] A. Ashkin, "Acceleration and Trapping of Particles by Radiation Pressure," *Physical Review Letters*, vol. 24, pp. 156–159, Jan. 1970.

[125] C. Bradac, "Nanoscale Optical Trapping: A Review," *Advanced Optical Materials*, vol. 6, p. 1800005, June 2018.

[126] R. Grimm, M. Weidemüller, and Y. B. Ovchinnikov, "Optical Dipole Traps for Neutral Atoms," in *Advances In Atomic, Molecular, and Optical Physics* (Benjamin Bederson and Herbert Walther, ed.), vol. Volume 42, pp. 95–170, Academic Press, 2000.

[127] C. Cohen-Tannoudji, "Manipulating atoms with photons," *Physica Scripta*, vol. 1998, p. 33, Jan. 1998.

[128] P. D. Lett, W. D. Phillips, S. L. Rolston, C. E. Tanner, R. N. Watts, and C. I. Westbrook, "Optical molasses," *Journal of the Optical Society of America B*, vol. 6, pp. 2084–2107, Nov. 1989.

[129] J. Simon, W. S. Bakr, R. Ma, M. E. Tai, P. M. Preiss, and M. Greiner, "Quantum simulation of antiferromagnetic spin chains in an optical lattice," *Nature*, vol. 472, pp. 307–312, Apr. 2011.

[130] S. Putz, D. O. Krimer, R. Amsüss, A. Valookaran, T. Nöbauer, J. Schmiedmayer, S. Rotter, and J. Majer, "Protecting a spin ensemble against decoherence in the strong-coupling regime of cavity QED," *Nature Physics*, vol. 10, pp. 720–724, Oct. 2014.

[131] B. C. Rose, A. M. Tyryshkin, H. Riemann, N. V. Abrosimov, P. Becker, H.-J. Pohl, M. L. W. Thewalt, K. M. Itoh, and S. A. Lyon, "Coherent Rabi Dynamics of a Superradiant Spin Ensemble in a Microwave Cavity," *Physical Review X*, vol. 7, p. 031002, July 2017.

[132] J. A. Mlynek, A. A. Abdumalikov, C. Eichler, and A. Wallraff, "Observation of Dicke superradiance for two artificial atoms in a cavity with high decay rate," *Nature Communications*, vol. 5, p. 5186, Nov. 2014.

[133] J. Eschner, C. Raab, F. Schmidt-Kaler, and R. Blatt, "Light interference from single atoms and their mirror images," *Nature*, vol. 413, pp. 495–498, Oct. 2001.

[134] R. G. DeVoe and R. G. Brewer, "Observation of Superradiant and Subradiant Spontaneous Emission of Two Trapped Ions," *Physical Review Letters*, vol. 76, pp. 2049–2052, Mar. 1996.

[135] M. Scheibner, T. Schmidt, L. Worschech, A. Forchel, G. Bacher, T. Passow, and D. Hommel, "Superradiance of quantum dots," *Nature Physics*, vol. 3, pp. 106–110, Feb. 2007.

[136] M. Gross, C. Fabre, P. Pillet, and S. Haroche, "Observation of Near-Infrared Dicke Superradiance on Cascading Transitions in Atomic Sodium," *Physical Review Letters*, vol. 36, pp. 1035–1038, Apr. 1976.

[137] N. Skribanowitz, I. P. Herman, J. C. MacGillivray, and M. S. Feld, "Observation of Dicke Superradiance in Optically Pumped HF Gas," *Physical Review Letters*, vol. 30, pp. 309–312, Feb. 1973.

[138] S. Inouye, A. P. Chikkatur, D. M. Stamper-Kurn, J. Stenger, D. E. Pritchard, and W. Ketterle, "Superradiant Rayleigh Scattering from a Bose-Einstein Condensate," *Science*, vol. 285, pp. 571–574, July 1999.

[139] M. A. Norcia, M. N. Winchester, J. R. K. Cline, and J. K. Thompson, "Superradiance on the millihertz linewidth strontium clock transition," *Science Advances*, vol. 2, p. e1601231, Oct. 2016.

[140] M. Gross, P. Goy, C. Fabre, S. Haroche, and J. M. Raimond, "Maser Oscillation and Microwave Superradiance in Small Systems of Rydberg Atoms," *Physical Review Letters*, vol. 43, pp. 343–346, July 1979.

[141] Y. Kaluzny, P. Goy, M. Gross, J. M. Raimond, and S. Haroche, "Observation of Self-Induced Rabi Oscillations in Two-Level Atoms Excited Inside a Resonant Cavity: The Ringing Regime of Superradiance," *Physical Review Letters*, vol. 51, pp. 1175–1178, Sept. 1983.

[142] A. Sipahigil, R. E. Evans, D. D. Sukachev, M. J. Burek, J. Borregaard, M. K. Bhaskar, C. T. Nguyen, J. L. Pacheco, H. A. Atikian, C. Meuwly, R. M. Camacho, F. Jelezko, E. Bielejec, H. Park, M. Lončar, and M. D. Lukin, "An integrated diamond nanophotonics platform for quantum-optical networks," *Science*, vol. 354, pp. 847–850, Nov. 2016.

[143] A. Angerer, K. Streltsov, T. Astner, S. Putz, H. Sumiya, S. Onoda, J. Isoya, W. J. Munro, K. Nemoto, J. Schmiedmayer, and J. Majer, "Superradiant emission from colour centres in diamond," *Nature Physics*, p. 1, Sept. 2018.

[144] M. Gross and S. Haroche, "Superradiance: An essay on the theory of collective spontaneous emission," *Physics Reports*, vol. 93, pp. 301–396, Dec. 1982.

[145] C.-C. Fu, H.-Y. Lee, K. Chen, T.-S. Lim, H.-Y. Wu, P.-K. Lin, P.-K. Wei, P.-H. Tsao, H.-C. Chang, and W. Fann, "Characterization and application of single fluorescent nanodiamonds as cellular biomarkers," *Proceedings of the National Academy of Sciences*, vol. 104, pp. 727–732, Jan. 2007.

[146] J. O. Orwa, K. W. Nugent, D. N. Jamieson, and S. Prawer, "Raman investigation of damage caused by deep ion implantation in diamond," *Physical Review B*, vol. 62, pp. 5461–5472, Sept. 2000.

[147] D. McCloskey, D. Fox, N. O'Hara, V. Usov, D. Scanlan, N. McEvoy, G. S. Duesberg, G. L. W. Cross, H. Z. Zhang, and J. F. Donegan, "Helium ion microscope generated nitrogen-vacancy centres in type Ib diamond," *Applied Physics Letters*, vol. 104, p. 031109, Jan. 2014.

[148] R. Martin, "Exploring Cooperative Effects with Nitrogen-Vacancy Centres in Diamond," Master's thesis, Macquarie University, 2017.

[149] C. Santori, P. E. Barclay, K.-M. C. Fu, R. G. Beausoleil, S. Spillane, and M. Fisch, "Nanophotonics for quantum optics using nitrogen-vacancy centers in diamond," *Nanotechnology*, vol. 21, no. 27, p. 274008, 2010.

[150] V. M. Huxter, T. a. A. Oliver, D. Budker, and G. R. Fleming, "Vibrational and electronic dynamics of nitrogen-vacancy centres in diamond revealed by two-dimensional ultrafast spectroscopy," *Nature Physics*, vol. 9, pp. 744–749, Nov. 2013.

[151] R. Ulbricht, S. Dong, A. Gali, S. Meng, and Z.-H. Loh, "Vibrational relaxation dynamics of the nitrogen-vacancy center in diamond," *Physical Review B*, vol. 97, p. 220302, June 2018.

[152] S. Felton, A. M. Edmonds, M. E. Newton, P. M. Martineau, D. Fisher, D. J. Twitchen, and J. M. Baker, "Hyperfine interaction in the ground state of the negatively charged nitrogen vacancy center in diamond," *Physical Review B*, vol. 79, p. 075203, Feb. 2009.

[153] V. M. Acosta, E. Bauch, M. P. Ledbetter, C. Santori, K.-M. C. Fu, P. E. Barclay, R. G. Beausoleil, H. Linget, J. F. Roch, F. Treussart, S. Chemerisov, W. Gawlik, and D. Budker, "Diamonds with a high density of nitrogen-vacancy centers for magnetometry applications," *Physical Review B*, vol. 80, p. 115202, Sept. 2009.

[154] R. Friedberg, S. R. Hartmann, and J. T. Manassah, "Limited superradiant damping of small samples," *Physics Letters A*, vol. 40, pp. 365–366, Aug. 1972.

[155] K. D. B. Higgins, S. C. Benjamin, T. M. Stace, G. J. Milburn, B. W. Lovett, and E. M. Gauger, "Superabsorption of light via quantum engineering," *Nature Communications*, vol. 5, p. 4705, Aug. 2014.

[156] C. A. McLellan, B. A. Myers, S. Kraemer, K. Ohno, D. D. Awschalom, and A. C. Bleszynski Jayich, "Patterned Formation of Highly Coherent Nitrogen-Vacancy Centers Using a Focused Electron Irradiation Technique," *Nano Letters*, vol. 16, pp. 2450–2454, Apr. 2016.

[157] M. J. Burek, N. P. de Leon, B. J. Shields, B. J. M. Hausmann, Y. Chu, Q. Quan, A. S. Zibrov, H. Park, M. D. Lukin, and M. Lončar, "Free-Standing Mechanical and Photonic Nanostructures in Single-Crystal Diamond," *Nano Letters*, vol. 12, pp. 6084–6089, Dec. 2012.

[158] P. Rath, S. Khasminskaya, C. Nebel, C. Wild, and W. H. P. Pernice, "Diamond-integrated optomechanical circuits," *Nature Communications*, vol. 4, p. 1690, Apr. 2013.

[159] M. C. W. Hunter and R. i. H. M. Hunter, *Establishing the New Science: The Experience of the Early Royal Society*. Boydell & Brewer Ltd, 1989. Google-Books-ID: T8YHw7bRx2wC.

[160] J. M. Binder, A. Stark, N. Tomek, J. Scheuer, F. Frank, K. D. Jahnke, C. Müller, S. Schmitt, M. H. Metsch, T. Unden, T. Gehring, A. Huck, U. L. Andersen, L. J. Rogers, and F. Jelezko, "Qudi: A modular python suite for experiment control and data processing," *SoftwareX*, vol. 6, pp. 85–90, Jan. 2017.

[161] D. Singh Chawla, "The unsung heroes of scientific software," *Nature News*, vol. 529, p. 115, Jan. 2016.

[162] J. M. Perkel, "Programming: Pick up Python," *Nature News*, vol. 518, p. 125, Feb. 2015.

[163] R. Munroe, "xkcd: Standards."

[164] T. Feger, C. Bacigalupo, T. R. Bedding, J. Bento, D. W. Coutts, M. J. Ireland, Q. A. Parker, A. Rizzuto, and I. Spaleniak, "RHEA: the ultra-compact replicable high-resolution exoplanet and Asteroseismology spectrograph," in *Ground-based and Airborne Instrumentation for Astronomy V*, vol. 9147, p. 91477I, International Society for Optics and Photonics, July 2014.

[165] T. Feger, M. J. Ireland, C. Schwab, J. Bento, C. Bacigalupo, and D. W. Coutts, "Attaining m s-1 level intrinsic Doppler precision with RHEA, a low-cost single-mode spectrograph," *Experimental Astronomy*, vol. 42, pp. 285–300, Dec. 2016.

[166] J. Bento, T. Feger, M. J. Ireland, A. Rains, N. Jovanovic, D. W. Coutts, C. Schwab, A. Arriola, and S. Gross, "Performance and future developments of the RHEA single-mode spectrograph," in *Ground-based and Airborne Instrumentation for Astronomy VI*, vol. 9908, p. 99086K, International Society for Optics and Photonics, Aug. 2016.

[167] A. D. Rains, M. J. Ireland, N. Jovanovic, T. Feger, J. Bento, C. Schwab, D. W. Coutts, O. Guyon, A. Arriola, and S. Gross, "Precision single mode fibre integral field spectroscopy with the RHEA spectrograph," in *Ground-based and Airborne Instrumentation for Astronomy VI*, vol. 9908, p. 990876, International Society for Optics and Photonics, Aug. 2016.

[168] S.-Y. Ding, J. Yi, J.-F. Li, B. Ren, D.-Y. Wu, R. Panneerselvam, and Z.-Q. Tian, "Nanostructure-based plasmon-enhanced Raman spectroscopy for surface analysis of materials," *Nature Reviews Materials*, vol. 1, p. 16021, June 2016.

[169] S. Laing, L. E. Jamieson, K. Faulds, and D. Graham, "Surface-enhanced Raman spectroscopy for *in vivo* biosensing," *Nature Reviews Chemistry*, vol. 1, p. 0060, Aug. 2017.

[170] J. R. Lombardi, "Raman spectroscopy: Enhanced by organic surfaces," *Nature Materials*, vol. 16, pp. 878–880, Sept. 2017.

[171] C. H. Camp Jr and M. T. Cicerone, "Chemically sensitive bioimaging with coherent Raman scattering," *Nature Photonics*, vol. 9, pp. 295–305, May 2015.

[172] C. V. Raman and K. S. Krishnan, "A New Type of Secondary Radiation," *Nature*, vol. 121, pp. 501–502, Mar. 1928.

[173] H. Haken and H. Christoph Wolf, "Raman Spectra," in *Molecular Physics and Elements of Quantum Chemistry: Introduction to Experiments and Theory* (H. Haken and H. Christoph Wolf, eds.), Advanced Texts in Physics, pp. 199–210, Berlin, Heidelberg: Springer Berlin Heidelberg, 1995.

[174] M. Balkanski, R. F. Wallis, and E. Haro, "Anharmonic effects in light scattering due to optical phonons in silicon," *Physical Review B*, vol. 28, pp. 1928–1934, Aug. 1983.

[175] C. Ramaswamy, "Raman Effect in Diamond," *Nature*, vol. 125, p. 704, May 1930.

[176] R. Robertson and J. J. Fox, "Infra-red Spectrum of Diamond by Infra-red Spectrometer and Raman Methods," *Nature*, vol. 125, p. 704, May 1930.

[177] P. G. Klemens, "Anharmonic Decay of Optical Phonons," *Physical Review*, vol. 148, pp. 845–848, Aug. 1966.

[178] W. J. Borer, S. S. Mitra, and K. V. Namjoshi, "Line shape and temperature dependence of the first order Raman spectrum of diamond," *Solid State Communications*, vol. 9, pp. 1377–1381, Aug. 1971.

[179] H. Herchen and M. A. Cappelli, "First-order Raman spectrum of diamond at high temperatures," *Physical Review B*, vol. 43, pp. 11740–11744, May 1991.

[180] E. S. Zouboulis and M. Grimsditch, "Raman scattering in diamond up to 1900 K," *Physical Review B*, vol. 43, pp. 12490–12493, May 1991.

[181] J. B. Cui, K. Amtmann, J. Ristein, and L. Ley, "Noncontact temperature measurements of diamond by Raman scattering spectroscopy," *Journal of Applied Physics*, vol. 83, pp. 7929–7933, May 1998.

[182] M. S. Liu, L. A. Bursill, S. Prawer, and R. Beserman, "Temperature dependence of the first-order Raman phonon line of diamond," *Physical Review B*, vol. 61, pp. 3391–3395, Feb. 2000.

[183] "Diamond (C), Debye temperature, heat capacity, density, hardness, melting point and related data," in *Group IV Elements, IV-IV and III-V Compounds. Part b - Electronic, Transport, Optical and Other Properties* (O. Madelung, U. Rössler, and M. Schulz, eds.), Landolt-Börnstein - Group III Condensed Matter, pp. 1–6, Berlin, Heidelberg: Springer Berlin Heidelberg, 2002.

[184] N. V. Surovtsev and I. N. Kupriyanov, "Temperature dependence of the Raman line width in diamond: Revisited," *Journal of Raman Spectroscopy*, vol. 46, no. 1, pp. 171–176, 2015.

[185] N. V. Surovtsev and I. Kupriyanov, "Effect of Nitrogen Impurities on the Raman Line Width in Diamond, Revisited," *Crystals*, vol. 7, p. 239, July 2017.

[186] K. Ganesan, P. K. Ajikumar, S. Ilango, G. Mangamma, and S. Dhara, "Si and N - Vacancy color centers in discrete diamond nanoparticles: Raman and fluorescence spectroscopic studies," *Diamond and Related Materials*, vol. 92, pp. 150–158, Feb. 2019.

[187] S. Osswald, V. N. Mochalin, M. Havel, G. Yushin, and Y. Gogotsi, "Phonon confinement effects in the Raman spectrum of nanodiamond," *Physical Review B*, vol. 80, p. 075419, Aug. 2009.

[188] M. Yoshikawa, Y. Mori, M. Maegawa, G. Katagiri, H. Ishida, and A. Ishitani, "Raman scattering from diamond particles," *Applied Physics Letters*, vol. 62, pp. 3114–3116, June 1993.

[189] K. W. Sun, J. Y. Wang, and T. Y. Ko, "Raman spectroscopy of single nanodiamond: Phonon-confinement effects," *Applied Physics Letters*, vol. 92, p. 153115, Apr. 2008.

[190] K. W. Sun, J. Y. Wang, and T. Y. Ko, "Photoluminescence and Raman spectroscopy of single diamond nanoparticle," *Journal of Nanoparticle Research*, vol. 10, pp. 115–120, Dec. 2008.

[191] M. J. D. Powell, "An efficient method for finding the minimum of a function of several variables without calculating derivatives," *The Computer Journal*, vol. 7, pp. 155–162, Jan. 1964.

[192] J. Geordy, L. Rogers, C. M. Rogers, T. Volz, and A. Gilchrist, "Bayesian estimation of switching rates for blinking emitters," *New Journal of Physics*, 2019.

[193] L. J. Rogers, O. Wang, Y. Liu, L. Antoniuk, C. Osterkamp, V. A. Davydov, V. N. Agafonov, A. B. Filipovski, F. Jelezko, and A. Kubanek, "Single SiV- Centers in Low-Strain Nanodiamonds with Bulklike Spectral Properties and Nanomanipulation Capabilities," *Physical Review Applied*, vol. 11, p. 024073, Feb. 2019.

[194] M. Chaigneau, G. Picardi, H. A. Girard, J.-C. Arnault, and R. Ossikovski, "Laser heating versus phonon confinement effect in the Raman spectra of diamond nanoparticles," *Journal of Nanoparticle Research*, vol. 14, p. 955, June 2012.

[195] X.-D. Chen, C.-H. Dong, F.-W. Sun, C.-L. Zou, J.-M. Cui, Z.-F. Han, and G.-C. Guo, "Temperature dependent energy level shifts of nitrogen-vacancy centers in diamond," *Applied Physics Letters*, vol. 99, p. 161903, Oct. 2011.

[196] E. Neu, C. Hepp, M. Hauschild, S. Gsell, M. Fischer, H. Sternschulte, D. Steinmüller-Nethl, M. Schreck, and C. Becher, "Low-temperature investigations of single silicon vacancy colour centres in diamond," *New Journal of Physics*, vol. 15, p. 043005, Apr. 2013.

[197] M. W. Doherty, V. M. Acosta, A. Jarmola, M. S. J. Barson, N. B. Manson, D. Budker, and L. C. L. Hollenberg, "Temperature shifts of the resonances of the NV- center in diamond," *Physical Review B*, vol. 90, p. 041201, July 2014.

[198] J. Zhou, A. Panday, Y. Xu, X. Chen, L. Chen, C. Ji, and L. J. Guo, "Visualizing Mie Resonances in Low-Index Dielectric Nanoparticles," *Physical Review Letters*, vol. 120, p. 253902, June 2018.

[199] S. Prawer, K. W. Nugent, D. N. Jamieson, J. O. Orwa, L. A. Bursill, and J. L. Peng, "The Raman spectrum of nanocrystalline diamond," *Chemical Physics Letters*, vol. 332, pp. 93–97, Dec. 2000.

[200] J. W. Ager, D. K. Veirs, and G. M. Rosenblatt, "Spatially resolved Raman studies of diamond films grown by chemical vapor deposition," *Physical Review B*, vol. 43, pp. 6491–6499, Mar. 1991.

[201] T. Plakhotnik and D. Gruber, "Luminescence of nitrogen -vacancy centers in nanodiamonds at temperatures between 300 and 700 K: perspectives on nanothermometry," *Physical Chemistry Chemical Physics*, vol. 12, no. 33, pp. 9751–9756, 2010.

[202] T. T. Tran, B. Regan, E. A. Ekimov, Z. Mu, Y. Zhou, W.-b. Gao, P. Narang, A. S. Solntsev, M. Toth, I. Aharonovich, and C. Bradac, "Anti-Stokes excitation of solid-state quantum emitters for nanoscale thermometry," *Science Advances*, vol. 5, p. eaav9180, May 2019.

[203] T. Gaebel, C. Bradac, J. Chen, J. M. Say, L. Brown, P. Hemmer, and J. R. Rabeau, "Size-reduction of nanodiamonds via air oxidation," *Diamond and Related Materials*, vol. 21, pp. 28–32, Jan. 2012.

[204] MacFarlane A. G. J., Dowling Jonathan P., and Milburn Gerard J., "Quantum technology: the second quantum revolution," *Philosophical Transactions of the Royal Society of London. Series A: Mathematical, Physical and Engineering Sciences*, vol. 361, pp. 1655–1674, Aug. 2003.

[205] D. Foreman-Mackey, D. W. Hogg, D. Lang, and J. Goodman, "emcee: The MCMC Hammer," *Publications of the Astronomical Society of the Pacific*, vol. 125, p. 306, Mar. 2013.